Ensuring Accurate Cosmology from the Era of High-precision Cosmic Shear Surveys

Anurag Chandrahas Deshpande

A dissertation submitted in partial fulfillment

of the requirements for the degree of

Doctor of Philosophy

Department of Space and Climate Physics

Mullard Space Science Laboratory

University College London

December 2022

Declaration

I, Anurag Chandrahas Deshpande, confirm that the work presented in this thesis is my own. Where information has been derived from other sources, I confirm that this has been indicated in the work.

The research chapters which form the main body of this thesis and elements of the introductory chapter are based on work carried out by me in the following publications, where I am the first author:

- Section 1.3 & Chapter 2 - **Deshpande, A. C.**, Kitching, T. D., Cardone, V. F., et al. (69 others) 2020, A&A, 636, A95
- Chapter 3 - **Deshpande, A. C.** & Kitching, T. D. 2020, Phys. Rev. D, 101, 103531
- Chapter 4 - **Deshpande, A. C.** & Kitching, T. D. 2021, Phys. Rev. D, 103, 123510
- Chapter 5 - **Deshpande, A. C.**, Taylor, P. L. & Kitching, T. D. 2020, Phys. Rev. D, 102, 083535

Completed 'Research Paper Declaration Forms' are presented following this section. Additionally, I have contributed to multiple other academic papers during the funding period. These are:

- Euclid Collaboration: **Deshpande, A. C.**, Kitching, T. D., Hall, A., et al. 2023, arXiv e-prints, arXiv:2302.04507.
- Kitching, T. D. & **Deshpande, A. C.** 2022, OJA, Vol. 5
- Data Study Group team (Equal Contributions - Aragones, M., Bedogni, L., **Deshpande, A.**, Gieschen, A., Huang, Z., McIntyre, F., Muntaha Nawfee, S., Roumpani, F., Saad, A., Vonnak, R.) 2022, The Alan Turing Institute, April 2021 Data Study Group: CityMaaS, Zenodo.
- Kitching, T. D., **Deshpande, A. C.** & Taylor, P. L. 2021, OJA, Vol. 4

- Taylor, P. L., Kitching, T. D., Cardone, V. F., Ferté, A., Huff, E. M., Bernardeau, F., Rhodes, J., **Deshpande, A. C.**, et al. (87 others) 2021, OJA, Vol. 4

- Data Study Group team (Equal Contributions - Arnold, E., Chen, J., Croydon-Veleslavov, I., **Deshpande, A.**, Guha, T., He, Y., Moseley, B., Seng Ng, G., Prince, L., Statham, T., Strong, P.) 2021, The Alan Turing Institute, September 2020 Data Study Group: Greenvest Solutions, Zenodo.

- Kitching, T. D. **Deshpande, A. C.** & Taylor, P. L. 2020, OJA, Vol. 3

and they will not be discussed within this work.

UCL Research Paper Declaration Form: referencing the doctoral candidate's own published work(s)

Please use this form to declare if parts of your thesis are already available in another format, e.g. if data, text, or figures:

- have been uploaded to a preprint server;
- are in submission to a peer-reviewed publication;
- have been published in a peer-reviewed publication, e.g. journal, textbook.

This form should be completed as many times as necessary. For instance, if you have seven thesis chapters, two of which containing material that has already been published, you would complete this form twice.

1. For a research manuscript that has already been published (if not yet published, please skip to section 2):	
a) What is the title of the manuscript?	Euclid: The reduced shear approximation and magnification bias for Stage IV cosmic shear experiments
b) Please include a link to or doi for the work:	https://doi.org/10.1051/0004-6361/201937323
c) Where was the work published?	Astronomy & Astrophysics
d) Who published the work? (e.g. OUP):	ESO
e) When was the work published?	April 2020
a) List the manuscript's authors in the order they appear on the publication:	A.C. Deshpande, T.D. Kitching, V.F. Cardone, P.L. Taylor, S. Casas, S. Camera, C. Carbone, M. Kilbinger, V. Pettorino, Z. Sakr, D. Sapone, I. Tutusaus, N. Auricchio, C. Bodendorf, D. Bonino, M. Brescia, V. Capobianco, J. Carretero, M. Castellano, S. Cavuoti, R. Cledassou, G. Congedo, L. Conversi, L. Corcione, M. Cropper, F. Dubath, S. Dusini, G. Fabbian, E. Franceschi, M. Fumana, B. Garilli, F. Grupp, H. Hoekstra, F. Hormuth, H. Israel, K. Jahnke, S. Kermiche, B. Kubik, M. Kunz, F. Lacasa, S. Ligori, P.B. Lilje, I. Lloro, E. Maiorano, O. Marggraf, R. Massey, S. Mei, M. Meneghetti, G. Meylan, L. Moscardini, C. Padilla, S. Paltani, F. Pasian, S. Pires, G. Polenta, M. Poncet, F. Raison, J. Rhodes, M. Roncarelli, R. Saglia, P. Schneider,

	A. Secroun, S. Serrano, G. Sirri, J.L. Starck, F. Sureau, A.N. Taylor, I. Tereno, R. Toledo-Moreo, L. Valenziano, Y. Wang, J. Zoubian
f) Was the work peer reviewed?	Yes
g) Have you retained the copyright?	No
h) Was an earlier form of the manuscript uploaded to a preprint server? (e.g. medRxiv; if 'Yes', please give a link or doi):	Yes https://arxiv.org/abs/1912.07326

[If no, please seek permission from the relevant publisher and check the box next to the below statement]:

☒	*I acknowledge permission of the publisher named under **1d** to include in this thesis portions of the publication named as included in **1c**.*

2. For a research manuscript prepared for publication but that has not yet been published (if already published, please skip to section 3):	
b) What is the current title of the manuscript?	
c) Has the manuscript been uploaded to a preprint server? (e.g. medRxiv; if 'Yes', please give a link or doi):	
d) Where is the work intended to be published? (e.g. journal names)	
e) List the manuscript's authors in the intended authorship order:	
f) Stage of publication (e.g. in submission):	

3. For multi-authored work, please give a statement of contribution covering all authors (if single-author, please skip to section 4):

A. C. Deshpande was the primary author of this publication, and carried out all the analysis within the work, expect where stated otherwise. T. D. Kitching was the supervisor of A. C. Deshpande, and as such conceptualised the work, directed its scope, and informed experimental direction. V.F. Cardone provided data used in the analysis; specifically, Fisher matrices under varying specifications. P. L. Taylor carried out the forward modelling analysis discussed in Section 4.5. S. Casas, S. Camera, C. Carbone, M. Kilbinger, V. Pettorino, Z. Sakr, D. Sapone, and I. Tutusaus contributed to the code used to generate the covariance and Fisher matrices used in this analysis. All remaining authors received credit due to being key members of the Euclid Consortium; the experimental collaboration which this paper was published as part of.

4. In which chapter(s) of your thesis can this material be found?

Chapter 1 Section 1.3 and Chapter 2

5. e-Signatures confirming that the information above is accurate (this form should be co-signed by the supervisor/ senior author

unless this is not appropriate, e.g. if the paper was a single-author work):			
Candidate:	Anurag Chandrahas Deshpande	**Date:**	09/09/2022
Supervisor/ Senior Author (where appropriate):	Thomas Kitching	**Date:**	09/09/2022

UCL Research Paper Declaration Form: referencing the doctoral candidate's own published work(s)

Please use this form to declare if parts of your thesis are already available in another format, e.g. if data, text, or figures:

- have been uploaded to a preprint server;
- are in submission to a peer-reviewed publication;
- have been published in a peer-reviewed publication, e.g. journal, textbook.

This form should be completed as many times as necessary. For instance, if you have seven thesis chapters, two of which containing material that has already been published, you would complete this form twice.

1. For a research manuscript that has already been published (if not yet published, please skip to section 2):	
a) What is the title of the manuscript?	Post-Limber weak lensing bispectrum, reduced shear correction, and magnification bias correction
b) Please include a link to or doi for the work:	https://doi.org/10.1103/PhysRevD.101.103531
c) Where was the work published?	Physical Review D
d) Who published the work? (e.g. OUP):	APS
e) When was the work published?	May 2020
a) List the manuscript's authors in the order they appear on the publication:	Anurag C. Deshpande, Thomas D. Kitching
f) Was the work peer reviewed?	Yes
g) Have you retained the copyright?	No
h) Was an earlier form of the manuscript uploaded to a preprint server? (e.g. medRxiv; if 'Yes', please give a link or doi):	Yes https://arxiv.org/abs/2004.01666
[If no, please seek permission from the relevant publisher and check the box next to the below statement]:	
☒	*I acknowledge permission of the publisher named under **1d** to include in this thesis portions of the publication named as included in **1c**.*

2. For a research manuscript prepared for publication but that has not yet been published (if already published, please skip to section 3):	
b) What is the current title of the manuscript?	
c) Has the manuscript been uploaded to a preprint server? (e.g. medRxiv; if 'Yes', please give a link or doi):	
d) Where is the work intended to be published? (e.g. journal names)	
e) List the manuscript's authors in the intended authorship order:	
f) Stage of publication (e.g. in submission):	
3. For multi-authored work, please give a statement of contribution covering all authors (if single-author, please skip to section 4):	
A. C. Deshpande was the primary author of this publication, and carried out all the analysis within the work. T. D. Kitching was the supervisor of A. C. Deshpande, and as such conceptualised the work, directed its scope, and informed experimental direction.	
4. In which chapter(s) of your thesis can this material be found?	
Chapter 3	
5. e-Signatures confirming that the information above is accurate (this form should be co-signed by the supervisor/ senior author unless this is not appropriate, e.g. if the paper was a single-author work):	

Candidate:	Anurag Chandrahas Deshpande	**Date:**	09/09/2022
Supervisor/ Senior Author (where appropriate):	Thomas Kitching	**Date:**	09/09/2022

UCL Research Paper Declaration Form: referencing the doctoral candidate's own published work(s)

Please use this form to declare if parts of your thesis are already available in another format, e.g. if data, text, or figures:

- have been uploaded to a preprint server;
- are in submission to a peer-reviewed publication;
- have been published in a peer-reviewed publication, e.g. journal, textbook.

This form should be completed as many times as necessary. For instance, if you have seven thesis chapters, two of which containing material that has already been published, you would complete this form twice.

1. For a research manuscript that has already been published (if not yet published, please skip to section 2):	
a) What is the title of the manuscript?	Cosmological parameter biases from Doppler-shifted weak lensing in stage IV experiments
b) Please include a link to or doi for the work:	https://doi.org/10.1103/PhysRevD.103.123510
c) Where was the work published?	Physical Review D
d) Who published the work? (e.g. OUP):	APS
e) When was the work published?	June 2021
a) List the manuscript's authors in the order they appear on the publication:	Anurag C. Deshpande, Thomas D. Kitching
f) Was the work peer reviewed?	Yes
g) Have you retained the copyright?	No
h) Was an earlier form of the manuscript uploaded to a preprint server? (e.g. medRxiv; if 'Yes', please give a link or doi):	Yes https://arxiv.org/abs/2103.11936
[If no, please seek permission from the relevant publisher and check the box next to the below statement]:	
☒	*I acknowledge permission of the publisher named under **1d** to include in this thesis portions of the publication named as included in **1c**.*

2. For a research manuscript prepared for publication but that has not yet been published (if already published, please skip to section 3):	
b) What is the current title of the manuscript?	
c) Has the manuscript been uploaded to a preprint server? (e.g. medRxiv; if 'Yes', please give a link or doi):	
d) Where is the work intended to be published? (e.g. journal names)	
e) List the manuscript's authors in the intended authorship order:	
f) Stage of publication (e.g. in submission):	

3. For multi-authored work, please give a statement of contribution covering all authors (if single-author, please skip to section 4):

A. C. Deshpande was the primary author of this publication, and carried out all the analysis within the work. T. D. Kitching was the supervisor of A. C. Deshpande, and as such conceptualised the work, directed its scope, and informed experimental direction.

4. In which chapter(s) of your thesis can this material be found?

Chapter 4

5. e-Signatures confirming that the information above is accurate (this form should be co-signed by the supervisor/ senior author unless this is not appropriate, e.g. if the paper was a single-author work):

Candidate:	Anurag Chandrahas Deshpande	**Date:**	09/09/2022
Supervisor/ Senior Author (where appropriate):	Thomas Kitching	**Date:**	09/09/2022

UCL Research Paper Declaration Form: referencing the doctoral candidate's own published work(s)

Please use this form to declare if parts of your thesis are already available in another format, e.g. if data, text, or figures:

- have been uploaded to a preprint server;
- are in submission to a peer-reviewed publication;
- have been published in a peer-reviewed publication, e.g. journal, textbook.

This form should be completed as many times as necessary. For instance, if you have seven thesis chapters, two of which containing material that has already been published, you would complete this form twice.

1. For a research manuscript that has already been published (if not yet published, please skip to section 2):	
a) What is the title of the manuscript?	Accessing the high-ℓ frontier under the reduced shear approximation with k-cut cosmic shear
b) Please include a link to or doi for the work:	https://doi.org/10.1103/PhysRevD.102.083535
c) Where was the work published?	Physical Review D
d) Who published the work? (e.g. OUP):	APS
e) When was the work published?	October 2020
a) List the manuscript's authors in the order they appear on the publication:	Anurag C. Deshpande, Peter L. Taylor, Thomas D. Kitching
f) Was the work peer reviewed?	Yes
g) Have you retained the copyright?	No
h) Was an earlier form of the manuscript uploaded to a preprint server? (e.g. medRxiv; if 'Yes', please give a link or doi):	Yes https://arxiv.org/abs/2009.01792
[If no, please seek permission from the relevant publisher and check the box next to the below statement]:	
☒	*I acknowledge permission of the publisher named under **1d** to include in this thesis portions of the publication named as included in **1c**.*

2. For a research manuscript prepared for publication but that has not yet been published (if already published, please skip to section 3):	
b) What is the current title of the manuscript?	
c) Has the manuscript been uploaded to a preprint server? (e.g. medRxiv; if 'Yes', please give a link or doi):	
d) Where is the work intended to be published? (e.g. journal names)	
e) List the manuscript's authors in the intended authorship order:	
f) Stage of publication (e.g. in submission):	

3. For multi-authored work, please give a statement of contribution covering all authors (if single-author, please skip to section 4):

A. C. Deshpande was the primary author of this publication, and carried out all the analysis within the work. P.L. Taylor contributed to conceptualising the work, pioneered the k-cut technique that this work uses extensively, and wrote the code used to compute BNT transforms. T. D. Kitching was the supervisor of A. C. Deshpande, and as such conceptualised the work, directed its scope, and informed experimental direction.

4. In which chapter(s) of your thesis can this material be found?

Chapter 5

5. e-Signatures confirming that the information above is accurate (this form should be co-signed by the supervisor/ senior author unless this is not appropriate, e.g. if the paper was a single-author work):

Candidate:	Anurag Chandrahas Deshpande	**Date:**	09/09/2022
Supervisor/ Senior Author (where appropriate):	Thomas Kitching	**Date:**	09/09/2022

Abstract

Two of the fundamental components of the Universe are still poorly understood: dark energy and dark matter. Collectively, these constitute around 95% of the Universe according to our current best measurements. This stresses the need to accurately model them. A particularly powerful probe of these quantities is the effect of weak gravitational lensing. This is the distortion of images of distant galaxies due to the gravitational effects of the large-scale structure of the Universe.

Upcoming weak lensing surveys, known as Stage IV experiments, are poised for more than an order-of-magnitude improvement in cosmological parameter constraining ability. Accordingly, it is paramount that the accuracy of our theoretical models keeps in step. In this thesis, I examine four previously neglected systematic effects, and report on their importance for upcoming experiments, particularly focusing on the most imminent of the Stage IV surveys, the *Euclid* space telescope. I also discuss a potential mitigation strategy for them.

Within this work, I first examine the impact of the reduced shear approximation and magnification bias. Specifically, I evaluate the biases in cosmological inference from neglecting these effects. For these terms, assuming a w_0w_aCDM cosmology, I find significant biases in Ω_m, σ_8, n_s, Ω_DE, w_0, and w_a. I then describe how these two corrections depend on another common approximation; the Limber approximation. I find that the Limber approximation can be safely used when evaluating the reduced shear and magnification bias corrections for Stage IV. Another neglected effect I study is the Doppler-shift of galaxies towards their local over-density. I again find this effect is not significant for a *Euclid*-like experiment. Finally, I report on how a scale-cutting technique, k-cut cosmic shear, can be used to bypass the need for these corrections, without significantly weakening cosmological constraints.

Impact Statement

Over the last three decades, considerable investment has been made at a global level in the *Euclid* and *Nancy Grace Roman* space telescopes, as well as the ground-based Vera Rubin Observatory. These cosmological experiments will begin imminently, and will help model dark energy and dark matter with unprecedented precision. These two phenomena make up approximately 95% of our Universe, and are currently poorly understood.

One of the primary probes that these surveys will use to perform cosmology is weak gravitational lensing. However, the existing theoretical formalism used to model this effect relies on making a plethora of assumptions and neglecting systematic effects. This thesis examines systematic effects which are of concern for these upcoming experiments.

This work studies how four key systematic effects will affect the ability of upcoming weak lensing experiments to perform cosmology: the reduced shear approximation, magnification bias, post-Limber reduced shear and magnification, and Doppler-shifted cosmic shear. By identifying that the reduced shear and magnification bias effects will significantly bias cosmological inference from forthcoming surveys, this work has significant impact on them. It serves to inform the modelling and inference strategy for them, and prevents their results from being significantly biased. It also helps manage resources for these missions, as without the findings of this work, the eventual biased inference would necessitate investigation and a revision of the already constructed inference pipeline to include these effects. Additionally, I present a potential mitigation strategy to deal with these higher-order corrections that could bypass the need to compute them explicitly, further reducing the resources required by these experiments. In this manner, the following investigation could be a strong influence on how imminent weak lensing surveys perform their cosmological inference, and accordingly this work could contribute to better constraining the nature of dark matter and dark energy; one of the most fundamental questions in Physics today.

Acknowledgements

I would like to extend massive thanks to my primary supervisor, Prof. Tom Kitching. His technical guidance, momentum, and, most importantly, kindness and supportiveness have given me an unparalleled foundation for success in this doctorate. Additionally, I am grateful to my secondary supervisor, Prof. Mark Cropper, and my panel chair, Prof. Geraint Jones, for their consistent encouragement and feedback throughout the process.

Another person instrumental to my success was Dr. Peter Taylor. Without our extensive discussions on cosmology when I was just starting out, I would not have been able to hit the ground running as fast as I did. Furthermore, I would like to recognise my collaborators in the *Euclid* Consortium; working with all of whom made me a better developer and cosmologist. Looking further back, I am deeply indebted to all those who nurtured my academic career. Specifically, I am thankful to my supervisors at the European Space Agency, Dr. Pierre Ferruit and Dr. Giovanna Giardino, for giving me an unmatched learning opportunity, and to my Masters supervisor at Imperial College London, Dr. Dave Clements, for recognising my aptitude for astronomy and cosmology early-on.

For reading and providing feedback on this thesis, I thank my examiners, Prof. Daisuke Kawata and Prof. Jonathan Pritchard. For dealing with the considerable administrative load accompanying a PhD, I thank Philippa Elwell and Samantha Babister.

On a personal note, I could not have accomplished as much as I have without the continued encouragement and support of my partner, Iliyana Todorova, and the support and sacrifices of my parents, Chandrahas 'Kishore' Deshpande and Anjali Deshpande. I'd also be remiss in not mentioning the emotional support of our daily feline visitor, Lily. To my friends and colleagues at MSSL, thank you for the great conversation, camaraderie, and post-lunch walks.

"The victory lies in the preparation."

– *Batman Vol. 1 #669*, Morrison, G. 2007.

Contents

List of Tables

List of Figures

Chapter 1
Introduction and Background

The idea that light could be deflected by matter was first formally broached by Sir Isaac Newton, following his establishment of a theory of gravity. He posed the question: "Do not Bodies act upon Light at a distance, and by their action bend its Rays; and is not this action (caeteris paribus) strongest at the least distance?" (Newton 1704). Answering this question proved a challenge, as light was thought to be made up of electromagnetic waves, unaffected by gravitation. A century later, it was suggested that, contrary to being massless, light could be assigned mass (von Soldner 1804). Accordingly, its deflection by massive objects could be calculated using Newtonian mechanics.

However, a more physically motivated solution to the question came with the theory of *General Relativity* (Einstein 1916). Gravity was now described as a geometric property of spacetime, which also accordingly influenced massless light particles. This phenomenon was dubbed *gravitational lensing*. The theory's first successful test came three years later, when a solar eclipse allowed the measurement of the deflection of light rays from distant stars by the Sun (Dyson et al. 1920). In 1979, the first extra-galactic observation of this effect was made when a doubly-imaged quasar being lensed by a galaxy was identified (Walsh et al. 1979). Lensing of this type, where the effect is strong enough to produce multiple images or arcs, came to be known as *strong lensing*. On the other hand, *weak gravitational lensing*, which must be measured statistically, was first detected in 1990; as statistical tangential alignments of

galaxies behind clusters (Tyson et al. 1990).

In the following decade, *cosmic shear*, which is weak lensing by the large-scale structure (LSS) of the universe, was first detected as coherent galaxy distortions in non-cluster fields (Bacon et al. 2000; Kaiser et al. 2000; Van Waerbeke et al. 2000; Wittman et al. 2000). Measuring these distortions allowed for exploration of the nature of the LSS. Cosmic shear as a cosmological probe had arrived. Since its first observations, cosmic shear has become one of the premier tools to study the universe on cosmological scales. Surveys such as CFHTLenS (Heymans et al. 2012), DES (Dark Energy Survey Collaboration 2005), and KiDS (de Jong et al. 2013) have helped us model the geometry of the universe, and the distribution of matter within it, with great precision.

The advent of the next generation of experiments, known as Stage IV (Albrecht et al. 2006), such as *Euclid* (Laureijs et al. 2011), *Roman* (Akeson et al. 2019), and the Rubin Observatory (LSST Science Collaboration et al. 2009) will bring a leap in the precision of our knowledge. For example, even a pessimistic analysis of *Euclid* weak lensing data is projected to increase precision by a factor of $\sim$25 over current surveys (Sellentin & Starck 2019). It must be ensured that the accuracy of our cosmic shear analysis keeps up accordingly. To do so, we must ensure we have a robust understanding of the impact of systematic effects on upcoming surveys. This will be the focus of the thesis. In particular, I will examine four closely related effects that all rely on the three-point angular statistic, the bispectrum, and demonstrate a potential mitigation method. In general, I will quantify these effects in relation to the *Euclid* telescope, or a *Euclid*-like survey, as forecasting specifications for this are readily available (Euclid Collaboration: Blanchard et al. 2020).

For the remainder of this introductory chapter, I describe the cosmological formalism necessary to understand this thesis, as well as how it is used within it. The following four chapters describe the main scientific contributions of this

work. Chapter 2 details the reduced shear approximation and magnification bias; two currently neglected systematic effects that I demonstrate will play an important role in Stage IV experiments. This chapter also details their previously unexplored interaction with the intrinsic alignment of galaxies.

Next, in chapter 3, I show how the corrections for reduced shear and magnification bias are reliant on the Limber approximation, and relax this further. Then, in chapter 4, I present another systematic effect closely related to the reduced shear approximation; the Doppler-shift of galaxies' observed redshifts and the resulting impact on the observed galaxy distributions.

A mitigation strategy that bypasses the need for full computation of these corrections by using the k-cut technique will be discussed in chapter 5; where it is applied to reduced shear. Finally, in chapter 6, I will summarise the main conclusions of this thesis, and discuss future work arising from it.

1.1 Geometry and Contents of the Universe

One of the most important conclusions of General Relativity was that light was subject to gravitation. In this theory, gravity is a geometric property of spacetime. Within this section, I will summarise the basic principles of General Relativity and Universal geometry, and explain how the constituents of the Universe influence this geometry.

1.1.1 Fundamentals of General Relativity

Within the framework of General Relativity, gravity is described by the *Einstein field equations*. These equations describe how the curvature of spacetime, which is represented by the Einstein tensor $G_{\mu\nu}$, is affected by the matter within it, which is represented by the energy-momentum tensor $T_{\mu\nu}$:

$$G_{\mu\nu} = \frac{8\pi G}{c^4} T_{\mu\nu}, \tag{1.1}$$

where G is Newton's constant of gravitation, c is the speed of light in a vacuum, and:

$$G_{\mu\nu} = R_{\mu\nu} - \frac{1}{2}Rg_{\mu\nu}, \tag{1.2}$$

where $R_{\mu\nu}$ is the Ricci curvature tensor, R is the Ricci scalar, $g_{\mu\nu}$ is the metric tensor. The Ricci tensor and scalar are both constructed from the metric tensor; which is the fundamental object that defines the geometric structure of spacetime. Consequently, when there is no matter in the Universe ($T_{\mu\nu} = 0$), the curvature of the Universe also vanishes.

An additional condition in General Relativity is that, analogous to the conservation of energy in Newtonian mechanics, energy-momentum is conserved. Accordingly:

$$\nabla_\mu T_{\mu\nu} = 0, \tag{1.3}$$

where ∇_μ is the covariant derivative.

Generally, in the weak-field limit (when the metric can be considered a perturbation from flat space) the equations of General Relativity simplify to their Newtonian counterparts. A notable exception is the case of gravitational lensing, which will be explored in Section 1.2.1.

1.1.2 The Expansion of the Universe and the Cosmological Constant

A plethora of observational evidence from Type Ia supernovae (Riess et al. 1998; Freedman et al. 2019, and many others) indicates that the Universe is expanding. These supernovae behave as standard candles; meaning that they emit the same intensity of light in their rest frame. Using this information, their distances from us can be calculated. Additionally, observations of their spectra reveal their recession velocities. Through combining these, the expansion of the Universe can be estimated.

Recently, observational evidence has revealed that the expansion of the Universe is, in fact, accelerating (Riess et al. 1998; Perlmutter et al. 1999). The expansion of the Universe can be described via a dimensionless scale factor, $a(t)$, that increases with time; relating a physical distance, d, to a comoving one, r:

$$d = a(t)r. \tag{1.4}$$

Taking the derivative of Equation (1.4), with respect to proper time, produces an expression for the velocity, v at which objects separated by distance d recede from each other:

$$v = H(t)d, \tag{1.5}$$

where $H(t) = \dot{a}/a$. This expression is known as the *Hubble-Lemaître law*, after two of its first proposers: Edwin Hubble (Hubble 1929), and Georges Lemaître (Lemaître 1927).

An important parameter in cosmology is the present-day value of H, which is known as the Hubble constant and denoted by H_0. The value of the Hubble constant is a contentious issue, with contemporary observations of the late and early Universe providing inconsistent values. For an in-depth review of the tension, see Mörtsell & Dhawan (2018). In general, the value is observed to lie between $67 - 75$ kms^{-1}Mpc^{-1} (Planck Collaboration et al. 2020; Freedman et al. 2019; Riess et al. 2019). The Hubble constant is also sometimes expressed as the dimensionless quantity h, where $H_0 = 100h$ kms^{-1}Mpc^{-1}.

The culprit behind the accelerating expansion of the Universe is typically identified as *dark energy*; owing to how little is known about it. One way of expressing this is as a repulsive vacuum energy term added into the Einstein field equations of Equation (1.1):

$$G_{\mu\nu} = \frac{8\pi G}{c^4} T_{\mu\nu} - \Lambda\, g_{\mu\nu}, \tag{1.6}$$

where Λ is the cosmological constant, which determines the strength of the repulsion.

The nature of dark energy and the cosmological constant is one of the major open questions in cosmology, and it is one where cosmic shear proves to be a particularly powerful probe (Albrecht et al. 2006).

1.1.3 Cosmological Redshift and the FLRW Metric

In an expanding Universe, the wavelength of light emitted by a source, $\lambda_{\rm e}$, receding away from an observer is stretched. The wavelength seen by the observer, $\lambda_{\rm o}$, is given by:

$$\lambda_{\rm o} = \frac{a(t_{\rm o})}{a(t_{\rm e})}\lambda_{\rm e}, \tag{1.7}$$

where $a(t_{\rm o})$ and $a(t_{\rm e})$ are the scale factors of the Universe at the observer and the emitter, respectively. This change in the wavelength of emitted light is known as *redshift*. Specifically, redshift as a quantity, z, is:

$$z = \frac{\lambda_{\rm o} - \lambda_{\rm e}}{\lambda_{\rm e}}. \tag{1.8}$$

Substituting Equation (1.8) into Equation (1.7), and rearranging, then provides a conversion between scale factor and redshift:

$$1 + z = \frac{a(t_{\rm o})}{a(t_{\rm e})}. \tag{1.9}$$

Conventionally, $a(t_{\rm o})$ is normalised to 1 at present-day.

In order to formulate a description for the fundamental metric of the Universe, one begins with the assumption of the *cosmological principle*. Under this assumption, the Universe is observed to be, on large scales, homogeneous (statistically the same at all points in space) and isotropic (the same in every direction). Then, the underlying metric of the Universe can be expressed in terms of a set of spatial, comoving, spherical coordinates (r, θ, ϕ), a time

coordinate t, and the scale factor:

$$\mathrm{d}s^2 = -c^2\mathrm{d}t^2 + a^2(t)[\mathrm{d}r^2 + S_K^2(r)(\mathrm{d}\theta^2 + \sin^2\theta\mathrm{d}\phi^2)], \tag{1.10}$$

where $S_K(r)$ is a function that encodes the dependence of the comoving distance on the curvature of the Universe, K, such that:

$$S_K(r) = \begin{cases} |K|^{-1/2}\sin(|K|^{-1/2}\,r) & K > 0 \\ r & K = 0 \\ |K|^{-1/2}\sinh(|K|^{-1/2}\,r) & K < 0. \end{cases} \tag{1.11}$$

The three scenarios describe the effect of curvature in a closed ($K > 0$), flat ($K = 0$), and open ($K < 0$) Universe. Observational evidence generally indicates that our Universe is flat (see e.g. Planck Collaboration et al. 2020). Equation (1.10) is known as the *Friedmann-Lemaître-Robertson-Walker* (FLRW) metric. Using this metric, one can formulate an expression for the comoving distance, in terms of redshift; by considering a *null geodesic*. A *geodesic* is the shortest path between two points in a given geometry, and a *null* geodesic is the path taken by a massless photon. For a radial null geodesic in the FLRW metric:

$$0 = -c^2\mathrm{d}t^2 + a^2(t)\mathrm{d}r^2. \tag{1.12}$$

This can be integrated, and one can apply a change of variables determined from differentiating Equation (1.9) with respect to time, to obtain an expression for the comoving distance:

$$r(z) = \int_0^z \frac{c}{a(t_\mathrm{o})}\frac{\mathrm{d}z'}{H(z')}. \tag{1.13}$$

Another distance commonly used in cosmology that also depends on the metric is angular diameter distance, d_A. This is the ratio of the true physical size of

an object, $r_{\rm phys}$, to the angle which it subtends on the sky, θ, so that:

$$d_{\rm A} = \frac{r_{\rm phys}}{\theta} = \frac{S_K[r(z)]a(z)\theta}{\theta} = S_K[r(z)]a(z). \tag{1.14}$$

For a flat universe with a present-day scale factor of 1, the angular diameter distance is equal to the comoving distance.

1.1.4 The Contents and Evolution of the Universe

In the framework of General Relativity, one can describe the constituents of the Universe as cosmological fluids. For a perfect fluid, in thermodynamic equilibrium, the energy-momentum tensor can be written as:

$$T_{\mu\nu} = \left(\rho + \frac{p}{c^2}\right)u_\alpha u_\beta + p\, g_{\mu\nu}, \tag{1.15}$$

where ρ is the mass-energy density of the fluid, p is its pressure, and u_α is its four-velocity. Applying the conservation of energy-momentum Equation (1.3) to this tensor leads to the *conservation equation*:

$$\frac{\partial \rho}{\partial t} + 3H(\rho + p) = 0. \tag{1.16}$$

In order to describe the relationship between the pressure and density of a cosmological fluid, one can define an *equation of state*:

$$p = w\rho\, c^2. \tag{1.17}$$

Substituting this into Equation (1.16), and rearranging, gives an expression describing the evolution of the density of a fluid with redshift:

$$\rho \propto a^{-3(1+w)}. \tag{1.18}$$

The Universe is typically divided into three such fluids: matter, radiation, and vacuum energy. Each of these components behaves differently, and accordingly has a different equation of state and redshift-evolution.

Matter

The term matter here encompasses both regular baryonic matter, and *dark matter*. In cosmology, baryonic matter refers broadly to all 'ordinary', visible, directly observable matter; including leptons. Meanwhile, dark matter is matter which cannot be observed directly; instead it interacts with light only via gravity. It is theorised to be a particle beyond the standard model of particle physics. In the conventional cosmological model, the cold dark matter (CDM) model, both of these species are taken to be non-relativistic. On cosmological scales, this non-relativistic matter can be treated as collisionless and hence having $p = 0$. Accordingly, the density of matter evolves as: $\rho_{\mathrm{m}} \propto a^{-3}$. Contemporary measurements place the percentage of the Universe made up of matter at 32%, with 5% being baryonic matter and 27% being dark matter (Planck Collaboration et al. 2020).

Radiation

In this case, radiation refers to ultra-relativistic particles with no rest mass; namely, neutrinos[1] and photons. For these particles, radiation pressure leads to an equation of state parameter of $w_r = 1/3$. The density of these species then changes as: $\rho_{\mathrm{r}} \propto a^{-4}$. Because the density of radiation falls more rapidly than that of matter, radiation is only an important component when considering the early Universe, and recent observations place its present-day contribution at 0.01% (Planck Collaboration et al. 2020).

Vacuum Energy

[1] In actuality, recent observations have shown neutrinos have a non-zero, but still very small, mass (Battye & Moss 2014). Accordingly, they are not necessarily relativistic. For a detailed review of the treatment of massive neutrinos, see Lesgourgues & Pastor (2006).

The third component of the Universe is the vacuum energy (or dark energy) of the cosmological constant, as described in Section 1.1.2. Being a constant, it is time-invariant which means that $\partial\rho_\Lambda/\partial t = 0$. Equation (1.16) then dictates that $w_\Lambda = -1$. Consequently, $\rho_\Lambda \propto a^0$ and vacuum energy dominates in the Universe at late times. In fact, the latest results place this dark energy as making up 68% of the Universe today (Planck Collaboration et al. 2020).

1.1.5 The Friedmann Equations

One can now construct expressions for the evolution of the scale factor of the Universe with relation to the density of its constituents. To do so, the FLRW metric of Equation (1.10), and the energy-momentum tensor of cosmological fluids of Equation (1.15), are substituted into the Einstein field equations, described by Equation (1.1). The results of this procedure are the *Friedmann equations*:

$$H^2 = \frac{8\pi G}{3}\rho - \frac{Kc^2}{a^2} \tag{1.19}$$

$$\frac{\ddot{a}}{a} = -\frac{4\pi G}{c^2}(\rho + 3p), \tag{1.20}$$

where $\ddot{}$ represents the second-derivative with respect to proper time. Then, using Equation (1.19) one can define a critical density, $\rho_{\rm crit}$, when the Universe is flat ($K = 0$). Since this is the case in the present-day, the critical density is:

$$\rho_{\rm crit} = \frac{3H_0^2}{8\pi G}. \tag{1.21}$$

In cosmology, the three fluid densities are often reported in terms of this value. The following dimensionless densities are typically used: $\Omega_{i;0} = \rho_i/\rho_{\rm crit}$, where $i \in \{\rm m, r, \Lambda\}$. The 0 in the subscript signifies that it is the present-day value. However, it is convention to drop this. Accordingly, throughout the remainder of this thesis, the present-day dimensionless densities are represented by

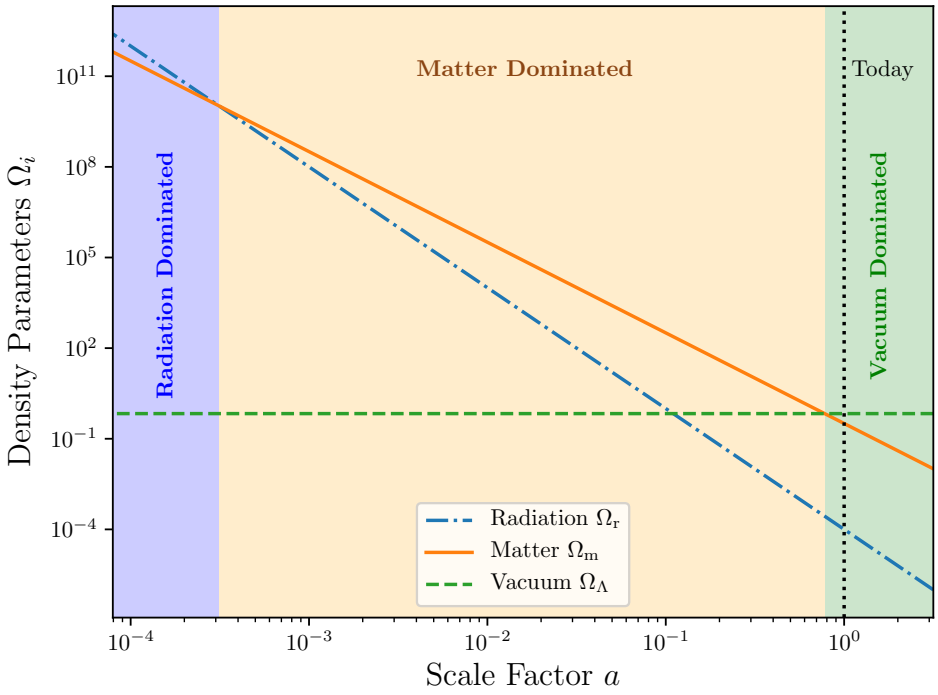

Figure 1.1: Evolution of the dimensionless density parameters of the three cosmological fluids with scale factor. The Universe can be divided into three eras: a period of radiation dominance, followed by matter dominance, and finally our current era of vacuum energy dominance.

Ω_i. The first Friedmann equation can then be expressed in terms of these dimensionless quantities, so that Equation (1.19) becomes:

$$H^2 = H_0^2(\Omega_\mathrm{m} a^{-3} + \Omega_\mathrm{r} a^{-4} + \Omega_\Lambda + \Omega_K a^{-2}), \tag{1.22}$$

where $\Omega_K = -K(c/H_0)^2$. Using the present-day values of these parameters, the evolution of the Universe can be charted. The changing densities of the Universe's individual components are shown in Figure 1.1. Three distinct eras become apparent: the early universe where radiation dominates, then an extended period of matter dominance, followed finally by our current era where the cosmological constant makes up most of the Universe.

1.1.6 The Dark Energy Equation of State

Given how little is known about dark energy, in cosmology we also investigate the possibility that dark energy deviates from simply being a cosmological constant. In order to do so, the Chevallier-Polarski-Linder (CPL) parameterisation for the dark energy equation of state parameter (Linder 2005) is typically adopted:

$$w_{\rm DE}(a) = w_0 + w_a(1-a), \tag{1.23}$$

where w_a modifies the equation of state at early times. This parameterisation is the result of a Taylor expansion around $a = 1$, and accordingly is not theoretically or observationally motivated. If either $w_0 \neq -1$ or $w_a \neq 0$, then dark energy cannot be explained by a cosmological constant.

When dark energy is represented by the CPL equation, then the expansion history of the Universe is different. In this case, Equation (1.16) becomes:

$$\frac{\mathrm{d}\ln(\rho_{\rm DE})}{\mathrm{d}\ln(a)} = -3(1+w_{\rm DE}). \tag{1.24}$$

Solving this equation leads to:

$$\rho_{\rm DE} \propto \exp\left[-3\int_1^a (1+w_{\rm DE})\mathrm{d}\ln(a')\right] \tag{1.25}$$

This expression for density then leads to a changed first Friedmann equation, replacing Equation (1.22) with:

$$H^2 = H_0^2\left(\Omega_{\rm m}a^{-3} + \Omega_{\rm r}a^{-4} + \Omega_\Lambda \exp\left[-3\int_1^a (1+w_{\rm DE})\mathrm{d}\ln(a')\right]\right), \tag{1.26}$$

where Ω_K has been set to 0 for compactness.

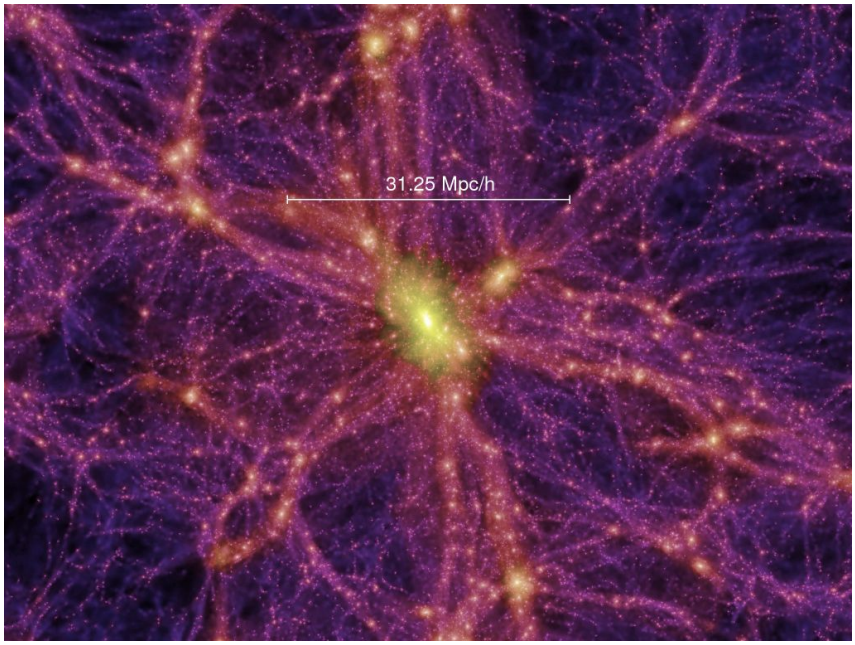

Figure 1.2: Simulation of the cosmic web, showing filaments of galaxies with voids in between. At the centre is a galaxy cluster. Adapted from Springel et al. (2005).

1.1.7 Structure Formation

On cosmological scales, it is assumed that the Universe is homogeneous. However, this is demonstrably untrue on smaller scales, as the Universe is full of structures such as galaxies, stars, and planets. In fact, the Universe itself has structure on large scales. Mass-energy in the Universe tends to cluster together in a 'cosmic web' of filaments and voids. Figure 1.2 shows a simulation of this LSS.

This structure begins as inhomogeneities in the initial mass-energy distribution at the time of the Big Bang resulting from quantum fluctuations. These perturbations can be written as a fractional overdensity, δ, at some point in space, $\boldsymbol{x}$:

$$\delta(\boldsymbol{x}) = \frac{\rho(\boldsymbol{x}) - \bar{\rho}}{\bar{\rho}}, \tag{1.27}$$

where $\bar{\rho}$ is the mean density of the Universe. These perturbations then grow into the LSS we see today through gravitational collapse. One can model this structure growth using linear perturbation theory. The discussion here follows

Weinberg (2007). For large scales, one can operate in the Newtonian limit. In this case, the following equations govern the density and velocity of an ideal fluid:

$$\text{Continuity equation: } \left(\frac{\partial \rho}{\partial t}\right)_{\boldsymbol{x}} + \nabla_{\boldsymbol{x}} \cdot (\rho \boldsymbol{u}) = 0, \tag{1.28}$$

$$\text{Euler equation: } \left(\frac{\partial \boldsymbol{u}}{\partial t}\right)_{\boldsymbol{x}} + (\boldsymbol{u} \cdot \nabla_{\boldsymbol{x}})\boldsymbol{u} = -\nabla_{\boldsymbol{x}} \Phi, \tag{1.29}$$

where Φ is the Newtonian gravitational potential, and I ignore pressure gradients in the Euler equation, since in a dark matter dominated Universe, there is no pressure. The other relevant equation is the Poisson equation for gravity:

$$\nabla^2_{\boldsymbol{x}} \Phi = 4\pi G \rho. \tag{1.30}$$

I now perform a transformation of variables to comoving distance $\boldsymbol{r} = \boldsymbol{x}/a$, and peculiar velocity $\boldsymbol{v} = \boldsymbol{u} - (\dot{a}/a)\boldsymbol{x} = \dot{(a\boldsymbol{r})} - \dot{a}\boldsymbol{r} = a\dot{\boldsymbol{r}}$. A mathematical identity to note at this stage is the time derivative of some function, f, at a given comoving distance. From the chain rule:

$$\left(\frac{\partial f}{\partial t}\right)_{\boldsymbol{r}} = \left(\frac{\partial f}{\partial t}\right)_{\boldsymbol{x}} + \left(\frac{\partial \boldsymbol{x}}{\partial t}\right)_{\boldsymbol{r}} \cdot \nabla_{\boldsymbol{x}} f = \left(\frac{\partial f}{\partial t}\right)_{\boldsymbol{x}} + \frac{\dot{a}}{a}\frac{\boldsymbol{x}}{a} \cdot (a \nabla_{\boldsymbol{x}} f). \tag{1.31}$$

Rearranging yields:

$$\left(\frac{\partial f}{\partial t}\right)_{\boldsymbol{x}} = \left(\frac{\partial f}{\partial t}\right)_{\boldsymbol{r}} - \frac{\dot{a}}{a}\boldsymbol{r} \cdot \nabla f, \tag{1.32}$$

where $\nabla \equiv a\nabla_{\boldsymbol{r}}$. Now, making the necessary substitutions leads to:

$$\text{Continuity equation: } \frac{\partial \delta}{\partial t} + \frac{1}{a}\nabla \cdot [(1+\delta)\boldsymbol{v}] = 0, \tag{1.33}$$

$$\text{Euler equation: } \frac{\partial \boldsymbol{v}}{\partial t} + \frac{1}{a}(\boldsymbol{v} \cdot \nabla)\boldsymbol{v} + \frac{\dot{a}}{a}\boldsymbol{v} = -\frac{1}{a}\nabla \phi, \tag{1.34}$$

$$\text{Poisson equation: } \nabla^2 \phi = 4\pi G \bar{\rho} a^2 \delta, \tag{1.35}$$

where $\phi = \Phi - 2/3\pi G\bar{\rho}a^2x^2$. I then keep only the terms that are first-order in δ or $\boldsymbol{v}$, as the linear approximation is being made here:

$$\text{Continuity equation: } \frac{\partial\delta}{\partial t} + \frac{1}{a}\nabla\cdot\boldsymbol{v} = 0, \tag{1.36}$$

$$\text{Euler equation: } \frac{\partial\boldsymbol{v}}{\partial t} + \frac{\dot{a}}{a}\boldsymbol{v} + \frac{1}{a}\nabla\phi = 0. \tag{1.37}$$

Taking the time derivative of Equation (1.36), $1/a \times$ the divergence of Equation (1.37), subtracting, and using the Poisson equation gives:

$$\ddot{\delta} + 2\frac{\dot{a}}{a}\dot{\delta} = 4\pi G\bar{\rho}\delta. \tag{1.38}$$

For the pressure-less dark matter dominated Universe, structure therefore grows as:

$$\delta \propto a, \tag{1.39}$$

while in cosmological constant dominated times:

$$\delta \propto \text{constant}. \tag{1.40}$$

Equation (1.39) and Equation (1.40) characterise growth on large and linear scales for the majority of the history of the Universe. In the matter dominated era, structure will grow with the scale factor, but after dark energy dominance, this LSS growth will be 'frozen out'. Once in the non-linear regime, on small scales, structure growth becomes difficult to describe. Large N-body simulations become necessary to model this.

1.2 Cosmic Shear

When light from distant galaxies travels towards us, it experiences weak gravitational lensing from all of the LSS along the line-of-sight. Accordingly, the images that we observe for these sources are distorted. This distortion is known

as cosmic shear. By measuring the distortion we can map the LSS, and accordingly interpret fundamental properties of the Universe. In this section, I will review the theory behind cosmic shear and how we can use it as a cosmological probe.

1.2.1 Light Deflection in General Relativity

In General Relativity, gravity is a geometric property of spacetime. As a consequence, it also affects light. Using Fermat's principle, the metric for the Universe, and Lagrangian mechanics, the deflection angle of a photon under the gravitational force of some mass-energy can be calculated. Here, I follow Meneghetti (2016) in my derivation.

According to Fermat's principle, the travel time of light through some medium with refractive index, n, is:

$$t = \frac{1}{c}\int n[\boldsymbol{x}(l)]\mathrm{d}l, \tag{1.41}$$

where c is the speed of light in a vacuum. This is extremised along the path $\boldsymbol{x}(l)$ between fixed points A and B such that:

$$\delta t = \delta\left[\frac{1}{c}\int_A^B n[\boldsymbol{x}(l)]\mathrm{d}l\right] = 0. \tag{1.42}$$

Now, one can consider what happens to the path of the light in the presence of a gravitational lens with Newtonian potential Φ. The metric for a static potential is:

$$\mathrm{d}s^2 = \left(1+\frac{2\Phi}{c^2}\right)c^2\mathrm{d}t^2 - \left(1-\frac{2\Phi}{c^2}\right)\mathrm{d}\boldsymbol{x}^2. \tag{1.43}$$

Since a photon experiences zero proper time, $\mathrm{d}s = 0$, and Equation (1.43) can be rearranged to give the effective speed of light in the gravitational field, c':

$$c' = \frac{|\mathrm{d}\boldsymbol{x}|}{\mathrm{d}t} = c\sqrt{\frac{1+\frac{2\Phi}{c^2}}{1-\frac{2\Phi}{c^2}}} \approx c\left(1+\frac{2\Phi}{c^2}\right), \tag{1.44}$$

where the 'weak-lens approximation' has been made, under which $\Phi \ll c^2$; an assumption that is valid in virtually all astrophysical cases. Accordingly, the refractive index is:

$$n = \frac{c}{c'} = \frac{1}{1 + \frac{2\Phi}{c^2}} \approx 1 - \frac{2\Phi}{c^2}. \tag{1.45}$$

This can now be treated as a variational problem, as in conventional optics. In this case, I recast the path of light in terms of an arbitrary parameter, λ, so that:

$$\mathrm{d}l = \left|\frac{\mathrm{d}\boldsymbol{x}}{\mathrm{d}\lambda}\right| \mathrm{d}\lambda = |\dot{\boldsymbol{x}}| \mathrm{d}\lambda. \tag{1.46}$$

With this, Equation (1.42) can be rewritten:

$$\delta\left[\frac{1}{c}\int_{\lambda_A}^{\lambda_B} n[\boldsymbol{x}(l)]|\dot{\boldsymbol{x}}|\mathrm{d}\lambda\right] = 0, \tag{1.47}$$

where the Lagrangian of the variational problem is $\mathcal{L} = n[\boldsymbol{x}(l)]|\dot{\boldsymbol{x}}|$. Now, I consider the equations of motion given by the *Euler-Lagrange equations*:

$$\frac{\mathrm{d}}{\mathrm{d}\lambda}\left(\frac{\partial \mathcal{L}}{\partial \dot{\boldsymbol{x}}}\right) - \frac{\partial \mathcal{L}}{\partial \boldsymbol{x}} = 0, \tag{1.48}$$

where:

$$\frac{\partial \mathcal{L}}{\partial \dot{\boldsymbol{x}}} = n\frac{\dot{\boldsymbol{x}}}{|\dot{\boldsymbol{x}}|} \tag{1.49}$$

$$\frac{\partial \mathcal{L}}{\partial \boldsymbol{x}} = |\dot{\boldsymbol{x}}|\frac{\partial n}{\partial \boldsymbol{x}} = |\dot{\boldsymbol{x}}|\boldsymbol{\nabla} n. \tag{1.50}$$

The vector $\dot{\boldsymbol{x}}$ is tangential to the light path, and it can be normalised by choosing a value for λ such that $|\dot{\boldsymbol{x}}| = 1$. In this case, the unit tangent vector $\boldsymbol{e} \equiv \dot{\boldsymbol{x}}$. Equation (1.48) then becomes:

$$\frac{\mathrm{d}}{\mathrm{d}\lambda}(n\boldsymbol{e}) - \boldsymbol{\nabla} n = 0, \tag{1.51}$$

which can be expanded, and rearranged to give:

$$n\dot{\boldsymbol{e}} = \boldsymbol{\nabla} n - \boldsymbol{e}(\boldsymbol{\nabla} n \cdot \boldsymbol{e}). \tag{1.52}$$

The second term on the right-hand side of this equation is $\boldsymbol{\nabla}_{\parallel} n$ which means that the entire right-hand side is $\boldsymbol{\nabla}_{\perp} n$. This leads to:

$$\dot{\boldsymbol{e}} = \frac{1}{n}\boldsymbol{\nabla}_{\perp} n = \boldsymbol{\nabla}_{\perp} \ln n. \tag{1.53}$$

As I am operating in the weak-lens limit, I can Taylor expand the natural logarithm to the first-order, $\ln n \approx -2\Phi/c^2$, so that:

$$\dot{\boldsymbol{e}} \approx -\frac{2}{c^2}\boldsymbol{\nabla}_{\perp}\Phi. \tag{1.54}$$

By integrating this expression over the light path, the total deflection angle of the light, $\boldsymbol{\alpha}$, can be determined:

$$\boldsymbol{\alpha} = -\frac{2}{c^2}\int_{\lambda_A}^{\lambda_B} \boldsymbol{\nabla}_{\perp}\Phi \mathrm{d}\lambda. \tag{1.55}$$

Using this expression still proves difficult, as it requires knowledge of the light's true path.

However, the weak-lens approximation means that one would expect the deflection angle to be small. Accordingly, I can make the *Born approximation*, within which one integrates the potential in Equation (1.55) along the unperturbed path. Now, if one considers a photon traveling parallel to the z direction, this expression becomes:

$$\boldsymbol{\alpha} = -\frac{2}{c^2}\int_{0}^{\infty} \boldsymbol{\nabla}_{\perp}\Phi \mathrm{d}z. \tag{1.56}$$

In the study of cosmic shear, this approximated expression is used to calculate

the gravitational deflection caused by the LSS.

1.2.2 The Lens Equation

To consider gravitational lensing of galaxy images on cosmological scales, I begin by examining the difference between two neighbouring geodesics. In this section, the standard derivations from the review articles of Kilbinger (2015), and Bartelmann & Schneider (2001) are followed.

Assuming the FLRW metric and the small angle approximation, the comoving separation between two rays, $\boldsymbol{x}_0$, seen by an observer over angle, $\boldsymbol{\theta}$, as a function of the comoving distance to them, χ, is:

$$\boldsymbol{x}_0(\chi) = S_K(\chi)\boldsymbol{\theta}. \tag{1.57}$$

Now, when these light rays from a source at comoving distance χ encounter a source of gravity at comoving distance χ', their separation changes by $\mathrm{d}\boldsymbol{x}$. This scenario is illustrated in Figure 1.3. The change in separation is given by:

$$\mathrm{d}\boldsymbol{x} = S_K(\chi - \chi')\mathrm{d}\boldsymbol{\alpha}. \tag{1.58}$$

Integrating over the line-of-sight along χ' then provides the total separation. Under the Born approximation, the separation is:

$$\boldsymbol{x}(\chi) = S_K(\chi)\boldsymbol{\theta} - \frac{2}{c^2}\int_0^{\chi} S_K(\chi - \chi')\boldsymbol{\nabla}_{\perp}\Phi(S_K(\chi')\boldsymbol{\theta}, \chi')\mathrm{d}\chi'. \tag{1.59}$$

Additionally, in the absence of lensing, if $\boldsymbol{x}$ was some unperturbed separation, the observer would view it over angle $\boldsymbol{\beta}$:

$$\boldsymbol{\beta} = \frac{\boldsymbol{x}(\chi)}{S_K(\chi)}. \tag{1.60}$$

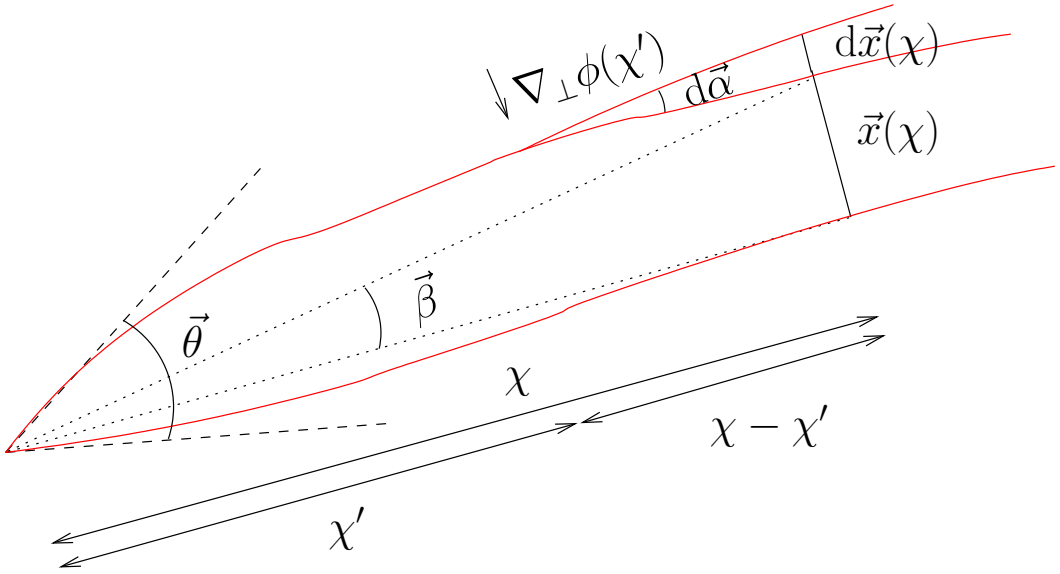

Figure 1.3: Illustration of the propagation of two light rays (solid, red lines) originating at comoving distance χ, experiencing a gravitational potential, ϕ, of a deflector at comoving distance, χ', and being deflected to converge at the observer. The dotted lines are the unperturbed geodesics that the light would take in the absence of a deflector, and they define the angle, $\vec{\beta}$ under which the observer would have seen the unperturbed comoving separation, $\vec{x}$. Meanwhile, the dashed lines show the apparent direction of the light rays to the observer, defining the angle $\vec{\theta}$. Adapted from Kilbinger (2015).

This angle can be defined by the *lens equation*:

$$\boldsymbol{\beta} = \boldsymbol{\theta} - \boldsymbol{\alpha}, \tag{1.61}$$

where:

$$\boldsymbol{\alpha} = \frac{2}{c^2}\int_0^\chi \frac{S_K(\chi - \chi')}{S_K(\chi)} \boldsymbol{\nabla}_\perp \Phi[S_K(\chi')\boldsymbol{\theta}, \chi'] \mathrm{d}\chi'. \tag{1.62}$$

Equation (1.61) is analogous to the lens equation from conventional optics for a single, thin lens.

1.2.3 Shear and Convergence

To obtain the quantities of interest in cosmic shear, *shear* and *convergence*, one begins by linearising Equation (1.61). Next, I define the amplification matrix

as the Jacobian $\boldsymbol{A} = \partial\boldsymbol{\beta}/\partial\boldsymbol{\theta}$ which has the components:

$$\begin{aligned} A_{ij} &= \frac{\partial\beta_i}{\partial\theta_j} = \delta_{ij} - \frac{\partial\alpha_i}{\partial\theta_j} \\ &= \delta_{ij} - \frac{2}{c^2}\int_0^\chi \frac{S_K(\chi-\chi')S_K(\chi')}{S_K(\chi)}\frac{\partial^2}{\partial x_i \partial x_j}\Phi[S_K(\chi')\boldsymbol{\theta},\chi']\mathrm{d}\chi'. \end{aligned} \tag{1.63}$$

The amplification matrix gives the linear mapping from lensed coordinates, $\boldsymbol{\theta}$, to unlensed coordinates, $\boldsymbol{\beta}$. Under the approximations made, the deflection angle can be written as the gradient of a two-dimensional lensing potential, ψ:

$$\psi(\boldsymbol{\theta},\chi) = \frac{2}{c^2}\int_0^\chi \frac{S_K(\chi-\chi')}{S_K(\chi)S_K(\chi')}\Phi[S_K(\chi')\boldsymbol{\theta},\chi']\mathrm{d}\chi'. \tag{1.64}$$

In this case, the amplification matrix can be written:

$$A_{ij} = \delta_{ij} - \partial_i\partial_j\psi, \tag{1.65}$$

where the ∂_i are the partial derivatives with respect to $\boldsymbol{\theta}$.

Now, the individual elements of the amplification matrix can be written in terms of the convergence, κ, and the spin-two shear, $\gamma = \gamma_1 + \mathrm{i}\gamma_2 = |\gamma|\exp(2\mathrm{i}\vartheta)$, where ϑ is the polar angle between the two components. In this framing, the matrix is written:

$$\boldsymbol{A} = \begin{pmatrix} 1-\kappa-\gamma_1 & -\gamma_2 \\ -\gamma_2 & 1-\kappa+\gamma_1 \end{pmatrix}. \tag{1.66}$$

Accordingly, the convergence and shear can be defined in terms of derivatives of the lensing potential:

$$\kappa = \frac{1}{2}(\partial_1\partial_1 + \partial_2\partial_2)\psi = \frac{1}{2}\boldsymbol{\nabla}^2\psi \tag{1.67}$$

$$\gamma_1 = \frac{1}{2}(\partial_1\partial_1 - \partial_2\partial_2)\psi \tag{1.68}$$

$$\gamma_2 = \partial_1\partial_2\psi. \tag{1.69}$$

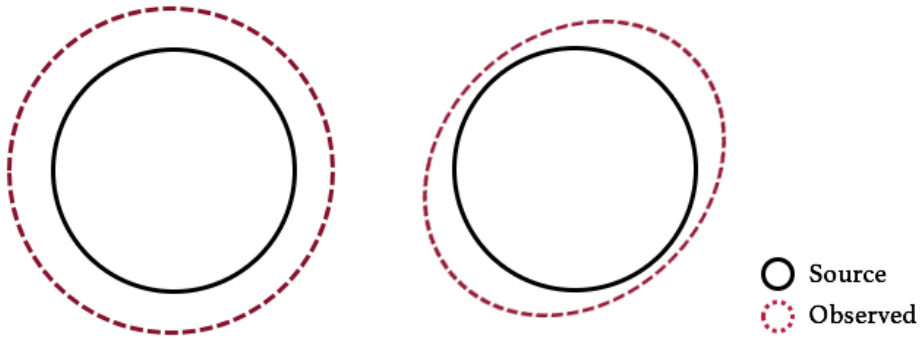

Figure 1.4: Illustrations of the two manifestations of weak lensing from the LSS; convergence (left) and shear (right). The observed shape of an initially circular source, after undergoing these effects, is shown.

The convergence and shear correspond to two different types of changes in the shape of an observed distribution of light. The shear, being the trace-free part of the matrix, represents an anisotropic stretching that would turn a circular distribution of light elliptical, whereas the convergence, which is the diagonal of the matrix, is an isotropic increase or decrease in the size of the image. The difference between these two components is illustrated in Figure 1.4.

The inverse amplification matrix, $\boldsymbol{A}^{-1}$, gives the local mapping from the source plane to image coordinates, and is given by:

$$\boldsymbol{A}^{-1} = \mu(1-\kappa)\left[I_2 + g\begin{pmatrix}\cos 2\vartheta & \sin 2\vartheta \\ \sin 2\vartheta & -\cos 2\vartheta\end{pmatrix}\right], \tag{1.70}$$

where I_2 is the two-dimensional identity matrix, $\mu = 1/\det\boldsymbol{A}$ is the magnification which is the size of the of the image at the observer relative to its size at the source, and g is a quantity known as *reduced shear*:

$$g = \frac{\gamma}{1-\kappa}. \tag{1.71}$$

Each source is mapped uniquely onto one image, and there are no multiple images as is the case in strong lensing.

The convergence and shear encode cosmological information about the Universe, because they are projections of the fractional overdensity of the Universe as given by Equation (1.27). Applying the Laplacian in the definition of convergence, Equation (1.67), to the lensing potential, and recalling the Poisson equation relating the gravitational potential and the fractional overdensity, Equation (1.35), leads to:

$$\kappa(\boldsymbol{\theta}, \chi) = \frac{3H_0^2\Omega_\mathrm{m}}{2c^2} \int_0^\chi \frac{1}{a(\chi')} \frac{S_K(\chi - \chi')S_K(\chi')}{S_K(\chi)} \delta(S_K(\chi')\boldsymbol{\theta}, \chi')\mathrm{d}\chi'. \tag{1.72}$$

To obtain the mean convergence from a population of galaxies, I weight Equation (1.72) with the galaxy probability distribution, $n(\chi)$, so that:

$$\kappa(\boldsymbol{\theta}) = \int_0^{\chi_\mathrm{lim}} n(\chi)\kappa(\boldsymbol{\theta}, \chi)\mathrm{d}\chi = \int_0^{\chi_\mathrm{lim}} W(\chi)\delta(S_K(\chi)\boldsymbol{\theta}, \chi)\mathrm{d}\chi, \tag{1.73}$$

where χ_lim is the limiting comoving distance of the galaxy survey, and $W(\chi)$ is the *lensing kernel*; which dictates the strength of the lensing by the combined background galaxy distribution at a comoving distance χ according to:

$$W(\chi) = \frac{3H_0^2\Omega_\mathrm{m}}{2c^2} \frac{S_K(\chi)}{a(\chi)} \int_\chi^{\chi_\mathrm{lim}} n(\chi') \frac{S_K(\chi' - \chi)}{S_K(\chi')} \mathrm{d}\chi'. \tag{1.74}$$

1.2.4 Measuring the Shear

In practice, the shear is the directly probed quantity, from which the convergence is calculated. In order to measure the shear, the change in the ellipticity of galaxies must be measured. To this end, the observed ellipticity of a galaxy, ε_obs, can be related to its source ellipticity, ε_src, by:

$$\varepsilon_\mathrm{obs} = \frac{\varepsilon_\mathrm{src} + g}{1 + g^*\varepsilon_\mathrm{src}}, \tag{1.75}$$

where * denotes the complex conjugate. Images are very weakly lensed by the LSS, and consequently $|\kappa|, |\gamma| \ll 1$ for individual sources.

Accordingly, it is standard procedure to make the *reduced shear approximation*, where $g \approx \gamma$. Then, Equation (1.75) becomes:

$$\varepsilon_{\rm obs} \approx \varepsilon_{\rm src} + \gamma. \tag{1.76}$$

A complication arises, however, from the fact that the shear of individual sources is beyond the realm of detection. The cosmic shear distortion for an individual source is typically $\gamma \sim 0.03$, while the intrinsic ellipticity RMS uncertainty is $\sigma_\varepsilon \sim 0.3$ (Kilbinger 2015). Therefore, to achieve a signal-to-noise ratio above one, the ensemble average of the ellipticity of the source must be taken. Naturally, we do not have an ensemble of universes readily available with which to carry out this operation. Fortunately, it can be safely assumed that the Universe is *ergodic*; meaning that the ensemble average is equivalent to averaging over a large number of sources in a sufficiently large volume.

Now, in the absence of any preferred intrinsic orientation for galaxies, the average source ellipticity will be zero, and so:

$$\langle \varepsilon_{\rm obs} \rangle \approx \langle \gamma \rangle. \tag{1.77}$$

However, the shear is a projection of the fractional overdensity, and accordingly $\langle \gamma \rangle \propto \langle \delta \rangle = 0$. In fact, the first non-trivial statistics of shear are its second-order statistics.

1.2.5 E-modes and B-modes

Because the two shear components, as defined in Equation (1.68) and Equation (1.69), are functions of a single scalar potential, they are not independent. Accordingly, the shear field is limited in the forms it can take.

To explore the available configurations, one can begin by defining a new vector field, $\boldsymbol{u}$:

$$\boldsymbol{u} = \boldsymbol{\nabla}\kappa. \tag{1.78}$$

Then, by definition, the curl of $\boldsymbol{u}$, $\boldsymbol{\nabla} \times \boldsymbol{u} = 0$. Now, substituting Equation (1.67), Equation (1.68), and Equation (1.69) into the curl yields a constraint on the shear field:

$$\partial_1\gamma_2 - \partial_2\gamma_2 = \partial_1\partial_2\gamma_1 = 0. \tag{1.79}$$

A shear field that satisfies this constraint is curl-free, and is known as an *E-mode* field, by analogy to the electric field in electromagnetism. However, in reality, the observed shear field generally has a curl component. This component is labelled the *B-mode* field, and occurs due to unaccounted for, higher-order systematic effects within the data. Detection of B-modes can be used as a measure of the quality of instrumentation and data analysis. However, it is important to note that this will only account for systematic effects that produce B-modes, and does not preclude the presence of systematic effects that do not produce these modes. Additionally, in spherical harmonic space, the two shear components, γ^α, can be trivially related to the convergence via:

$$\widetilde{\gamma}^\alpha(\boldsymbol{\ell}) = T^\alpha(\boldsymbol{\ell})\,\widetilde{\kappa}(\boldsymbol{\ell}), \tag{1.80}$$

where $\boldsymbol{\ell}$ is the spherical harmonic conjugate of $\boldsymbol{\theta}$ with magnitude ℓ and polar angle ϕ_ℓ. In this expression, the *flat-sky* approximation is made; meaning the impact of the curvature of the sky is neglected. This has a negligible impact on inference (Kitching et al. 2017). The T^α are trigonometric weighting functions:

$$T^1(\boldsymbol{\ell}) = \cos(2\phi_\ell), \tag{1.81}$$

$$T^2(\boldsymbol{\ell}) = \sin(2\phi_\ell). \tag{1.82}$$

This now allows for the mathematical definition of E-modes and B-modes. For an arbitrary shear field (for example one estimated from data), these are expressed as linear combinations of the shear components:

$$\widetilde{E}(\boldsymbol{\ell}) = \sum_{\alpha} T^{\alpha}\, \widetilde{\gamma}^{\alpha}(\boldsymbol{\ell}), \tag{1.83}$$

$$\widetilde{B}(\boldsymbol{\ell}) = \sum_{\alpha} \sum_{\beta} \varepsilon^{\alpha\beta}\, T^{\alpha}(\boldsymbol{\ell})\, \widetilde{\gamma}^{\beta}(\boldsymbol{\ell}), \tag{1.84}$$

where $\varepsilon^{\alpha\beta}$ is the Levi-Civita symbol (i.e. $\varepsilon^{12} = -\varepsilon^{21} = 1$ and $\varepsilon^{11} = \varepsilon^{22} = 0$).

1.2.6 Weak Lensing Power Spectra

In the study of cosmic shear, we typically utilise the second-order statistic of shear in spherical harmonic space for inference. This is the angular power spectrum of convergence, C_ℓ, and is defined:

$$\langle \widetilde{E}(\boldsymbol{\ell}) \widetilde{E}(\boldsymbol{\ell'}) \rangle = (2\pi)^2 \delta_{\mathrm{D}}(\boldsymbol{\ell} - \boldsymbol{\ell'}) C_\ell(\ell), \tag{1.85}$$

where δ_{D} is the Dirac delta.

One can obtain an expression for the angular power spectrum, in terms of the underlying cosmology, by taking the square of Equation (1.73) in spherical harmonic space, substituting the result into Equation (1.85), and using the *Limber approximation* (Limber 1953; LoVerde & Afshordi 2008). This approximation is a mathematical convenience that involves replacing computationally intensive integrals of spherical Bessel functions with delta functions at their peak. Then, the convergence angular power spectrum is:

$$C_\ell = \int_0^{\chi_{\mathrm{lim}}} \frac{W(\chi)^2}{S_K^2} P_\delta[k = (\ell + 1/2)/S_K, \chi]\, \mathrm{d}\chi, \tag{1.86}$$

where P_δ is the three-dimensional matter power spectrum, and $k = (\ell + 1/2)/S_K(\chi)$ under the Limber approximation (LoVerde & Afshordi 2008). Ad-

ditionally, Equation (1.80) leads to the fact that, under the flat-sky approximation, the convergence angular power spectrum is equal to the shear angular power spectrum.

Equation (1.86) provides only two-dimensional information, as it integrates over comoving distance. However, it is possible to retain three-dimensional information through a technique known as *tomography*. In this framework, the galaxies observed in a survey are divided into tomographic bins in redshift. Then for each of the bins and bin combinations, auto and cross-correlation angular power spectra are calculated. In this way, a three-dimensional, redshift-dependent picture is obtained. The auto and cross-correlation spectra for two bins, i and j, are given by:

$$C_{\ell;ij} = \int_0^{\chi_{\rm lim}} \frac{W_i(\chi) W_j(\chi)}{S_K(\chi)^2} P_{\delta\delta}(k, \chi)\, \mathrm{d}\chi, \tag{1.87}$$

where W_i is the lensing kernel for bin i, with definition:

$$W_i(\chi) = \frac{3H_0^2\Omega_{\rm m}}{2c^2} \frac{S_K(\chi)}{a(\chi)} \int_\chi^{\chi_{\rm lim}} n_i(\chi') \frac{S_K(\chi' - \chi)}{S_K(\chi')} \mathrm{d}\chi', \tag{1.88}$$

where now n_i is the probability distribution of galaxies within bin i. In practice, the observed angular power spectra also consist of additional terms resulting from astrophysical effects. These signals must be carefully accounted for to properly extract the cosmological information.

1.2.7 Shot Noise

The dominant portion of the observed lensing power spectrum consists of *shot noise*. This signal is the result of the intrinsic dispersion of the ellipticities of galaxies. For cross-correlation spectra this term is zero, because the ellipticities of galaxies at different comoving distances should be uncorrelated. However, it is non-zero for auto-correlation spectra. As the shot noise is the result of

the shear field being Poisson sampled at the positions of observed galaxies, it scales inversely with the number of galaxies in the survey.

In the case of a tomographic galaxy survey utilising equi-populated redshift bins, the shot noise, $N_{l;ij}$, is (Euclid Collaboration: Blanchard et al. 2020):

$$N^{\epsilon}_{l;ij} = \frac{\sigma^2_{\epsilon}}{\bar{n}_{\rm g}/N_{\rm bin}}\delta^{\rm K}_{ij}, \tag{1.89}$$

where σ^2_{ϵ} is the variance of the observed ellipticities in the galaxy sample, $\bar{n}_{\rm g}$ is the galaxy surface density of the survey, $N_{\rm bin}$ is the number of tomographic bins used, and $\delta^{\rm K}_{ij}$ is the Kronecker delta. Typically, $\sigma_{\epsilon} \approx 0.3$. For a detailed derivation of shot-noise, see Appendix A.

1.2.8 Intrinsic Alignments

Another astrophysical signal that must be disentangled from the cosmic shear signal comes from the *intrinsic alignments* (IA) of galaxies. When galaxies form near each other, they do so in a similar tidal environment. These tidal processes can induce a preferred, intrinsically correlated, alignment of galaxy shapes (Joachimi et al. 2015; Kirk et al. 2015; Kiessling et al. 2015).

To first-order, this acts as an additional contribution to the observed ellipticity of a galaxy, $\varepsilon_{\rm obs}$. Under the reduced shear approximation, this can be written as:

$$\varepsilon_{\rm obs} = \gamma + \gamma^{\rm I} + \varepsilon_{\rm src}, \tag{1.90}$$

where γ is the gravitational lensing shear, $\gamma^{\rm I}$ is the contribution to the observed shape resulting from IAs, and $\varepsilon_{\rm src}$ is the source ellipticity that the galaxy would have in the absence of the process causing the IA.

Now the theoretical two-point statistic consists of three types of terms: $\langle\gamma\gamma\rangle$, $\langle\gamma^{\rm I}\gamma\rangle$, and $\langle\gamma^{\rm I}\gamma^{\rm I}\rangle$. The first of these terms leads to the standard lensing power spectra of Equation (1.87), while the other two terms lead to additional

contributions to the observed power spectra, $C^{\epsilon\epsilon}_{\ell;ij}$, so that:

$$C^{\epsilon\epsilon}_{\ell;ij} = C^{\gamma\gamma}_{\ell;ij} + C^{\mathrm{I}\gamma}_{\ell;ij} + C^{\gamma\mathrm{I}}_{\ell;ij} + C^{\mathrm{II}}_{\ell;ij} + N^{\epsilon}_{\ell;ij}, \tag{1.91}$$

where the $C^{\mathrm{I}\gamma}_{\ell;ij}$ spectra represent the correlation between the background shear and the foreground IA, the $C^{\gamma\mathrm{I}}_{\ell;ij}$ spectra correspond to the opposite case, $C^{\mathrm{II}}_{\ell;ij}$ are the auto-correlation spectra of the IAs, and $N^{\epsilon}_{\ell;ij}$ is a shot noise term.

The additional spectra can be described in a similar manner to the shear power spectra, by way of the 'non-linear alignment' (NLA) model (Bridle & King 2007). In this model, the IA contribution to the ellipticity can be written:

$$\gamma^{\mathrm{I}}_1 = -\frac{\mathcal{A}_{\mathrm{IA}}\mathcal{C}_{\mathrm{IA}}}{4\pi G}(\partial_1^2 - \partial_2^2)\Phi_{\mathrm{p}}, \tag{1.92}$$

$$\gamma^{\mathrm{I}}_2 = -\frac{\mathcal{A}_{\mathrm{IA}}\mathcal{C}_{\mathrm{IA}}}{4\pi G}(2\partial_1\partial_2)\Phi_{\mathrm{p}}, \tag{1.93}$$

where $\gamma^{\mathrm{I}} = \gamma^{\mathrm{I}}_1 + \mathrm{i}\gamma^{\mathrm{I}}_2$, $\mathcal{A}_{\mathrm{IA}}$ and $\mathcal{C}_{\mathrm{IA}}$ are free model parameters to be determined by fitting to data or simulations, the partial derivatives are with respect to position on the sky $\boldsymbol{\theta}$ and Φ_{p} is the gravitational potential at the time of galaxy formation.

Now, by carrying out a process analogous to the derivation of the shear auto and cross-correlation spectra, the two contributions to the observed shear spectrum that are the result of IAs can be obtained:

$$C^{\mathrm{I}\gamma}_{\ell;ij} = \int_0^{\chi_{\mathrm{lim}}} \frac{\mathrm{d}\chi}{S_K^2(\chi)}[W_i(\chi)n_j(\chi) + n_i(\chi)W_j(\chi)]P_{\delta\mathrm{I}}(k,\chi), \tag{1.94}$$

$$C^{\mathrm{II}}_{\ell;ij} = \int_0^{\chi_{\mathrm{lim}}} \frac{\mathrm{d}\chi}{S_K^2(\chi)} n_i(\chi)\, n_j(\chi)\, P_{\mathrm{II}}(k,\chi), \tag{1.95}$$

where the intrinsic alignment power spectra, $P_{\delta\mathrm{I}}(k,\chi)$ and $P_{\mathrm{II}}(k,\chi)$, are ex-

pressed as functions of the matter power spectra:

$$P_{\delta \mathrm{I}}(k,\chi) = \frac{-\mathcal{A}_{\mathrm{IA}}\mathcal{C}_{\mathrm{IA}}\Omega_{\mathrm{m}}}{D(\chi)} P_{\delta\delta}(k,\chi), \tag{1.96}$$

$$P_{\mathrm{II}}(k,\chi) = \left(\frac{-\mathcal{A}_{\mathrm{IA}}\mathcal{C}_{\mathrm{IA}}\Omega_{\mathrm{m}}}{D(\chi)}\right)^2 P_{\delta\delta}(k,\chi), \tag{1.97}$$

in which $D(\chi)$ is the growth factor of density perturbations in the Universe, as a function of comoving distance.

1.2.9 The State of Weak Lensing

Cosmic shear experiments are currently well into a phase known as Stage III (Albrecht et al. 2006). They are able to carry out precision cosmology competitive with other cosmological probes such as supernovae, and the cosmic microwave background (CMB). However, there is a complication. Measurements of the comological parameters Ω_{m}, which is the dimensionless mass density of the Universe, and σ_8, the RMS value of density fluctuations on 8 h^{-1}Mpc scales, from the CMB (Planck Collaboration et al. 2020) are potentially in tension with those from cosmic shear surveys (Hildebrandt et al. 2020). At the current level of precision, one of the Stage III experiments, the Kilo-Degree Survey (KiDS), is inconsistent with the CMB measurements of Planck Collaboration et al. (2020). In addition, while other Stage III weak lensing experiments are consistent with CMB analysis, the Planck Collaboration et al. (2020) constraints of Ω_{m} and σ_8 are systematically higher. This discrepancy is shown in Figure 1.5. Stage III cosmic shear experiments also do not currently have the constraining power on the Hubble constant that is needed in order to address the Hubble tension.

We are now on the verge of Stage IV cosmic shear, with experiments like *Euclid* (Laureijs et al. 2011), *Roman* (Akeson et al. 2019), and the Rubin Observatory (LSST Science Collaboration et al. 2009) on the horizon. These experiments will offer more than an order of magnitude leap in precision, that

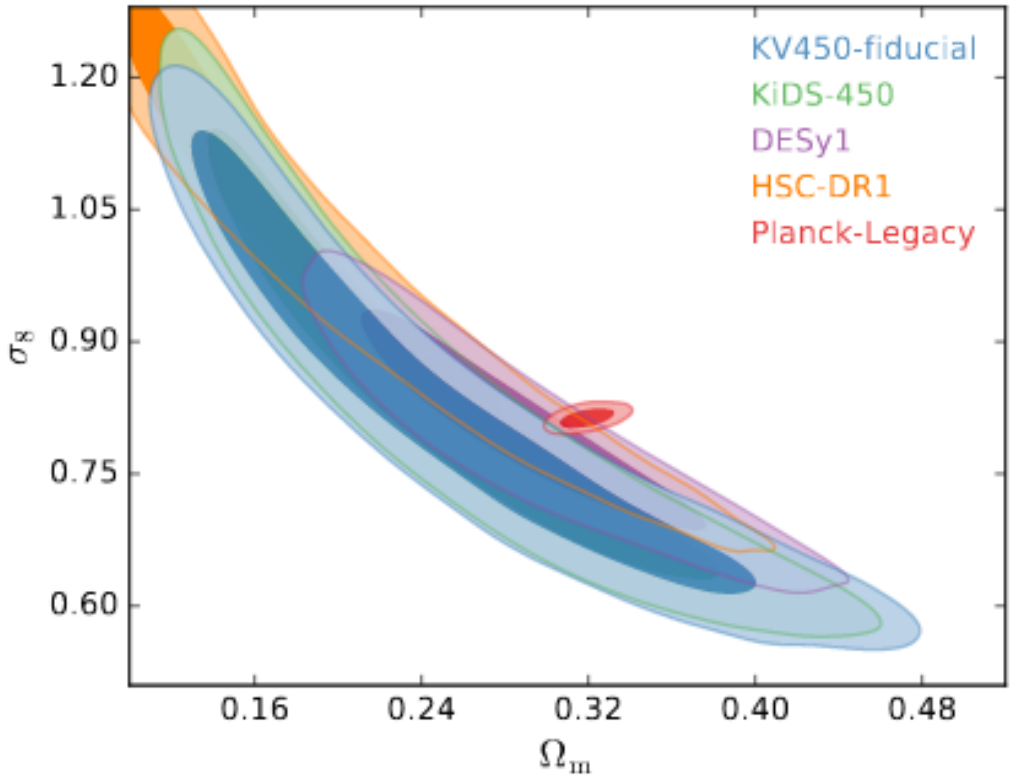

Figure 1.5: Comparison of the marginalised $1-\sigma$ and $2-\sigma$ contours on the cosmological parameters Ω_m and σ_8 between Stage III cosmic shear experiments and the CMB. The CMB experiment is *Planck* (Planck Collaboration et al. 2020), whereas the weak lensing experiments are KiDS-450 (de Jong et al. 2013), the Dark Energy Survey (DES)(Dark Energy Survey Collaboration 2005), and HyperSuprime-Cam (HSC) (Hikage et al. 2019). Adapted from Hildebrandt et al. (2020).

will enable us to begin to address discrepancies like the Hubble tension and the $\Omega_m - \sigma_8$ tension. They will also be effective probes of dark energy (Albrecht et al. 2006).

But, in order to use this newfound precision effectively, we must also ensure that the accuracy of our methods keeps up. Hitherto ignored systematic effects must be understood well, and assumptions in the theoretical framework must be relaxed. The focus of this thesis is the forecasting of the impact of such effects on Stage IV experiments, and the mitigation of such biases and errors that would compromise their accuracy.

1.3 Forecasting for Stage IV Surveys

This section adapts Sections 2.7 and 3 of Deshpande et al. (2020a).

Typically, once data is obtained from a given survey, Bayesian inference techniques are used to fit theoretical models to it and obtain constraints on cosmological parameters. The preferred tools for this are Markov–Chain Monte Carlo techniques, and variants thereof. For detailed overviews of these methods, see Verde (2007, 2010).

However, in advance of obtaining data, it is often necessary to forecast the constraining ability of experiments. This can be accomplished through employing the Fisher matrix formalism (Tegmark et al. 1997). Given a model for the likelihood and covariance of the survey, this allows the prediction of uncertainty constraints on parameters of interest.

In this section, I will review the mathematical formalism behind the use of Fisher matrices for forecasting parameter constraints. I will also show how this formalism can be extended to predict biases from neglecting systematic effects. Additionally, modelling specifics that are used throughout this work to represent Stage IV experiments will be detailed. In particular, the specifications of *Euclid* will be used, as these are readily available and well-established (Euclid Collaboration: Blanchard et al. 2020). Furthermore, I will present the choice of fiducial cosmology used throughout.

1.3.1 Fisher Matrices

The Fisher matrix, F, is explicitly defined as the Hessian of the log-likelihood:

$$F_{\alpha\beta} = \left\langle \frac{-\partial^2 \ln L}{\partial\theta_\alpha \partial\theta_\beta} \right\rangle, \tag{1.98}$$

where α and β index the matrix such that the corresponding entry relates to parameters of interest θ_α and θ_β respectively, and L is the likelihood.

For Stage IV cosmic shear experiments, the likelihood can be safely assumed to be Gaussian (Lin et al. 2020; Taylor et al. 2019); though I note that in reality it is non-Gaussian (see e.g. Sellentin et al. 2018). Generically, the Fisher matrix for a Gaussian likelihood can be written in terms of the covariance of the data, $\boldsymbol{C}$, and the mean of the data vector, $\boldsymbol{\mu}$. It takes the form:

$$F_{\alpha\beta} = \frac{1}{2}\,\mathrm{tr}\left[\frac{\partial \boldsymbol{C}}{\partial\theta_\alpha}\boldsymbol{C}^{-1}\frac{\partial \boldsymbol{C}}{\partial\theta_\beta}\boldsymbol{C}^{-1}\right] + \sum_{pq}\frac{\partial\mu_p}{\partial\theta_\alpha}(\boldsymbol{C}^{-1})_{pq}\frac{\partial\mu_q}{\partial\theta_\beta}, \tag{1.99}$$

with the summations over p and q representing sums over the variables of the data vector. Now, considering the case of cosmic shear specifically, the actual signal is the mean of the angular power spectrum. Accordingly the first term in the above vanishes. This means that the corresponding Fisher matrix is expressed as:

$$F_{\alpha\beta} = \sum_{\ell'=\ell_{\min}}^{\ell_{\max}}\sum_{\ell=\ell_{\min}}^{\ell_{\max}}\sum_{ij,mn}\frac{\partial C^{\epsilon\epsilon}_{\ell;ij}}{\partial\theta_\alpha}\mathrm{Cov}^{-1}\left[C^{\epsilon\epsilon}_{\ell;ij}, C^{\epsilon\epsilon}_{\ell';mn}\right]\frac{\partial C^{\epsilon\epsilon}_{\ell';mn}}{\partial\theta_\beta}, \tag{1.100}$$

where $\mathrm{Cov}^{-1}\left[C^{\epsilon\epsilon}_{\ell;ij}, C^{\epsilon\epsilon}_{\ell';mn}\right]$ is the covariance of the signal, $\{\ell_{\min}, \ell_{\max}\}$ bound the angular wavenumber range of the survey, and the sums are over the ℓ-blocks.

The uncertainties can then be predicted for parameters of interest by examining the diagonal of the inverse of the matrix. For parameter θ_α, the predicted 1σ uncertainty, σ_α is given by:

$$\sigma_\alpha = \sqrt{{F_{\alpha\alpha}}^{-1}}. \tag{1.101}$$

Another aspect of this formalism that makes it particularly useful in this work,

is that it can readily be extended to predict any biases in the parameters of interest that would result from neglecting systematic effects during inference (Taylor et al. 2007). Modelling a particular systematic effect as an additive term to the shear angular power spectra, $\delta C_{\ell;ij}$, the predicted bias, $\mathfrak{b}_\alpha$, on parameter of interest θ_α depends on the Fisher matrix thusly:

$$\mathfrak{b}_\alpha = \sum_\beta \left(F^{-1}\right)_{\alpha\beta} \mathcal{B}_\beta, \tag{1.102}$$

with:

$$\mathcal{B}_\beta = \sum_{\ell'=\ell_{\rm min}}^{\ell_{\rm max}} \sum_{\ell=\ell_{\rm min}}^{\ell_{\rm max}} \sum_{ij,mn} \delta C_{\ell;ij}\, {\rm Cov}^{-1}\left[C^{\epsilon\epsilon}_{\ell;ij}, C^{\epsilon\epsilon}_{\ell';mn}\right] \frac{\partial C_{\ell';mn}}{\partial \theta_\beta}. \tag{1.103}$$

This formalism is used throughout this thesis to quantify the biases on inferred cosmological parameters, if various systematic effects are neglected at the shear angular power spectrum level.

1.3.2 Modelling a *Euclid*-like Survey

In order to quantify the impact of the studied effects on a *Euclid*-like survey, I adopted the forecasting specifications of Euclid Collaboration: Blanchard et al. (2020). Accordingly, I took there to be ten equi-populated tomographic bins, with bin edges: {0.001, 0.418, 0.560, 0.678, 0.789, 0.900, 1.019, 1.155, 1.324, 1.576, 2.50}.

I primarily investigated the impact on the 'optimistic' case for such a survey, in which ℓ-modes of up to 5000 are probed, because this is necessary for *Euclid* to reach its required figure of merit using cosmic shear (Euclid Collaboration: Blanchard et al. 2020). I considered the intrinsic variance of observed ellipticities to have two components, each with a value of 0.21, so that the intrinsic ellipticity root-mean-square value $\sigma_\epsilon = \sqrt{2} \times 0.21 \approx 0.3$. For *Euclid*, I took the surface density of galaxies to be $\bar{n}_{\rm g} = 30$ arcmin^{-2}, and the fraction

Table 1.1: Choice of parameter values used to define the probability distribution function of the photometric redshift distribution of sources, in Equation (1.106). I did not consider how variation in the quality of photometric redshifts impacts the Fisher matrix predictions. Adapted from Deshpande et al. (2020a). Reproduced with permission from Astronomy & Astrophysics, © ESO.

Model Parameter	Fiducial Value
c_b	1.0
z_b	0.0
σ_b	0.05
c_o	1.0
z_o	0.1
σ_o	0.05
f_out	0.1

of sky covered to be $f_\mathrm{sky} = 0.36$.

As in Euclid Collaboration: Blanchard et al. (2020), I defined the distributions of galaxies in the tomographic bins, for photometric redshift estimates, as:

$$\mathcal{N}_i(z) = \frac{\int_{z_i^-}^{z_i^+} \mathrm{d}z_\mathrm{p}\, \mathfrak{n}(z) p_\mathrm{ph}(z_\mathrm{p}|z)}{\int_{z_\mathrm{min}}^{z_\mathrm{max}} \mathrm{d}z \int_{z_i^-}^{z_i^+} \mathrm{d}z_\mathrm{p}\, \mathfrak{n}(z) p_\mathrm{ph}(z_\mathrm{p}|z)}, \tag{1.104}$$

where z_p is measured photometric redshift, z_i^- and z_i^+ are edges of the i-th redshift bin, and z_min and z_max define the range of redshifts covered by the survey. Then, $n_i(\chi) = \mathcal{N}_i(z)\mathrm{d}z/\mathrm{d}\chi$.

In Equation (1.104), $\mathfrak{n}(z)$ is the true distribution of galaxies with redshift, z; defined as in the *Euclid* Red Book (Laureijs et al. 2011):

$$\mathfrak{n}(z) \propto \left(\frac{z}{z_0}\right)^2 \exp\left[-\left(\frac{z}{z_0}\right)^{3/2}\right], \tag{1.105}$$

where $z_0 = z_\mathrm{m}/\sqrt{2}$, with $z_\mathrm{m} = 0.9$ as the median redshift of the survey. Meanwhile, the function $p_\mathrm{ph}(z_\mathrm{p}|z)$ describes the probability that a galaxy at redshift

z is measured to have a redshift $z_{\rm p}$:

$$p_{\rm ph}(z_{\rm p}|z) = \frac{1-f_{\rm out}}{\sqrt{2\pi}\sigma_{\rm b}(1+z)}\exp\left\{-\frac{1}{2}\left[\frac{z-c_{\rm b}z_{\rm p}-z_{\rm b}}{\sigma_{\rm b}(1+z)}\right]^2\right\} + \frac{f_{\rm out}}{\sqrt{2\pi}\sigma_{\rm o}(1+z)}\exp\left\{-\frac{1}{2}\left[\frac{z-c_{\rm o}z_{\rm p}-z_{\rm o}}{\sigma_{\rm o}(1+z)}\right]^2\right\}. \quad (1.106)$$

In this parameterisation, the first term describes the multiplicative and additive bias in redshift determination for the fraction of sources with a well measured redshift, whereas the second term accounts for the effect of a fraction of catastrophic outliers, $f_{\rm out}$. The values of these parameters, chosen to match the selection of Euclid Collaboration: Blanchard et al. (2020), are stated in Table 1.1. By using this formalism, the impact of the photometric redshift uncertainties was also included in the derivatives of the shear power spectra.

1.3.3 Choice of Fiducial Cosmology

I considered the w_0w_aCDM model case in my calculations. This extension of the lambda cold dark matter (ΛCDM) model accounts for a time-varying dark energy equation of state. This model consists of the following parameters:

- $\Omega_{\rm m}$ - the present-day matter density parameter,
- $\Omega_{\rm b}$ - the present-day baryonic matter density parameter,
- $h = H_0/100{\rm km\,s^{-1}Mpc^{-1}}$ - the Hubble parameter,
- $n_{\rm s}$ - the spectral index,
- σ_8 - the RMS value of density fluctuations on $8h^{-1}$Mpc scales,
- $\Omega_{\rm DE}$ - the present-day dark energy density parameter,
- w_0 - the present-day value of the dark energy equation of state,
- w_a - the high redshift value of the dark energy equation of state.

Table 1.2: Fiducial values of w_0w_aCDM cosmological parameters used throughout this thesis. These values were selected in accordance with *Euclid* Collaboration forecasting choices (Euclid Collaboration: Blanchard et al. 2020); to facilitate consistent comparisons. Note that the value of the neutrino mass was kept fixed in the Fisher matrix calculations. Adapted from Deshpande et al. (2020a). Reproduced with permission from Astronomy & Astrophysics, © ESO.

Cosmological Parameter	Fiducial Value
$\Omega_{\rm m}$	0.32
$\Omega_{\rm b}$	0.05
h	0.67
$n_{\rm s}$	0.96
σ_8	0.816
$\sum m_\nu$ (eV)	0.06
$\Omega_{\rm DE}$	0.68
w_0	-1
w_a	0

Additionally, I assumed neutrinos to have masses. I denote the sum of neutrino masses by $\sum m_\nu \neq 0$. This quantity was kept fixed, and I did not generate confidence contours for it, in concordance with Euclid Collaboration: Blanchard et al. (2020). The fiducial values chosen for these parameters are given in Table 1.2. These values were chosen to allow for a direct and consistent comparison of the studied corrections with the forecast precision of *Euclid*. They are also our current best estimates of these parameters (Planck Collaboration et al. 2020). The values provided in the forecasting specifications for the free parameters of the NLA model were also used in this work, in Equation (1.96) and Equation (1.97). These are: $\mathcal{A}_{\rm IA} = 1.72$ and $\mathcal{C}_{\rm IA} = 0.0134$.

My Fisher matrices included the parameters $\Omega_{\rm m}, \Omega_{\rm b}, h, n_{\rm s}, \sigma_8, \Omega_{\rm DE}, w_0, w_a$, and $\mathcal{A}_{\rm IA}$. I did not include any additional nuisance parameters. However, I do not expect this to affect the significance of any studied corrections, as Euclid Collaboration: Blanchard et al. (2020) find that the inclusion of various nuisance parameters typically alters the predicted relative uncertainties on cosmological parameters by less than 10%.

1.4 Utilisation of Foundational Theory

The weak lensing formalism and forecasting specifications discussed in this chapter are used throughout this thesis. Here, I describe how these concepts are utilised and built upon. The research chapters that follow aim to refine the theoretical calculation of the cosmic shear observable, as detailed in Section 1.2, to match the increased precision of upcoming experiments.

Specifically, Chapter 2 relaxes the reduced shear approximation, described in Section 1.2.4 and accounts for the effects of the magnification effect identified in Section 1.2.3. Following on from this, Chapter 3 discusses the implications of the Limber approximation, mentioned in Section 1.2.6, on the reduced shear and magnification bias corrections. Similarly, Chapter 4, extends the cosmic shear observable to account for the effects of the peculiar velocities of galaxies. Finally, a strategy to mitigate the effects of the discussed corrections is presented in Chapter 5; involving re-weighting the projection kernels described in Section 1.2.6. To accurately forecast the impact of these terms, all of the research chapters use the survey specifications and Fisher matrices given in Section 1.3.

Chapter 2

Reduced Shear Approximation & Magnification Bias

This chapter adapts Deshpande et al. (2020a).

In this chapter, I evaluate the impact of the reduced shear approximation and magnification bias on the information that will be obtained from the angular power spectrum observed by a Stage IV cosmic shear survey. Specifically, I focus on the impact on inference from the *Euclid* space telescope.

2.1 Motivation and Outline

The constituent parts of the ΛCDM model, and its extensions, are not all fully understood. In the current framework, there is no definitive explanation for the physical natures of dark matter and dark energy. Cosmic shear is a powerful cosmological probe that can help improve our knowledge of these.

With the impending arrival of Stage IV dark energy experiments, such as *Euclid*, *Roman*, and the Rubin Observatory, we are poised for a leap in precision. To ensure that the accuracy of the analysis keeps up with the increasing precision of the measurements, the impact of previously neglected physical effects must be evaluated, and assumptions in the theoretical formalism must also be relaxed.

One such, currently ubiquitous, assumption is the reduced shear approximation. Demonstrated in Equation (1.75) and Equation (1.76), this approximation takes the statistics of the reduced shear, the quantity that is actually observed, to be equal to those of the shear. The formalism to correct for the effect of measuring reduced shear, rather than shear itself, is known (Shapiro 2009; Krause & Hirata 2010). However, its impact on impending surveys has not yet been quantified.

Another effect that is not typically taken into consideration for probes of cosmic shear is magnification bias. This refers to a change in the observed galaxy distribution for a particular survey due to the magnification (or demagnification) of individual sources close to the survey's flux limit. While simple models have been proposed to quantify the impact on Stage IV experiments (specifically for observations from the Rubin Observatory; Liu et al. 2014), this approach risks underestimating the bias for surveys covering the redshift range of *Euclid*'s cosmic shear probe.

Specifically, rather than assuming that the magnification bias at the survey's mean redshift is representative of the bias at all covered redshifts, a tomographic approach is required. Magnification bias also affects measurements of galaxy clustering; which is the other of *Euclid*'s major probes. Thiele et al. (2020); Lorenz et al. (2018); Duncan et al. (2014) study the impact of magnification on the clustering sample, and as such complement this work in forming a holistic picture of the effect on *Euclid*.

Conveniently, the magnification bias correction takes a mathematically similar form to that of reduced shear; meaning these corrections can be treated together (Schmidt et al. 2009). Accordingly, I consider them both within this chapter. Here, I calculate the bias on the predicted cosmological parameters obtained from *Euclid*, when these two effects are neglected. I also show how the uncertainty constraints on the cosmological parameters would change if the

corrections were taken into account. I further extend the existing correction formalism to the calculation of IAs, which has not been considered to-date.

This chapter is organised as follows: I begin by detailing the formalism for relaxing the reduced shear approximation, as established in Shapiro (2009), in Section 2.2. Next, in Section 2.3, I describe magnification bias, and present the mathematical expression to correct for it. Then, Section 2.4 extends both the reduced shear and magnification bias corrections to the calculation of IAs. Following on, Section 2.5 describes the modelling specifics used to quantify the impact on *Euclid* of these effects, while Section 2.6 presents my results. Finally, a summary of the work reported in this chapter is given in Section 2.7, alongside future prospects.

2.2 The Reduced Shear Correction

I account for the effects of the reduced shear approximation by means of a second-order correction to Equation (1.86) (Shapiro 2009; Krause & Hirata 2010; Dodelson et al. 2006). This can be done by taking the Taylor expansion of Equation (1.71) around $\kappa = 0$, and keeping terms up to second-order:

$$g^{\alpha}(\boldsymbol{\theta}) = \gamma^{\alpha}(\boldsymbol{\theta}) + (\gamma^{\alpha}\kappa)(\boldsymbol{\theta}) + \mathcal{O}(\kappa^3). \tag{2.1}$$

By substituting this expanded form of g^{α} for γ^{α} in Equation (1.83) and then recomputing the E-mode ensemble average for each tomographic combination, I obtain the tomographic version of the original result of Equation (1.85), plus a correction:

$$\begin{aligned}\delta\left\langle\widetilde{E}_i(\boldsymbol{\ell})\widetilde{E}_j(\boldsymbol{\ell'})\right\rangle &= (2\pi)^2\,\delta_{\mathrm{D}}^2(\boldsymbol{\ell}+\boldsymbol{\ell'})\,\delta C_{\ell;ij}^{\mathrm{RS}} \\ &= \sum_{\alpha}\sum_{\beta} T^{\alpha}(\boldsymbol{\ell})T^{\beta}(\boldsymbol{\ell'})\left\langle\widetilde{(\gamma^{\alpha}\kappa)}_i(\boldsymbol{\ell})\,\widetilde{\gamma}_j^{\beta}(\boldsymbol{\ell'})\right\rangle \\ &\quad + T^{\alpha}(\boldsymbol{\ell'})T^{\beta}(\boldsymbol{\ell})\left\langle\widetilde{(\gamma^{\alpha}\kappa)}_j(\boldsymbol{\ell'})\,\widetilde{\gamma}_i^{\beta}(\boldsymbol{\ell})\right\rangle, \end{aligned}\tag{2.2}$$

where $\delta C_{\ell;ij}^{\mathrm{RS}}$ are the resulting corrections to the angular spectra. Applying the Limber approximation once more, I obtain an expression for these:

$$\delta C_{\ell;ij}^{\mathrm{RS}} = \ell(\ell+1)\frac{(\ell+2)!}{(\ell-2)!}\frac{1}{(\ell+1/2)^6}\int_0^\infty \frac{\mathrm{d}^2\boldsymbol{\ell'}}{(2\pi)^2}\cos(2\phi_{\ell'}-2\phi_\ell) \times B_{ij}^{\kappa\kappa\kappa}(\boldsymbol{\ell},\boldsymbol{\ell'},-\boldsymbol{\ell}-\boldsymbol{\ell'}). \tag{2.3}$$

The factors of $\ell(\ell+1)(\ell+2)!/(\ell-2)!$ and $1/(\ell+1/2)^6$ arise from foregoing the three-point equivalent of the pre-factor unity approximation (Kitching et al. 2017). As in the two-point case, the product of these factors can be well approximated by one. However, I do not make this approximation for the sake of completeness, and as the additional factors do not add any significant computational expense. Here, $B_{ij}^{\kappa\kappa\kappa}$ is the two-redshift convergence bispectrum, which takes the following form:

$$\begin{aligned} B_{ij}^{\kappa\kappa\kappa}(\boldsymbol{\ell_1},\boldsymbol{\ell_2},\boldsymbol{\ell_3}) &= B_{iij}^{\kappa\kappa\kappa}(\boldsymbol{\ell_1},\boldsymbol{\ell_2},\boldsymbol{\ell_3}) + B_{ijj}^{\kappa\kappa\kappa}(\boldsymbol{\ell_1},\boldsymbol{\ell_2},\boldsymbol{\ell_3}) \\ &= \int_0^{\chi_{\mathrm{lim}}} \frac{\mathrm{d}\chi}{S_K^4(\chi)} W_i(\chi)W_j(\chi)[W_i(\chi)+W_j(\chi)] \\ &\quad \times B_{\delta\delta\delta}(\boldsymbol{k_1},\boldsymbol{k_2},\boldsymbol{k_3},\chi), \end{aligned} \tag{2.4}$$

where $B_{iij}^{\kappa\kappa\kappa}$ and $B_{ijj}^{\kappa\kappa\kappa}$ are the three-redshift bispectra, k_x is the magnitude and $\phi_{\ell;x}$ is the angular component of $\boldsymbol{k_x}$ (for $x \in \{1,2,3\}$). Under the Limber approximation, $k_x = (\ell_x+1/2)/S_K(\chi)$. Here, I also approximate the photometric redshift bins to be infinitesimally narrow. In reality, because these bins would have a finite width, the product of lensing kernels in Equation (2.4) would be replaced by a single integral over the products of the contents of the integral in Equation (1.88). Accordingly, the values of the bispectrum would be slightly higher. However, given that *Euclid* will have high quality photometric redshift measurement, I expect this difference to be negligible. Consequently, in my calculations I proceeded with the narrow-bin approximation here.

Analogous to the convergence angular power spectra being projections of the three-dimensional matter power spectrum, the two-dimensional convergence bispectra are a projection of the three-dimensional matter bispectrum, $B_{\delta\delta\delta}(\boldsymbol{k_1}, \boldsymbol{k_2}, \boldsymbol{k_3}, \chi)$. The matter bispectrum is not well-described analytically. Instead, a semi-analytic approach starting with second-order perturbation theory (2PT) (Fry 1984), and then fitting its result to N-body simulations, is employed. At this initial stage, I used the fitting formula of Scoccimarro & Couchman (2001). Accordingly, the matter bispectrum can be written:

$$B_{\delta\delta\delta}(\boldsymbol{k_1}, \boldsymbol{k_2}, \boldsymbol{k_3}, \chi) = 2F_2^{\rm eff}\left(\boldsymbol{k_1}, \boldsymbol{k_2}\right) P_{\delta\delta}(k_1, \chi) P_{\delta\delta}(k_2, \chi) + \text{cyc.}, \tag{2.5}$$

where $F_2^{\rm eff}$ encapsulates the simulation fitting aspect, and is defined as:

$$\begin{aligned} F_2^{\rm eff}(\boldsymbol{k_1}, \boldsymbol{k_2}) = &\frac{5}{7}\, a(n_{\rm s}, k_1)\, a(n_{\rm s}, k_2) \\ &+ \frac{1}{2}\frac{\boldsymbol{k_1}\cdot\boldsymbol{k_2}}{k_1 k_2}\left(\frac{k_1}{k_2} + \frac{k_2}{k_1}\right) b(n_{\rm s}, k_1)\, b(n_{\rm s}, k_2) \\ &+ \frac{2}{7}\left(\frac{\boldsymbol{k_1}\cdot\boldsymbol{k_2}}{k_1 k_2}\right)^2 c(n_{\rm s}, k_1)\, c(n_{\rm s}, k_2), \end{aligned} \tag{2.6}$$

where $n_{\rm s}$ is the scalar spectral index, which indicates the deviation of the primordial matter power spectrum from scale invariance ($n_{\rm s} = 1$), and the functions a, b, and c are fitting functions, defined in Scoccimarro & Couchman (2001). There are no additional correction terms of form $\widetilde{E}\widetilde{B}$ or $\widetilde{B}\widetilde{B}$, and it has been shown that higher-order terms from the Taylor expansion of Equation (2.1) are sub-dominant (Dodelson et al. 2006; Krause & Hirata 2010; Deshpande et al. 2020a), so further terms in Equation (2.1) can be neglected for now.

2.3 The Magnification Bias Correction

The observed overdensity of galaxies on the sky is affected by gravitational lensing in two competing ways (Turner et al. 1984). Firstly, individual galaxies can

be magnified (or demagnified), which results in their flux being increased (or decreased). At the flux limit of a survey, this can cause fainter sources (which in the absence of lensing would be excluded) to be included in the observed sample. Conversely, the density of galaxies in the patch of sky around this source appears reduced (or increased) due to the patch of sky being magnified (or demagnified) similarly to the source. Accordingly, the net effect of these depends on the slope of the intrinsic, unlensed, galaxy luminosity function, at the survey's flux limit. This net effect is known as magnification bias.

Additionally, galaxies can also be pulled into a sample because their effective radius is increased as a consequence of magnification, such that they pass a resolution factor cut. In this work, I do not consider this effect as it is more important for ground-based surveys than space-based ones such as *Euclid*.

In the case of weak lensing, where $|\kappa| \ll 1$, and assuming that fluctuations in the intrinsic galaxy overdensity are small on the scales of interest, the observed galaxy overdensity in tomographic bin i is (Hui et al. 2007; Turner et al. 1984):

$$\delta^g_{\mathrm{obs};i}(\boldsymbol{\theta}) = \delta^g_i(\boldsymbol{\theta}) + (5s_i - 2)\kappa_i(\boldsymbol{\theta}), \tag{2.7}$$

where $\delta^g_i(\boldsymbol{\theta})$ is the intrinsic, unlensed, galaxy overdensity in bin i, and s_i is the slope of the cumulative galaxy number counts brighter than the survey's limiting magnitude, m_{lim}, in redshift bin i. This slope is defined as:

$$s_i = \left.\frac{\partial \log_{10} \mathfrak{n}(\bar{z}_i, m)}{\partial m}\right|_{m_{\mathrm{lim}}}, \tag{2.8}$$

where $\mathfrak{n}(\bar{z}_i, m)$ is the true distribution of galaxies, evaluated at the central redshift of bin i, $\bar{z}_i$. It is important to note that, in practice, this slope is determined from observations, and accordingly depends on the wavelength band within which the galaxy is observed in addition to its redshift. Operationally, magnification bias causes the true shear, γ^α_i, to be replaced, within the es-

timator used to determine the power spectrum from data, by an 'observed' shear:

$$\gamma^{\alpha}_{\mathrm{obs};i} \to \gamma^{\alpha}_{i} + \gamma^{\alpha}_{i}\delta^{g}_{\mathrm{obs};i} = \gamma^{\alpha}_{i} + \gamma^{\alpha}_{i}\delta^{g}_{i} + (5s_i - 2)\gamma^{\alpha}_{i}\kappa_i. \tag{2.9}$$

Now, one can evaluate the impact of magnification bias on the two-point statistic by substituting $\widetilde{\gamma}^{\alpha}_{\mathrm{obs};i}$ for $\widetilde{\gamma}^{\alpha}_{i}$ in Equation (1.83), and recomputing. As source-lens clustering terms of the form $\gamma^{\alpha}_{i}\delta^{g}_{i}$ are negligible (Schmidt et al. 2009), one recovers the standard result of Equation (1.85), with an additional correction term:

$$\begin{aligned}\delta\langle\widetilde{E}_i(\boldsymbol{\ell})\widetilde{E}_j(\boldsymbol{\ell'})\rangle = \sum_{\alpha}\sum_{\beta} & T^{\alpha}(\boldsymbol{\ell})T^{\beta}(\boldsymbol{\ell'})(5s_i - 2)\,\langle\widetilde{(\gamma^{\alpha}\kappa)}_{i}(\boldsymbol{\ell})\,\widetilde{\gamma}^{\beta}_{j}(\boldsymbol{\ell'})\rangle \\ & + T^{\alpha}(\boldsymbol{\ell'})T^{\beta}(\boldsymbol{\ell})(5s_j - 2)\,\langle\widetilde{(\gamma^{\alpha}\kappa)}_{j}(\boldsymbol{\ell'})\,\widetilde{\gamma}^{\beta}_{i}(\boldsymbol{\ell})\rangle\,.\end{aligned} \tag{2.10}$$

Analogously to the reduced shear case, one then obtains corrections to the auto and cross-correlation angular spectra of the form:

$$\begin{aligned}\delta C^{\mathrm{MB}}_{\ell;ij} = \ell(\ell+1)\frac{(\ell+2)!}{(\ell-2)!}\frac{1}{(\ell+1/2)^6}\int_0^{\infty}\frac{\mathrm{d}^2\boldsymbol{\ell'}}{(2\pi)^2}\cos(2\phi_{\ell'} - 2\phi_{\ell}) \\ \times\,[(5s_i - 2)B^{\kappa\kappa\kappa}_{iij}(\boldsymbol{\ell},\boldsymbol{\ell'},-\boldsymbol{\ell}-\boldsymbol{\ell'}) \\ + (5s_j - 2)B^{\kappa\kappa\kappa}_{ijj}(\boldsymbol{\ell},\boldsymbol{\ell'},-\boldsymbol{\ell}-\boldsymbol{\ell'})].\end{aligned} \tag{2.11}$$

I note that the mathematical form of Equation (2.11) is simply Equation (2.3) with factors of $(5s_i - 2)$ and $(5s_j - 2)$ applied to the corresponding bispectra. These additional pre-factors are due to the magnification bias contribution from each bin depending on the slope of the luminosity function in that bin. Accordingly, both effects can be computed for the cost of one.

2.4 IA-enhanced Lensing Bias

The reduced shear approximation is typically also employed when computing the contribution of IAs to the lensing signal, and the role magnification bias

plays here is usually neglected too. I account for these by substituting the appropriate second-order expansions of the shear, Equation (2.1) and Equation (2.9), in place of γ within Equation (1.90). Neglecting source-lens clustering, the ellipticity now becomes:

$$\varepsilon_{\rm obs} \simeq \gamma + (1 + 5s - 2)\gamma\kappa + \gamma^{\rm I} + \varepsilon_{\rm src}. \tag{2.12}$$

Constructing a theoretical expression for the two-point statistic from this revised expression for the ellipticity now gives six types of terms: $\langle\gamma\gamma\rangle$, $\langle\gamma^{\rm I}\gamma\rangle$, $\langle\gamma^{\rm I}\gamma^{\rm I}\rangle$, $\langle(\gamma\kappa)\gamma\rangle$, $\langle(\gamma\kappa)(\gamma\kappa)\rangle$, and $\langle(\gamma\kappa)\gamma^{\rm I}\rangle$. The first three terms remain unchanged from the first-order case. The fourth term encompasses the basic reduced shear and magnification bias corrections, and results in the shear power spectrum corrections defined by Equation (2.3) and Equation (2.11). The fifth of these terms can be neglected, as it is a fourth-order term. The final term creates an additional correction, $\delta C^{\rm I}_{\ell;ij}$, to the observed spectra that takes a form analogous to the basic reduced shear and magnification bias corrections:

$$\begin{aligned}\delta C^{\rm I}_{\ell;ij} = \ell(\ell+1)\frac{(\ell+2)!}{(\ell-2)!}\frac{1}{(\ell+1/2)^6}\int_0^\infty \frac{{\rm d}^2\boldsymbol{\ell'}}{(2\pi)^2}\cos(2\phi_{\ell'}) \\ \times [(1+5s_i-2)B^{\kappa\kappa{\rm I}}_{iij}(\boldsymbol{\ell},\boldsymbol{\ell'},-\boldsymbol{\ell}-\boldsymbol{\ell'}) \\ + (1+5s_j-2)B^{\kappa\kappa{\rm I}}_{jji}(\boldsymbol{\ell},\boldsymbol{\ell'},-\boldsymbol{\ell}-\boldsymbol{\ell'})],\end{aligned} \tag{2.13}$$

where the convergence-IA bispectra, $B^{\kappa\kappa{\rm I}}_{iij}$ and $B^{\kappa\kappa{\rm I}}_{jji}$, are given by:

$$B^{\kappa\kappa{\rm I}}_{iij}(\boldsymbol{\ell_1},\boldsymbol{\ell_2},\boldsymbol{\ell_3}) = \int_0^{\chi_{\rm lim}} \frac{{\rm d}\chi}{S^4_K(\chi)} W_i^2(\chi) n_j(\chi) B_{\delta\delta{\rm I}}(\boldsymbol{k_1},\boldsymbol{k_2},\boldsymbol{k_3},\chi), \tag{2.14}$$

$$B^{\kappa\kappa{\rm I}}_{jji}(\boldsymbol{\ell_1},\boldsymbol{\ell_2},\boldsymbol{\ell_3}) = \int_0^{\chi_{\rm lim}} \frac{{\rm d}\chi}{S^4_K(\chi)} W_j^2(\chi) n_i(\chi) B_{\delta\delta{\rm I}}(\boldsymbol{k_1},\boldsymbol{k_2},\boldsymbol{k_3},\chi). \tag{2.15}$$

The density perturbation-IA bispectrum, $B_{\delta\delta{\rm I}}(\boldsymbol{k_1},\boldsymbol{k_2},\boldsymbol{k_3},\chi)$, can be calculated in a similar way to the matter density perturbation bispectrum, using per-

turbation theory and the Scoccimarro & Couchman (2001) fitting formula. Accordingly:

$$\begin{aligned} B_{\delta\delta\mathrm{I}}(\boldsymbol{k_1}, \boldsymbol{k_2}, \boldsymbol{k_3}, \chi) = 2F_2^{\mathrm{eff}}(\boldsymbol{k_1}, \boldsymbol{k_2}) P_{\mathrm{I}\delta}(k_1, \chi) P_{\delta\delta}(k_2, \chi) \\ + 2F_2^{\mathrm{eff}}(\boldsymbol{k_2}, \boldsymbol{k_3}) P_{\delta\delta}(k_2, \chi) P_{\delta\mathrm{I}}(k_3, \chi) \\ + 2F_2^{\mathrm{eff}}(\boldsymbol{k_1}, \boldsymbol{k_3}) P_{\delta\mathrm{I}}(k_1, \chi) P_{\delta\delta}(k_3, \chi), \end{aligned} \tag{2.16}$$

with $P_{\mathrm{I}\delta}(k_1, \chi) = P_{\delta\mathrm{I}}(k_1, \chi)$. This equation is an ansatz for how IAs behave in the non-linear regime, analogous to the NLA model. The described approach, and in particular the fitting functions, remain valid because, in the NLA model, one can treat IAs as a field proportional, by some redshift-dependent weighting, to the matter density contrast. Since the fitting functions, F_2^{eff}, do not depend on the comoving distance, they remain unchanged. For the full derivation of this bispectrum term, and a generalisation for similar terms, see Appendix B.

2.5 Modelling Methodology

The matter density power spectrum and growth factor used in my analysis were computed using the publicly available `CLASS`[1] cosmology package (Blas et al. 2011). Within the framework of `CLASS`, I included non-linear corrections to the matter density power spectrum, using the `Halofit` model (Takahashi et al. 2012), as well as the additional corrections of Mead et al. (2015).

In practice, the covariance of the data itself is non-Gaussian. Generally, when performing inference or calculating Fisher matrices for Stage IV cosmic shear, non-Gaussian contributions should be accounted for (see e.g. Barreira et al. 2018; Takada & Hu 2013). The dominant contribution to the non-Gaussian part of the covariance is the super-sample covariance (SSC) (Hu & Kravtsov 2003). This additional component arises from the fact that, in any

[1] `https://class-code.net/`

galaxy survey, a limited fraction of the Universe is observed. Density fluctuations with wavelengths larger than the size of the survey can then cause the background density measured by the survey to no longer be representative of the true average density of the Universe. Additional non-Gaussian contributions, such as connected trispectrum terms, can be safely neglected for *Euclid* (Barreira et al. 2018).

For weak lensing, the covariance can then be expressed as the sum of the Gaussian, $\mathrm{Cov_G}$, and SSC, $\mathrm{Cov_{SSC}}$, parts:

$$\begin{aligned}\mathrm{Cov}\left[C^{\epsilon\epsilon}_{\ell;ij}, C^{\epsilon\epsilon}_{\ell';mn}\right] &= \mathrm{Cov_G}\left[C^{\epsilon\epsilon}_{\ell;ij}, C^{\epsilon\epsilon}_{\ell';mn}\right] \\ &\quad + \mathrm{Cov_{SSC}}\left[C^{\epsilon\epsilon}_{\ell;ij}, C^{\epsilon\epsilon}_{\ell';mn}\right], \end{aligned} \tag{2.17}$$

where (i, j) and (m, n) are redshift bin pairs. The Gaussian covariance is given by:

$$\mathrm{Cov_G}\left[C^{\epsilon\epsilon}_{\ell;ij}, C^{\epsilon\epsilon}_{\ell';mn}\right] = \frac{C^{\epsilon\epsilon}_{\ell;im}\, C^{\epsilon\epsilon}_{\ell';jn} + C^{\epsilon\epsilon}_{\ell;in}\, C^{\epsilon\epsilon}_{\ell';jm}}{(2\ell+1) f_{\mathrm{sky}} \Delta\ell}\, \delta^{\mathrm{K}}_{\ell\ell'}, \tag{2.18}$$

where δ^{K} is the Kronecker delta, $\Delta\ell$ is the bandwidth of ℓ-modes sampled, and f_{sky} is the fraction of the sky surveyed.The contribution from SSC can be approximated as (Lacasa & Grain 2019):

$$\mathrm{Cov_{SSC}}\left[C^{\epsilon\epsilon}_{\ell;ij}, C^{\epsilon\epsilon}_{\ell';mn}\right] \approx R_\ell\, C^{\epsilon\epsilon}_{\ell;ij}\, R_{\ell'}\, C^{\epsilon\epsilon}_{\ell';mn}\, S_{ijmn}, \tag{2.19}$$

where S_{ijmn} is the dimensionless volume-averaged covariance of the background matter density contrast, and R_ℓ is the effective relative response of the observed power spectrum, which can safely be taken as a constant for a given probe.

Using these modelling specifics, together with those specified in Section 1.3, I first calculated the basic reduced shear correction of Equation (2.3), and then the resulting biases in the $w_0 w_a$CDM parameters using the Fisher

matrix formalism. To do so, I computed the derivatives of my tomographic matrices, at each sampled ℓ-mode, using the numerical method described in Euclid Collaboration: Blanchard et al. (2020). Additionally, to include the impact of SSC during this process, I calculated the dimensionless volume-averaged covariance of the background matter density contrast of Equation (2.19) using the publicly available `PySSC`[2] code (Lacasa & Grain 2019). With this, I computed the full-sky value, and divided by the *Euclid* value of $f_{\rm sky}$. Additionally, I set $R_\ell \approx 4$ for weak lensing[3].

Furthermore, to predict what the cosmological parameter uncertainties would look like in the scenario where the reduced shear correction has already been made, I added the relevant partial derivatives of the correction term, with respect to each cosmological parameter, to the relevant derivative of the angular power spectra within the Fisher matrix calculation.

The correction for magnification bias, the resulting biases in the cosmological parameters, and the change in cosmological parameter uncertainty if magnification bias was already accounted for, were then calculated in the same way as above. The slope of the luminosity function, as defined in Equation (2.8), was calculated for each redshift bin using the approach described in Appendix C of Joachimi & Bridle (2010). I applied a finite-difference method to the fitting formula for galaxy number density as a function of limiting magnitude stated here, in order to calculate the slope of the luminosity function at the limiting magnitude of *Euclid*, 24.5 (Laureijs et al. 2011); or AB in the *Euclid* VIS band (Cropper et al. 2012). This technique produces slope values consistent with those generated from the Schechter function approach of Liu et al. (2014). The calculated slopes for each redshift bin are given in Table 2.1. However, I emphasise that while this method allows the investigation of the

[2] `https://github.com/fabienlacasa/PySSC`
[3] Private communications with F. Lacasa.

Table 2.1: Slope of the luminosity function for each redshift bin, calculated at the central redshifts of each bin. These are evaluated at the limiting magnitude 24.5 (AB in the *Euclid* VIS band; Cropper et al. 2012). The slopes are determined using finite difference methods with the fitting formula of Joachimi & Bridle (2010), which is based on fitting to COMBO-17 and SDSS r-band results (Blake & Bridle 2005). Adapted from Deshpande et al. (2020a). Reproduced with permission from Astronomy & Astrophysics, © ESO.

Bin i	Central Redshift	Slope s_i
1	0.2095	0.196
2	0.489	0.274
3	0.619	0.320
4	0.7335	0.365
5	0.8445	0.412
6	0.9595	0.464
7	1.087	0.525
8	1.2395	0.603
9	1.45	0.720
10	2.038	1.089

impact of magnification bias at this stage, when the correction is computed for the true *Euclid* data, updated galaxy number counts determined directly from *Euclid* observations should be used to ensure accuracy.

I then combined the two corrections, and calculated the resulting biases as well as the resulting confidence contours for parameter combinations. In addition to the biases, the modified parameter uncertainties in the scenario where the corrections are accounted for were also determined. Next, the additional IA-lensing bias interaction term from Equation (2.13) was included, and the biases and uncertainties were recomputed.

2.6 Results and Discussion

In this section, I report the impact of the various effects studied on *Euclid*. I first present the individual and combined impacts of the reduced shear and magnification bias corrections. The impact of IA-enhanced lensing bias is then discussed.

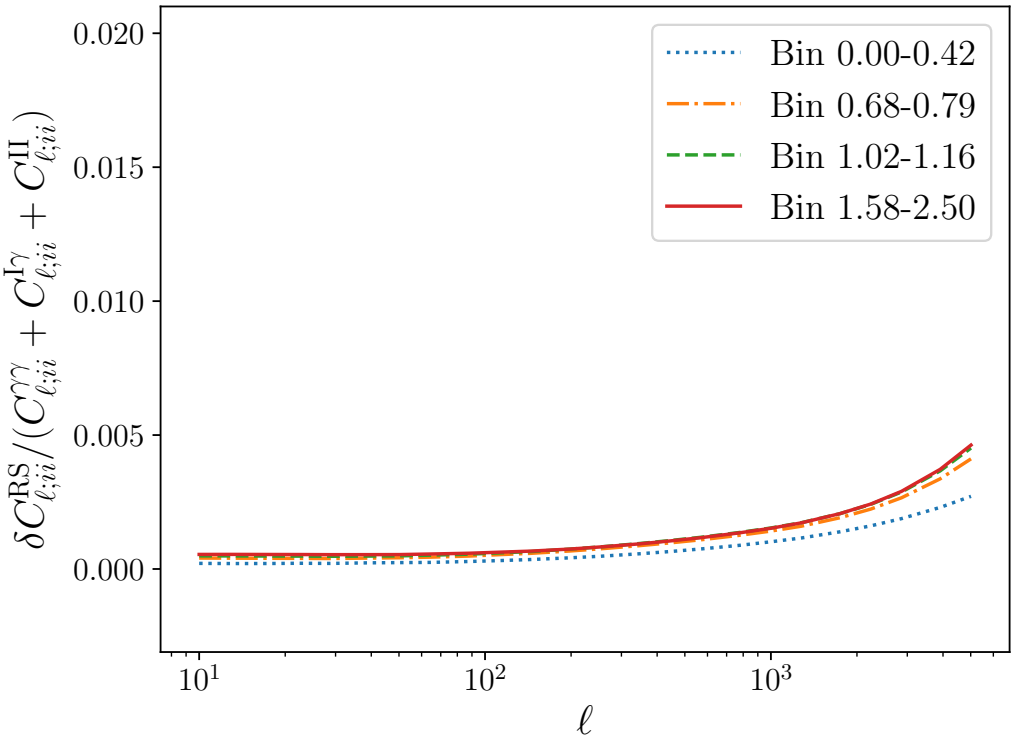

Figure 2.1: The reduced shear correction relative to the observed angular shear auto-correlation spectra (excluding shot noise), for four different redshift bins. For the basic reduced shear correction, the relative size of the correction increases alongside redshift, as the correction term has an additional factor of the lensing kernel compared to the power spectra. The correction plateaus at higher redshifts, because the lensed light encounters the most non-linearity and clustering at lower redshifts. It also increases with ℓ, as convergence tends to be higher on smaller physical scales. The corrections seen here are in the case of the w_0w_aCDM cosmology of Table 1.2. Adapted from Deshpande et al. (2020a). Reproduced with permission from Astronomy & Astrophysics, © ESO.

2.6.1 Reduced Shear Correction Results

The relative magnitude of the basic reduced shear correction described by Equation (2.3), to the observed shear auto-correlation spectra (excluding shot noise), at various redshifts, is shown in Figure 2.1. The correction increases with ℓ, and becomes particularly pronounced at scales above $\ell \sim 100$. This is expected, as small-scale modes grow faster in high-density regions, where the convergence tends to be greater, so there is more power in these regions. One

can also see, from Figure 2.1, that the relative magnitude of the correction increases with redshift, as the reduced shear correction has an extra factor of the lensing kernel, $W_i(\chi)$, in comparison to the angular shear spectra. The lensing kernel increases with comoving distance and, accordingly, redshift. While only a selection of auto-correlation spectra are presented in Figure 2.1 for illustration purposes, the remaining auto and cross-correlation spectra exhibit the same trends.

The uncertainties on the w_0w_aCDM cosmological parameters that are predicted for *Euclid*, are stated in Table 2.2. Correspondingly, Table 2.3 shows the biases that are induced in the predicted cosmological parameters from neglecting the basic reduced shear correction.

Biases are typically considered acceptable when the biased and unbiased confidence regions have an overlap of at least 90%; corresponding to the magnitude of the bias being $< 0.25\sigma$ (Massey et al. 2013). The majority of the biases are not significant, with $\Omega_{\rm m}$, $\Omega_{\rm b}$, h, $n_{\rm s}$, and σ_8 remaining strongly consistent pre- and post-correction. However, $\Omega_{\rm DE}$, w_0, and w_a, all exhibit significant biases of 0.31σ, -0.32σ, and 0.39σ, respectively. Since one of the chief goals of upcoming weak lensing surveys is the inference of dark energy parameters, these biases, which can be readily dealt with, indicate that the reduced shear correction must be included when constraining cosmological parameters from the surveys.

Also shown in Table 2.2 is the change in the uncertainty itself, when the reduced shear correction and its derivatives are included in the Fisher matrix used for prediction. In general, the change is negligible, because the reduced shear correction and its derivatives are relatively small in comparison to the shear spectra and derivatives. In the absence of any corrections, there are near-exact degeneracies which result in large uncertainties when the Fisher matrix is inverted. However, because we are dealing with near-zero eigenvalues in the

Fisher matrix, even subtle changes to the models that encode information can significantly change the resulting parameter constraints.

Since the reduced shear correction depends on the observed density of baryonic matter, including it slightly improves the constraint on $\Omega_{\rm b}$. Also, the predicted uncertainties on h are also reduced, as the correction term has an additional factor of the lensing kernel relative to the angular power spectrum; increasing sensitivity to h by a power of two. The fitting formulae used to describe the matter bispectrum, as part of the correction term, also have a non-trivial dependence on $n_{\rm s}$. This means that the sensitivity to $n_{\rm s}$ is also increased, when the correction is made.

On the other hand, the uncertainty on $\Omega_{\rm DE}$ worsens upon correcting for the reduced shear approximation. This stems from the fact that the derivative of the correction term with respect to $\Omega_{\rm DE}$ is negative, as a higher dark energy density results in a Universe that has experienced a greater rate of expansion, and accordingly is more sparsely populated with matter. Then, convergence in general is lower, and the magnitude of the correction drops as the approximation is more accurate. Therefore, the magnitude of the reduced shear correction and the strength of the $\Omega_{\rm DE}$ signal are inversely correlated. This means that in the case where the reduced shear correction is made, $\Omega_{\rm DE}$ is less well constrained than in the case where there is no correction.

Conversely, increasing w_0 and w_a decreases the rate of expansion of the Universe. Then, sensitivity to w_0 and w_a increases in the case when the correction is made.

2.6.2 Magnification Bias Correction Results

Figure 2.2 shows the magnitude of the basic magnification bias correction, relative to the shear auto-correlation spectra (again excluding shot noise). In this case, the relative magnitude of the correction again increases with redshift.

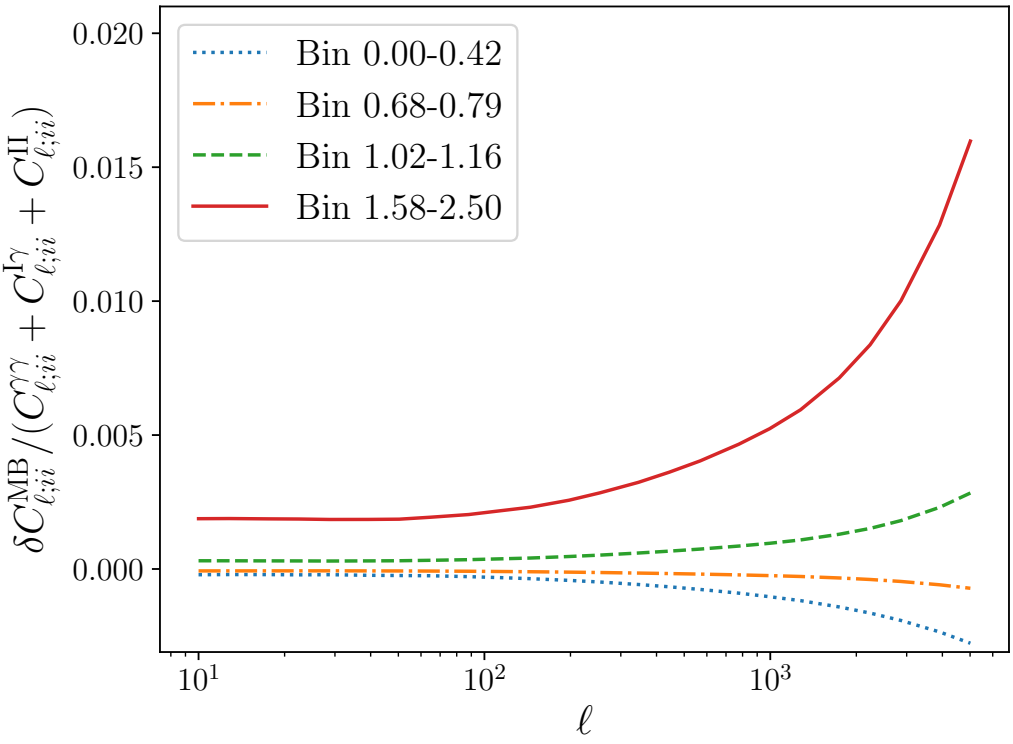

Figure 2.2: The magnification bias correction relative to the observed angular shear auto-correlation spectra (excluding shot noise), for four different redshift bins. The relative size of the correction also increases with redshift. At lower redshifts, the term is subtractive, as the magnification of individual galaxies dominates, leading to an overestimation of the galaxy density. Whereas, at higher redshifts, the dilution of galaxy density dominates, leading to an underestimation if the correction is not made. The corrections seen here are in the case of the $w_0 w_a$CDM cosmology of Table 1.2. Adapted from Deshpande et al. (2020a). Reproduced with permission from Astronomy & Astrophysics, © ESO.

However, in the two lowest redshift bins shown, the correction is subtractive. This is the case for the five lowest redshift bins, of the ten that I consider. This is due to the dilution of galaxy density dominating over the magnification of individual galaxies, as there are fewer intrinsically fainter galaxies at lower redshifts. Conversely, at higher redshifts, there are more fainter sources which lie on the threshold of the survey's magnitude cut, that are then magnified to be included in the sample.

The change in the uncertainty of the cosmological parameters if magnifica-

tion bias is corrected for, and the bias in these parameters if magnification bias is neglected, are given in Table 2.2 and Table 2.3, respectively. Accordingly, correcting for the magnification bias has a noticeable effect on the uncertainties of the parameters Ω_b, h, n_s, Ω_DE, w_0, and w_a. These changes follow the same trends as those seen from the reduced shear correction. I note, however, that the changes in uncertainty induced by the inclusion of these corrections will likely be dwarfed by those resulting from the combination of *Euclid* weak lensing data with other probes; both internal and external. For example, the combination of weak lensing with other *Euclid* probes alone, such as photometric and spectroscopic galaxy clustering as well as the cross-correlation between weak lensing and photometric galaxy clustering, will significantly improve parameter constraints (Euclid Collaboration: Blanchard et al. 2020).

If magnification bias is not corrected for, the values determined for the parameters Ω_m, σ_8, Ω_DE, w_0, and w_a are significantly biased at -0.43σ, 0.36σ, 1.05σ, -0.35σ, and 0.81σ, respectively. All of these biases are higher than the corresponding bias from making the reduced shear approximation. Given that half of the cosmological parameters are significantly biased if magnification bias is neglected, this correction is necessary for *Euclid*.

2.6.3 Combined Correction Results

The relative magnitude of the combined reduced shear and magnification bias correction is shown in Figure 2.3. At the lowest redshifts considered, the subtractive magnification bias correction essentially cancels out the reduced shear correction. Then, at intermediate redshifts, the magnification bias is additive and comparable to the reduced shear correction. However, the dominant part of combined corrections is found at the highest redshifts, where the magnification bias correction is particularly strong. Therefore, the combined correction term is predominantly additive across the survey's redshift bins. The effects of the combined corrections, on the predicted cosmological parameter constraints,

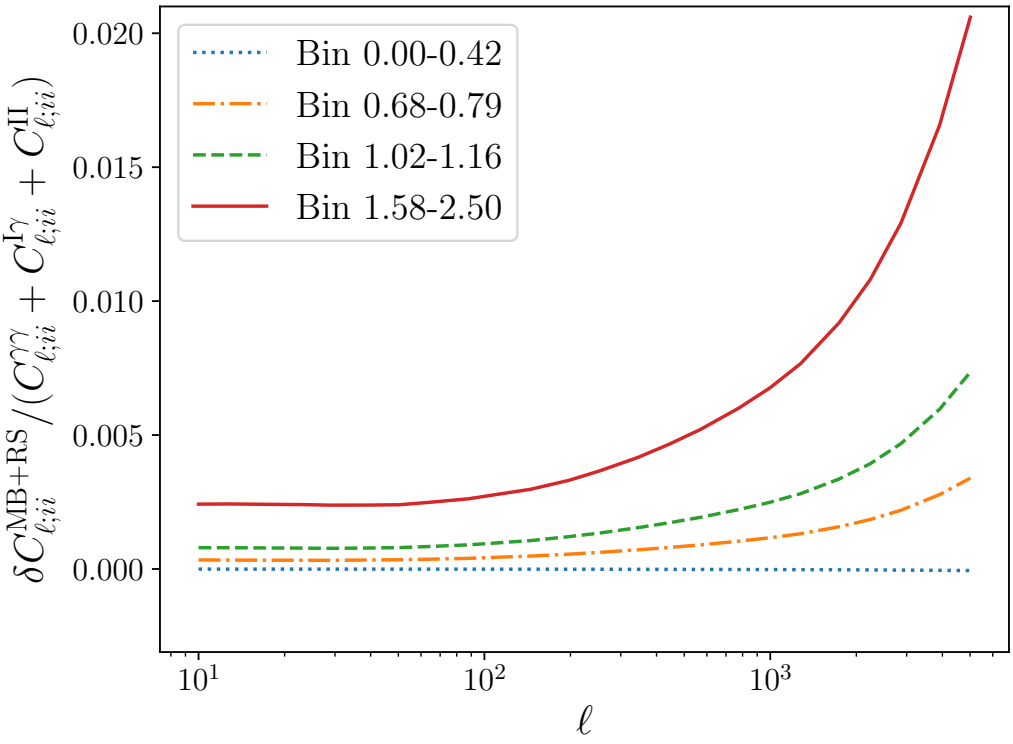

Figure 2.3: The combined corrections relative to the observed angular shear auto-correlation spectra (excluding shot noise), for four different redshift bins. Now, the magnification bias correction effectively cancels out the reduced shear correction at the lowest redshifts. Meanwhile, at intermediate redshifts, the magnification bias is small, but additive; slightly enhancing the reduced shear correction. However, at the highest redshifts, the magnification bias is particularly strong, and the combined correction is significantly greater than at lower redshifts. The corrections seen here are in the case of the $w_0 w_a$CDM cosmology of Table 1.2. Adapted from Deshpande et al. (2020a). Reproduced with permission from Astronomy & Astrophysics, © ESO.

are stated in Table 2.2 and shown in Figure 2.4. The constraints largely remain affected as they were before. The constraints on h worsen slightly when the two corrections are considered together, due to their differing behaviour at lower redshifts. The uncertainty on Ω_{DE} also increases further.

Additionally, Figure 2.5 and Table 2.3 show the biases induced in the cosmological parameters if these corrections are neglected. As expected, the biases add together linearly, and when combined the bias on n_{s} also becomes significant. Now, all but two of the cosmological parameters are significantly biased,

Table 2.2: Predicted uncertainties for the w_0w_aCDM parameters from Table 1.2, for *Euclid*, in the various cases studied. The 'with correction' uncertainties are for the cases when the stated corrections are included Fisher matrix calculation. 'RS' denotes reduced shear, and 'MB' denotes magnification bias. The combined contribution to the uncertainty from both corrections is labelled 'RS+MB'. Adapted from Deshpande et al. (2020a). Reproduced with permission from Astronomy & Astrophysics, © ESO.

Cosmological Parameter	W/o Corr. 1-σ	With RS 1-σ	With MB 1-σ	With RS+MB 1-σ
$\Omega_{\rm m}$	0.012	0.012	0.012	0.013
$\Omega_{\rm b}$	0.021	0.019	0.017	0.017
h	0.13	0.092	0.081	0.082
$n_{\rm s}$	0.032	0.019	0.018	0.018
σ_8	0.012	0.011	0.012	0.012
$\Omega_{\rm DE}$	0.050	0.063	0.059	0.068
w_0	0.17	0.15	0.14	0.17
w_a	0.95	0.91	0.84	1.01

emphasising the need for these two corrections to be applied to the angular power spectra that will be obtained from *Euclid*.

Furthermore, the combination of weak lensing with other probes will improve parameter constraints, whilst leaving the biases resulting from reduced shear and magnification bias unchanged; meaning that the relative biases in this scenario will be even higher. This further stresses the importance of these corrections.

2.6.4 IA-enhanced Lensing Bias Correction Results

When the IA-lensing bias interaction term, from Equation (2.13), is also accounted for, the biases are minimally altered. These are displayed in Table 2.3. From these, one can see that the additional term is non-trivial, but does not induce significant biases in the cosmological parameters obtained at our current level of precision by itself. However, when combined with the basic reduced shear and magnification terms, it leads to the total bias in $\Omega_{\rm b}$ becoming significant, while the total bias in $n_{\rm s}$ is suppressed to now only be on the threshold of significance. The nature of this additional correction, and its

Table 2.3: Biases induced in the w_0w_aCDM parameters of Table 1.2, from neglecting the various corrections, for *Euclid*. 'RS' denotes the bias from only the reduced shear correction, 'MB' denotes only the magnification bias part, and the combined effect is labelled 'RS+MB'. The impact of the IA-enhanced lensing bias correction is also given. Adapted from Deshpande et al. (2020a). Reproduced with permission from Astronomy & Astrophysics, © ESO.

Cosmological Parameter	RS Bias/σ	MB Bias/σ	Combined RS+MB Bias/σ	IA-enhanced Bias/σ
Ω_m	-0.11	-0.43	-0.53	-0.62
Ω_b	0.016	-0.22	-0.20	-0.25
h	0.069	-0.029	0.040	-0.007
n_s	-0.093	-0.24	-0.34	-0.27
σ_8	0.068	0.36	0.43	0.52
Ω_DE	0.31	1.05	1.36	1.32
w_0	-0.32	-0.35	-0.68	-0.67
w_a	0.39	0.81	1.21	1.14

relatively minor impact, is explained by Figure 2.6. This charts the change with ℓ and redshift, of the two components of the IA-enhanced lensing bias, $\delta C^{\mathrm{RS+MB}}_{\ell;ij}$ and $\delta C^{\mathrm{I}}_{\ell;ij}$.

From this, it is seen that for the lowest redshift bins, the two already small terms cancel each other out and at higher redshifts, the latter term is evidently sub-dominant. Accordingly, while upcoming surveys must make the basic reduced shear and magnification bias corrections to extract accurate information, the IA-enhanced correction is not strictly necessary.

2.7 Summary and Outlook

In this chapter, I quantified the impact that making the reduced shear approximation and neglecting magnification bias will have on the angular power spectra of upcoming weak lensing surveys and the resulting cosmological inference. Specifically, I calculated the biases that would be expected in the cosmological parameters obtained from *Euclid*.

By doing so, significant biases were found for Ω_m, σ_8, n_s, Ω_DE, w_0, and w_a of -0.53σ, 0.43σ, -0.34σ, 1.36σ, -0.68σ, and 1.21σ, respectively. I also

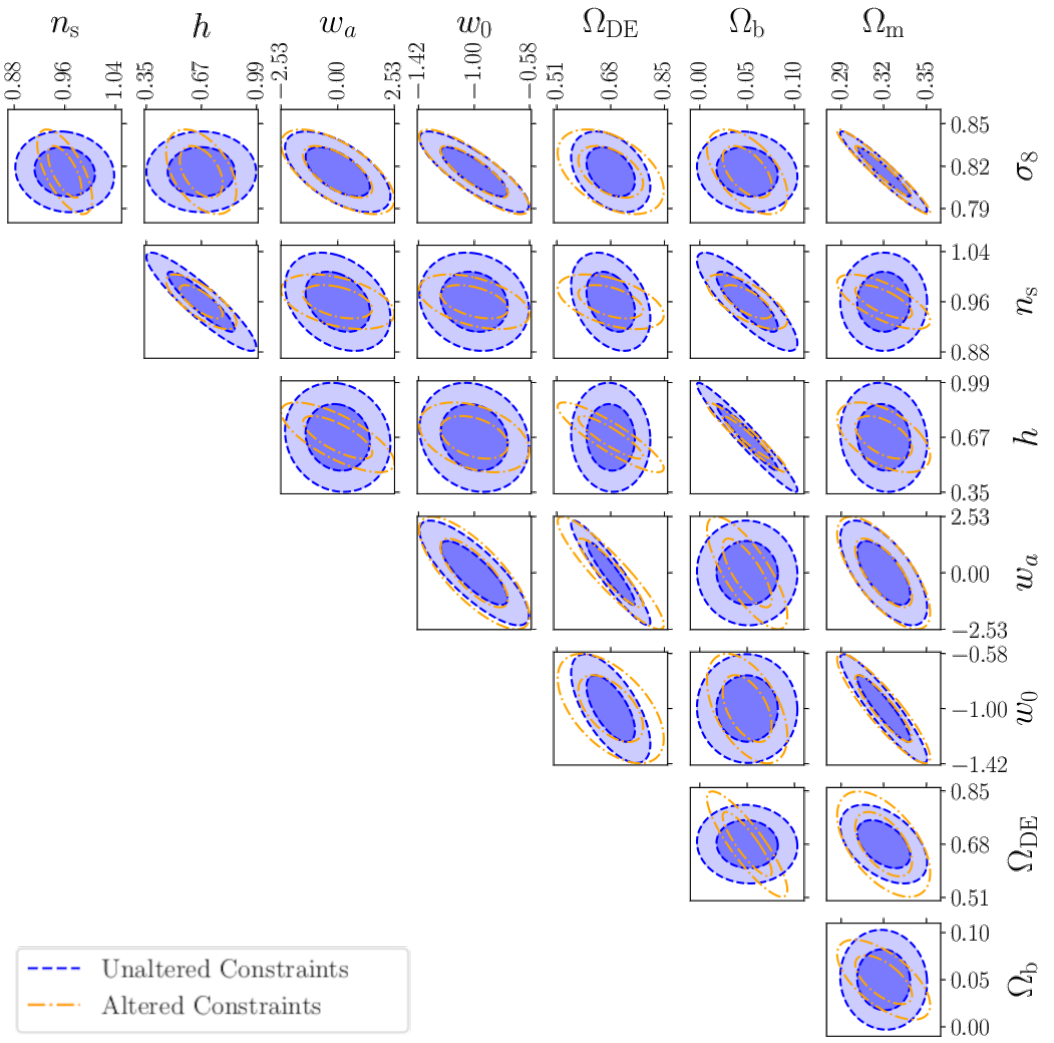

Figure 2.4: The change in the predicted 2-parameter projected 1-σ and 2-σ contours on the w_0w_aCDM cosmological parameters from Table 1.2 for *Euclid*, when including the reduced shear and magnification bias corrections, and their derivatives, in the Fisher matrix calculation. The contours decrease in size for the parameters Ω_b, h, n_s, w_0, and w_a. However, in the case of Ω_{DE}, the contours increase in size. Adapted from Deshpande et al. (2020a). Reproduced with permission from Astronomy & Astrophysics, © ESO.

built the formalism for an IA-enhanced correction. This was discovered to be sub-dominant. Given the severity of the calculated biases, I conclude that it is necessary to make both the reduced shear and magnification bias corrections for Stage IV experiments.

However, there are important limitations to consider in the approach described here. In calculating these corrections, the Limber approximation was

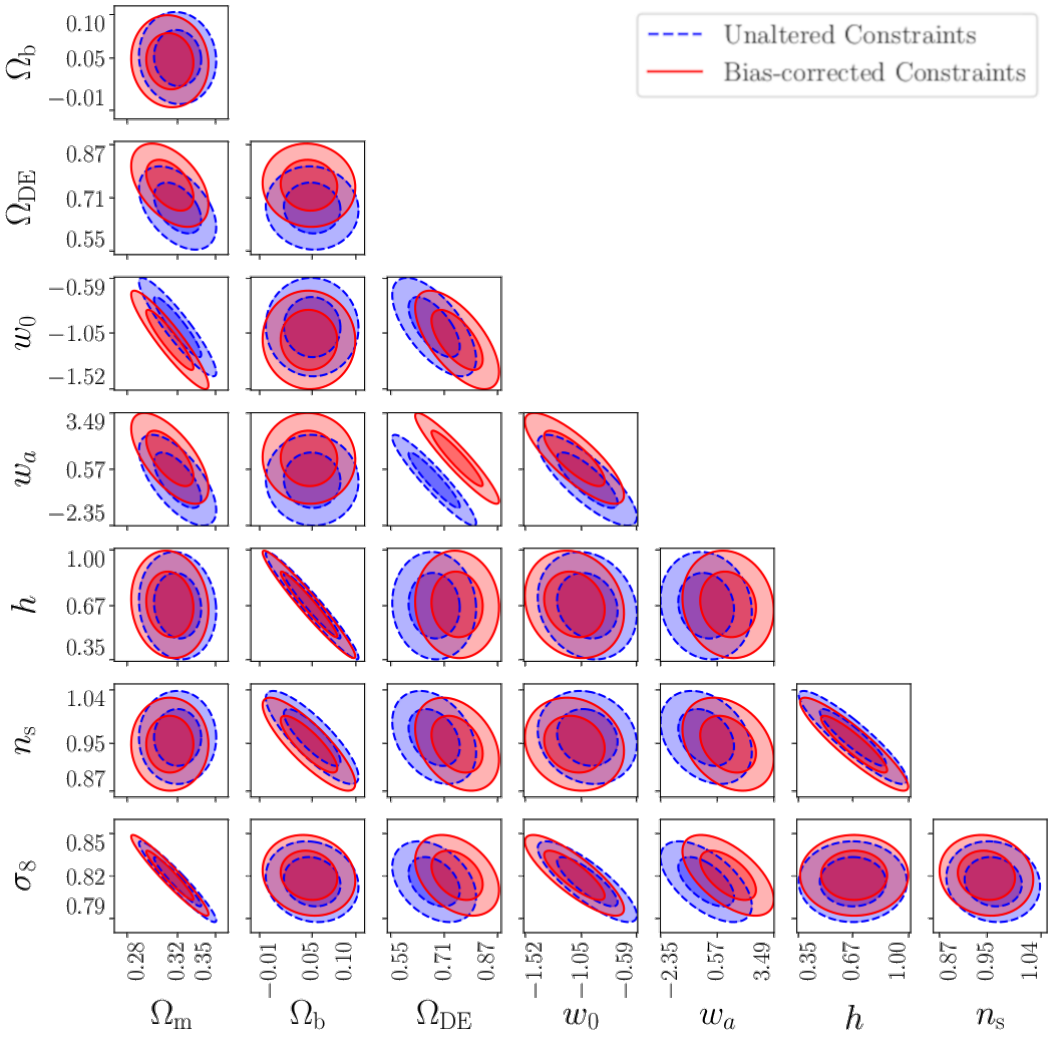

Figure 2.5: Predicted 2-parameter projected 1-σ and 2-σ contours on the w_0w_aCDM cosmological parameters from Table 1.2, for *Euclid*. The optimistic case, probing ℓ-modes up to 5000, is considered here. The biases in the predicted values of the cosmological parameters, that arise from neglecting the basic reduced shear and magnification bias corrections, are shown here. The additional IA-lensing bias terms are not included. Of these, $\Omega_{\rm m}$, σ_8, $n_{\rm s}$, $\Omega_{\rm DE}$, w_0, and w_a have significant biases of -0.53σ, 0.43σ, -0.34σ, 1.36σ, -0.68σ, and 1.21σ, respectively. Adapted from Deshpande et al. (2020a). Reproduced with permission from Astronomy & Astrophysics, © ESO.

still made. This approximation is typically valid above $\ell \sim 100$. But, for *Euclid* we expect to reach ℓ-modes of ten. Therefore, the impact of this simplification at the correction level must be evaluated.

Given that the dominant contributions to the reduced shear and magnification bias corrections come from ℓ-modes above 100, I would not expect the

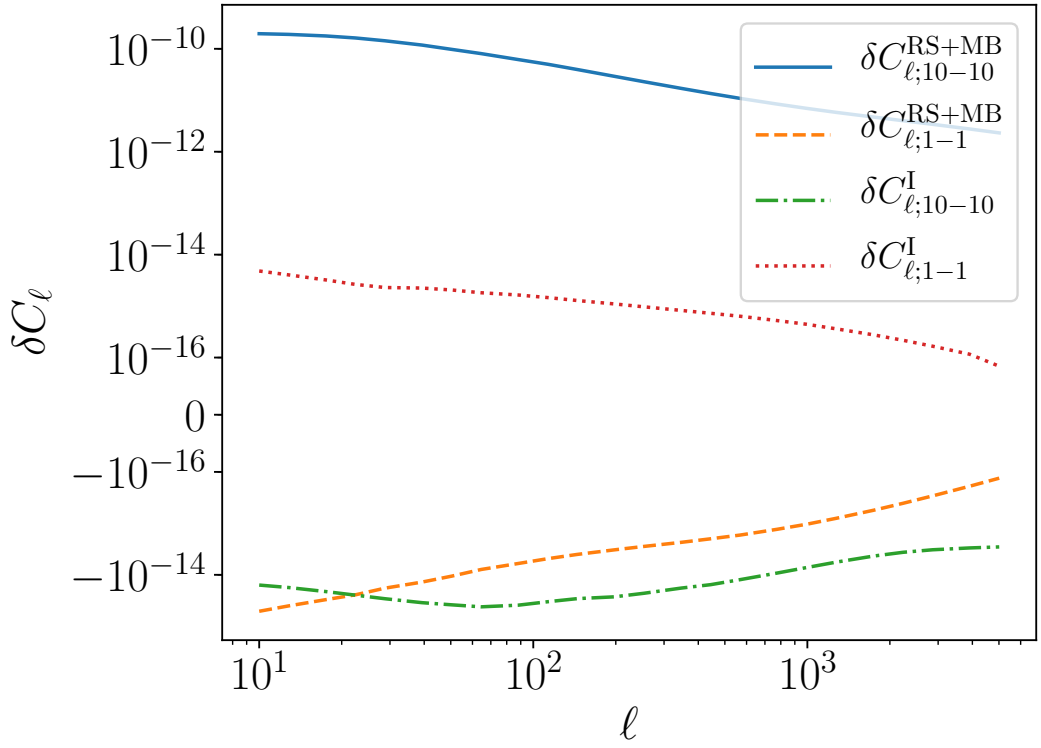

Figure 2.6: The IA-enhanced lensing bias correction of Equation (2.13) compared with the combined reduced shear and magnification bias corrections. The cross-spectra of the first ($0.001 \leq z \leq 0.418$) and tenth bins ($1.576 \leq z \leq 2.50$) are shown. For the first bin, the basic correction is already sub-dominant, and the additional IA-enhanced term cancels it out. In the higher redshift bin, the second term is sub-dominant. This trend persists across all bins. Adapted from Deshpande et al. (2020a). Reproduced with permission from Astronomy & Astrophysics, © ESO.

Limber approximation to significantly affect the resulting cosmological biases. However, an explicit calculation is still warranted. Furthermore, the various correction terms depend on bispectra which are not well understood: they both involve making a plethora of assumptions, and using fitting formulae that have accuracies of only 30-50% on small scales.

In addition, this work does not consider the impact of baryonic feedback on the corrections. We would expect that baryonic feedback behaves in a similar way to lowering the fiducial value σ_8 (see Appendix C of Deshpande et al. 2020a), that is, they both suppress structure growth in high density regions.

Accordingly, it is likely that the inclusion of baryonic feedback would have an effect on these corrections. If the matter power spectrum is suppressed by a greater fraction than the matter bispectrum, then the biases will increase. However, it is not currently clear to what degree the matter bispectrum is suppressed relative to the matter power spectrum, and existing numerical simulations propose seemingly inconsistent answers (see e.g. Barreira et al. 2019; Semboloni et al. 2013). For this reason, I cannot robustly quantify the impact of baryonic feedback on the biases. As knowledge of the impact of baryons on the bispectrum improves, the reduced shear and magnification bias corrections should be modified accordingly.

An additional hurdle is the large computational expense of these terms; arising from the multiple nested integrals needing numerical computation. Computing the reduced shear and magnification bias corrections for this work took on the order of 24 hours when multiprocessing across 100 CPU threads. Including the IA-enhanced correction term increases this to ~ 48 hours. This expense can be prohibitive if the correction is to be included in inference methods. Accordingly, there is also merit in exploring whether the existing processes can be optimised, as well as if these corrections can be forward modelled. Another recent approach that has shown promise in reducing modelling time at inference is the use of machine learning-based emulation (see e.g. Spurio Mancini et al. 2022).

Chapter 3

Post-Limber Reduced Shear & Magnification Bias

This chapter adapts Deshpande & Kitching (2020).

In the following chapter, I discuss the dependency of the corrections for the reduced shear approximation and magnification bias on another common assumption; the Limber approximation. In particular, I demonstrate how the Limber approximation can be relaxed during the calculation of the convergence bispectrum, and the corresponding effect on the two corrections. These calculations are performed in the context of a *Euclid*-like survey.

3.1 Motivation and Outline

Weak gravitational lensing can be a powerful tool to refine our knowledge of the currently favoured standard model for the Universe, the ΛCDM model. A useful manifestation of this effect is cosmic shear: the distortion of the observed shapes of distant galaxies due to weak gravitational lensing by the LSS. Impending Stage IV cosmic shear surveys necessitate a reevaluation of approximations made in our theoretical analyses, owing to their significantly increased precision.

One such approximation, that is regularly made, is the Limber approximation. In this, computationally challenging integrals over highly oscillatory

spherical Bessel functions are replaced with delta functions at their peaks. The impact of relaxing this approximation, together with the Hankel transform and flat-sky approximations, for a *Euclid*-like experiment has been evaluated (Kitching et al. 2017). As demonstrated in Chapter 2, two further effects that have recently been shown to be important for Stage IV experiments are the reduced shear approximation and magnification bias. Compounding the complexity of correcting for any one such approximation is that the procedure for doing so often involves making one of the others.

In this chapter, I focus on the reduced shear approximation and magnification bias, and their inter-dependency with the Limber approximation. When cosmic shear is probed, the quantity measured is reduced shear, rather than shear itself. Under the reduced shear approximation, the statistics of one are taken to equal those of the other. On the other hand, magnification bias refers to the change of the observed galaxy number density due to individual sources or patches of the sky being magnified. These two effects are treated together because their corrections take mathematically similar forms. However, these corrections depend on the convergence bispectrum, and one typically evaluates this quantity under the Limber approximation.

Here, I forgo the Limber approximation when calculating the convergence bispectrum. Subsequently, I measure the resulting change in the magnification bias and reduced shear corrections for a *Euclid*-like survey, and compare it to the sample variance of the survey. I also demonstrate that the resulting change does not induce significant biases in inferred $w_0 w_a$CDM cosmological parameters if neglected.

The remainder of this chapter is structured thusly: Section 3.2 first contextualises the Limber approximation by reviewing its implementation at the angular power spectrum level. Then, in Section 3.3, I describe its implementation at the bispectrum level, as well as how it can be relaxed. The modelling

specifics used in this investigation are detailed in Section 3.4. The results of the investigation are then reported and discussed in Section 3.5, before I conclude the chapter with a summary in Section 3.6.

3.2 Shear on a Sphere and the Limber Approximation

The derivation of the shear angular power spectra in Section 1.2.6 is predicated on the Limber approximation. Here, I describe the general case, and how the Limber approximation is applied to it.

In practice, shear is observed on the sphere of the sky. For a given tomographic redshift bin, i, the spin-2 cosmic shear, in spherical-harmonic space, can be represented as:

$$\widetilde{\gamma}_{i;\ell m} = \sqrt{\frac{2}{\pi}} \sum_{g} \gamma_g \left(\theta_g, \chi_g\right) j_\ell \left(k\chi_g\right) {}_2Y^*_{\ell m}(\hat{\boldsymbol{k}}), \tag{3.1}$$

where m is the magnitude of angular wavevector $\boldsymbol{m}$ analogous to ℓ, $\boldsymbol{k}$ is a spatial momentum vector with magnitude $k = |\boldsymbol{k}|$, j_ℓ are spherical Bessel functions, ${}_2Y^*_{\ell m}$ are spin-weighted with spin= 2 spherical harmonics, * denotes the complex conjugate, and γ_g is the shear of individual galaxies in the bin, denoted by subscript g, which are then summed over. Generalised to a shear field in real-space, rather than a sum over galaxies, this becomes:

$$\widetilde{\gamma}_{i;\ell m} = \sqrt{\frac{2}{\pi}} \int \mathrm{d}^3\boldsymbol{r}\, \gamma_i(\mathbf{r})\, j_\ell \left(k\chi\right)\, {}_2Y^*_{\ell m}(\hat{\boldsymbol{k}}), \tag{3.2}$$

where $\boldsymbol{r}$ are the spatial coordinates (θ, χ). The inverse transform is:

$$\gamma_i(\mathbf{r}) = \sqrt{\frac{2}{\pi}} \int \mathrm{d}k\, k \sum_{\ell=0}^{\infty} \sum_{m=-\ell}^{\ell} \widetilde{\gamma}_{i;\ell m}\, j_\ell \left(k\chi\right)\, {}_2Y_{\ell m}(\hat{\boldsymbol{r}}). \tag{3.3}$$

Now, under the flat-sky approximation (Kitching et al. 2017), one can as-

sume that the angular coverage of the observed field is small, and therefore that the angular component can be treated with planar geometry. The three-dimensional spherical expansion can then be represented as a three-dimensional Fourier expansion:

$$\gamma_i(\mathbf{r}) = \frac{1}{(2\pi)^3}\int \mathrm{d}^3\boldsymbol{k}\,\widetilde{\gamma}_i(\boldsymbol{k},\chi)\,e^{i\boldsymbol{k}\cdot\boldsymbol{r}}, \tag{3.4}$$

where the i in the exponential is the imaginary unit, not the bin index as used to subscript the observables. Then, using the identity:

$$e^{i\boldsymbol{k}\cdot\boldsymbol{r}} = 4\pi\sum_{\ell=0}^{\infty}\sum_{m=-\ell}^{m=\ell} i^\ell\, j_\ell\left(k\chi\right){}_2Y^*_{\ell m}(\hat{\boldsymbol{k}})\,{}_2Y_{\ell m}(\hat{\boldsymbol{r}}), \tag{3.5}$$

as well as trivially taking the Fourier-space equivalent of the results of Section 1.2 (implicitly under the pre-factor unity and Born approximations), the shear on a sphere can be expressed as:

$$\widetilde{\gamma}_{i;\ell m} = 4\pi i^\ell\int_0^{\chi_{\rm lim}}\mathrm{d}\chi W_i(\chi)\int_0^\infty\frac{\mathrm{d}^3\boldsymbol{k}}{(2\pi)^3}\,j_\ell(k\chi)\,{}_2Y^*_{\ell m}(\hat{\boldsymbol{k}})\,\widetilde{\delta}(\boldsymbol{k},\chi), \tag{3.6}$$

where $\widetilde{\delta}$ is the density contrast of the Universe in Fourier-space. The three-dimensional, spherical angular power spectrum is then:

$$\begin{aligned} C_{\ell;ij} = &\left[\frac{3H_0^2\Omega_{\rm m}}{2c^2}\right]^2\int_0^{\chi_{\rm lim}}\frac{\mathrm{d}\chi}{S_K(\chi)^2}\left[\frac{S_k(\chi)}{a(\chi)}\right]^2\int_\chi^{\chi_{\rm lim}}\mathrm{d}\chi'\,n_i\left(\chi'\right)n_j\left(\chi'\right)\\ &\times\left[\frac{S_k\left(\chi'-\chi\right)}{S_k\left(\chi'\right)}\right]^2\int_0^\infty\frac{\mathrm{d}k}{k^2}\,j_\ell(k\chi)\,j_\ell(k\chi')\,P_{\delta\delta}(k,\chi), \end{aligned} \tag{3.7}$$

under the equal-time correlators assumption (Kitching & Heavens 2017). The Limber approximation is then made by noticing that the integral over k will peak when $\chi \simeq \chi'$ (specifically when $k = (\ell+1/2)/\chi$, see LoVerde & Afshordi 2008), and replacing the spherical Bessel functions with a Dirac delta function. This recovers Equation (1.87).

For a *Euclid*-like experiment, it has been shown that making this approximation produces an error that makes up less than 10% of the error budget (Kitching et al. 2017). Accordingly at the power spectrum level this approximation can safely be made. However, until this investigation, its impact on the bispectrum, and dependent quantities, remained unknown.

3.3 The Convergence Bispectrum

The reduced shear and magnification bias corrections, encompassed by Equation (2.3) and Equation (2.11) respectively, both rely on calculating the convergence bispectrum. Until now, this has been done under the assumption of the Limber approximation, leading to Equation (2.4). From Equation (3.6), the trigonometric relationship between convergence and shear, and by noting that one is always free to choose a set of coordinates such that $\phi_\ell = 0$, the equivalent expression for the convergence is obtained. Accordingly, the observed convergence in spherical harmonic space on a sphere is written as:

$$\widetilde{\kappa}_{i;\ell m} = 4\pi i^\ell \int_0^{\chi_{\rm lim}} \mathrm{d}\chi W_i(\chi) \int_0^\infty \frac{\mathrm{d}^3 k}{(2\pi)^3} j_\ell(k\chi)\, {}_2Y_{\ell m}(\hat{\boldsymbol{k}})\widetilde{\delta}(\boldsymbol{k},\chi). \tag{3.8}$$

The bispectrum is defined on the sphere as (Assassi et al. 2017):

$$\langle \widetilde{\kappa}_{i;\ell_1 m_1} \widetilde{\kappa}_{j;\ell_2 m_2} \widetilde{\kappa}_{q;\ell_3 m_3} \rangle = \mathcal{G}^{\ell_1\ell_2\ell_3}_{m_1 m_2 m_3}\, B^{\kappa\kappa\kappa}_{ijq}(\boldsymbol{\ell_1}, \boldsymbol{\ell_2}, \boldsymbol{\ell_3}), \tag{3.9}$$

where $\mathcal{G}^{\ell_1\ell_2\ell_3}_{m_1 m_2 m_3}$ is the Gaunt integral:

$$\begin{aligned} \mathcal{G}^{\ell_1\ell_2\ell_3}_{m_1 m_2 m_3} = &\sqrt{\frac{(2\ell_1+1)(2\ell_2+1)(2\ell_3+1)}{4\pi}} \\ &\times \begin{pmatrix} \ell_1 & \ell_2 & \ell_3 \\ 0 & 0 & 0 \end{pmatrix} \begin{pmatrix} \ell_1 & \ell_2 & \ell_3 \\ m_1 & m_2 & m_3 \end{pmatrix}, \end{aligned} \tag{3.10}$$

in which the final matrix on the R.H.S. is the Wigner $3j$-symbol.

However, Equation (3.9) is highly challenging computationally, due to the multiple nested-integrals present. Fortunately, this calculation can be simplified by recognizing that, given that the convergence is a projection of the density contrast, the convergence bispectrum is a projection of the matter bispectrum, $B_{\delta\delta\delta}$, and the matter bispectrum is separable. This means that it can be expressed as the linear sum of products of functions of momenta:

$$B_{\delta\delta\delta}(\boldsymbol{k_1}, \boldsymbol{k_2}, \boldsymbol{k_3}; \chi_1, \chi_2, \chi_3) = \sum_{n_1,n_2,n_3} f_{1;n_1}(k_1, \chi_1) f_{2;n_2}(k_2, \chi_2) \times f_{3;n_3}(k_3, \chi_3), \tag{3.11}$$

where n_1, n_2, n_3 are power-law indices in their respective functions. For a review of why this holds true, see Lee & Dvorkin (2020). This can be seen directly by considering the 2PT linear bispectrum (Fry 1984):

$$B_{\delta\delta\delta}(\boldsymbol{k_1}, \boldsymbol{k_2}, \boldsymbol{k_3}; \chi_1, \chi_2, \chi_3) = 2F_2\left(\boldsymbol{k_1}, \boldsymbol{k_2}\right) P^{\rm lin}_{\delta\delta}(k_1, \chi_1) P^{\rm lin}_{\delta\delta}(k_2, \chi_2) + \text{cyc.}, \tag{3.12}$$

where $P^{\rm lin}_{\delta\delta}$, is the linear matter power spectrum, and:

$$F_2(\boldsymbol{k_1}, \boldsymbol{k_2}) = \frac{5}{7} + \frac{1}{2}\frac{\boldsymbol{k_1}\cdot\boldsymbol{k_2}}{k_1 k_2}\left(\frac{k_1}{k_2} + \frac{k_2}{k_1}\right) + \frac{2}{7}\left(\frac{\boldsymbol{k_1}\cdot\boldsymbol{k_2}}{k_1 k_2}\right)^2. \tag{3.13}$$

The full non-linear bispectrum described by Equation (2.5) is then recovered by multiplying this expression by fitting functions determined from N-body simulations. Now, the separability of the matter bispectrum can be leveraged to express the convergence bispectrum as:

$$B^{\kappa\kappa\kappa}_{ijq}(\boldsymbol{\ell_1}, \boldsymbol{\ell_2}, \boldsymbol{\ell_3}) = \frac{1}{(2\pi^2)^3}\int_0^{\chi_{\rm lim}} \mathrm{d}r\, r^2 [I^{(1,n_1)}_{\ell_1;i}(r) \times I^{(2,n_2)}_{\ell_2;j}(r) I^{(3,n_3)}_{\ell_3;q}(r) + \text{perms.}], \tag{3.14}$$

within which:

$$I_{\ell_n}^{(a,n_a)}(r) = 4\pi \int_0^{\chi_{\rm lim}} \mathrm{d}\chi\, W(\chi) \int_0^{\infty} \mathrm{d}k\, j_\ell(k\chi) j_\ell(kr)\, k^2 f_{a;n_a}(k,\chi). \tag{3.15}$$

Spherical Bessel functions are highly oscillatory, making the integrals in Equation (3.15) a significant computational challenge. To bypass this, one can realize that the integral in k will peak when $\chi \simeq r$, and replace the k-integral with a Dirac delta function, $\delta_{\rm D}$:

$$\begin{aligned} I_{\ell_n}^{(a,n_a)}(r) &\approx 4\pi \int_0^{\chi_{\rm lim}} \mathrm{d}\chi\, W(\chi)\, \frac{\pi}{2r^2} f_{a;n_a}(k=\ell/r,\chi)\delta_{\rm D}(\chi - r) \\ &\approx \frac{2\pi^2}{r^2} W(r)\, f_{a;n_a}(k=(\ell+1/2)/r, r). \end{aligned} \tag{3.16}$$

This is the application of the Limber approximation for the convergence bispectrum. In this investigation, I evaluated the impact of making this approximation on both the bispectrum itself and the two correction terms.

3.4 Modelling Methodology

As in Chapter 2, I used the *Euclid*-like modelling specifics of Section 1.3.2, and the w_0w_aCDM fiducial cosmology described in Section 1.3.3. A *Euclid*-like survey would be expected to have ten equi-populated redshift bins, covering the range 0 – 2.5. However, in this chapter, I only computed the bispectra and correction terms for the auto-correlation of four redshift bins: $[0.001, 0.418]$, $[0.678, 0.789]$, $[1.019, 1.155]$, and $[1.576, 2.50]$. These serve to sufficiently illustrate the impact of the Limber approximation across the survey's redshift range, while avoiding the significant computational expense of computing the 55 total bin combinations. Furthermore, I once again used the `CLASS` cosmology package to compute the matter power spectrum, as well as cosmological distances. The matter power spectrum was again calculated using the non-linear corrections of Takahashi et al. (2012) and Mead et al. (2015).

One important distinction in the methodology of this investigation, relative to Chapter 2, is that only the Gaussian covariance of Equation (2.18) is used in Fisher matrix calculations, and SSC terms are neglected. This is done in order to reduce the already significant computational load. Additionally, the SSC terms are not involved in the calculation of the corrections, and accordingly their exclusion should not significantly change the relative magnitudes of any biases as a fraction of the predicted cosmological parameter uncertainties, particularly given that the inclusion of SSC terms changes the projected parameter contours by on the order of a few percent (Barreira et al. 2018).

Using the discussed modelling specifications, I computed the convergence bispectrum, both with and without making the Limber approximation. I computed the bispectra for equilateral configurations where $\ell_1 = \ell_2 = \ell_3$, and isosceles configurations where $\ell_1 = \ell_2 \neq \ell_3$. I studied two different isosceles configurations, one where $\ell_3 = 20$, and another where $\ell_3 = 100$.

The separability of the bispectrum was used to reduce some of the computational complexity of the post-Limber case. The 2PT expression for the bispectrum stated in Equation (3.12) is valid when $\ell_1, \ell_2, \ell_3 < 100$. Accordingly, it is also true that the bispectrum's individual separated components $I^{a,n_a}_{\ell_n}$, as defined in Equation (3.15), will match sufficiently well whether only the 2PT expression or the non-linear fitting function expression of Equation (2.6) is used in their computation, when $\ell_n < 100$. Therefore, using the 2PT expression for a particular $I^{a,n_a}_{\ell_n}$ when the corresponding $\ell_n < 100$, avoids the laborious numerical integration over the fitting functions of Equation (2.6) in that case; reducing the overall total computation time.

I then computed the reduced shear and magnification bias corrections. However, the integration over the bispectrum necessitated by these terms is an intractable computation to perform directly for the post-Limber case, given the number of steps in ℓ-space required. It would take on the order of ~ 50 weeks

for just one bin auto-correlation[1]. To bypass this hurdle, I first computed the post-Limber and Limber approximated bispectra on a grid of 1331 points in ℓ-space, with each ℓ_i sampled logarithmically in the range $10 \leq \ell_i \leq 5000$, for each bin. The ratio of these quantities at each point was then taken, and these ratios were interpolated over, using linear 3D interpolation. This gave a function which maps the Limber approximated bispectrum onto the post-Limber case. In computing the post-Limber reduced shear and magnification bias corrections, I calculated the required bispectra as in the Limber approximated case, and used the previously interpolated function to scale these to their post-Limber counterparts.

I compared these corrections to the sample variance of a *Euclid*-like survey. The sample variance from LSS for a weak lensing galaxy survey is given by:

$$\delta C^{\mathrm{SV}}_{\ell;ij} \,/\, C^{\gamma\gamma}_{\ell;ij} = \sqrt{2}\,[f_{\mathrm{sky}}(2\ell+1)]^{-1/2}, \tag{3.17}$$

where f_{sky} is the fraction of surveyed (Weinberg 2008).

Then, I defined a worst-case scenario where the difference between post-Limber and Limber approximated corrections, $\Delta C_{\ell;ij} \approx 0.01\, C^{\gamma\gamma}_{\ell;ij}$ for all bin combinations and ℓ-modes. This corresponds to the largest difference seen for these survey specifications, at $\ell \approx 5000$ for the auto-correlation of bin $1.56 - 2.50$. I then calculated the cosmological parameter biases resulting from $\Delta C_{\ell;ij}$. For this calculation, I considered the auto- and cross-correlation spectra for all ten redshift bins specified in Section 1.3.2.

3.5 Results and Discussion

Here, I present the effect of relaxing the Limber approximation on the quantities examined. Firstly, I report the impact on the convergence bispectrum in

[1]For a `Python` script multi-processed across 100 CPU threads.

the four studied redshift bins. Then, I do the same for the reduced shear and magnification bias corrections to the angular power spectrum.

3.5.1 The Post-Limber Convergence Bispectrum

The effect of relaxing the Limber approximation for the equilateral configuration of the convergence bispectrum is shown in Figure 3.1, for all of the examined redshift bins. From this, I find that for all redshift bins, the Limber approximation over-predicts the bispectrum for ℓ-modes below $\ell \sim 60$. Additionally, the over-prediction worsens at lower ℓ-modes, and for higher redshift bins.

Furthermore, Figures 3.2 and 3.3 show the bispectra of the four bins for two different isosceles configurations. The configurations shown are when $\ell_1 = \ell_2$ and $\ell_3 = 20$, and when $\ell_1 = \ell_2$ and $\ell_3 = 100$, respectively. For the former of these cases, I note that the bispectrum is over-predicted by the Limber approximation for all ℓ-modes.

On the other hand, when in an isosceles configuration with $\ell_3 = 100$, one sees much the same trends as in Figure 3.1. This implies that the Limber approximation fails for the convergence bispectrum when any one of its sides $\ell_i < 60$. Similar discrepancies at low ℓ-modes are seen for both the equilateral and isosceles configurations in Munshi et al. (2020), where the Limber-approximated theoretical expression for the bispectrum is compared to the bispectrum measured from full-sky simulations.

Accordingly, if ℓ-modes below 60 are probed, as will be the case for Stage IV experiments, the Limber approximation cannot be used to compute the bispetrum in this regime. This presents a computational challenge, as computing the post-Limber bispectrum is two orders-of-magnitude slower than using the Limber approximation.

However, the separability of the bispectrum, discussed in Section 3.3, offers

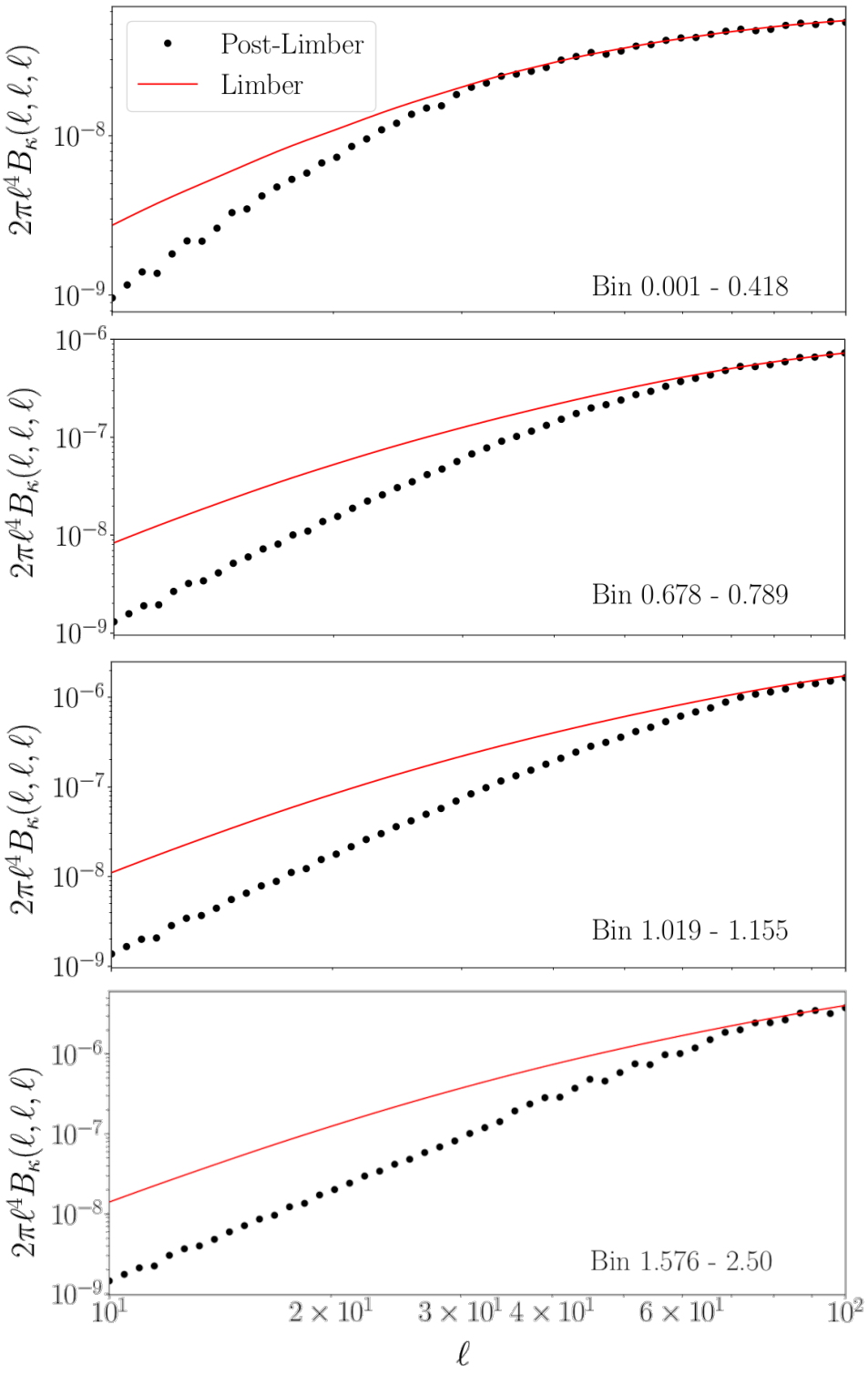

Figure 3.1: Comparison of the equilateral configuration convergence bispectrum with and without making the Limber approximation, for the auto-correlation of four redshift bins across the redshift range of a *Euclid*-like survey. The Limber approximation fails when $\ell < 60$, and overestimates the bispectrum. This over-prediction is worse at higher redshifts and lower ℓ-modes. Adapted from Deshpande & Kitching (2020).

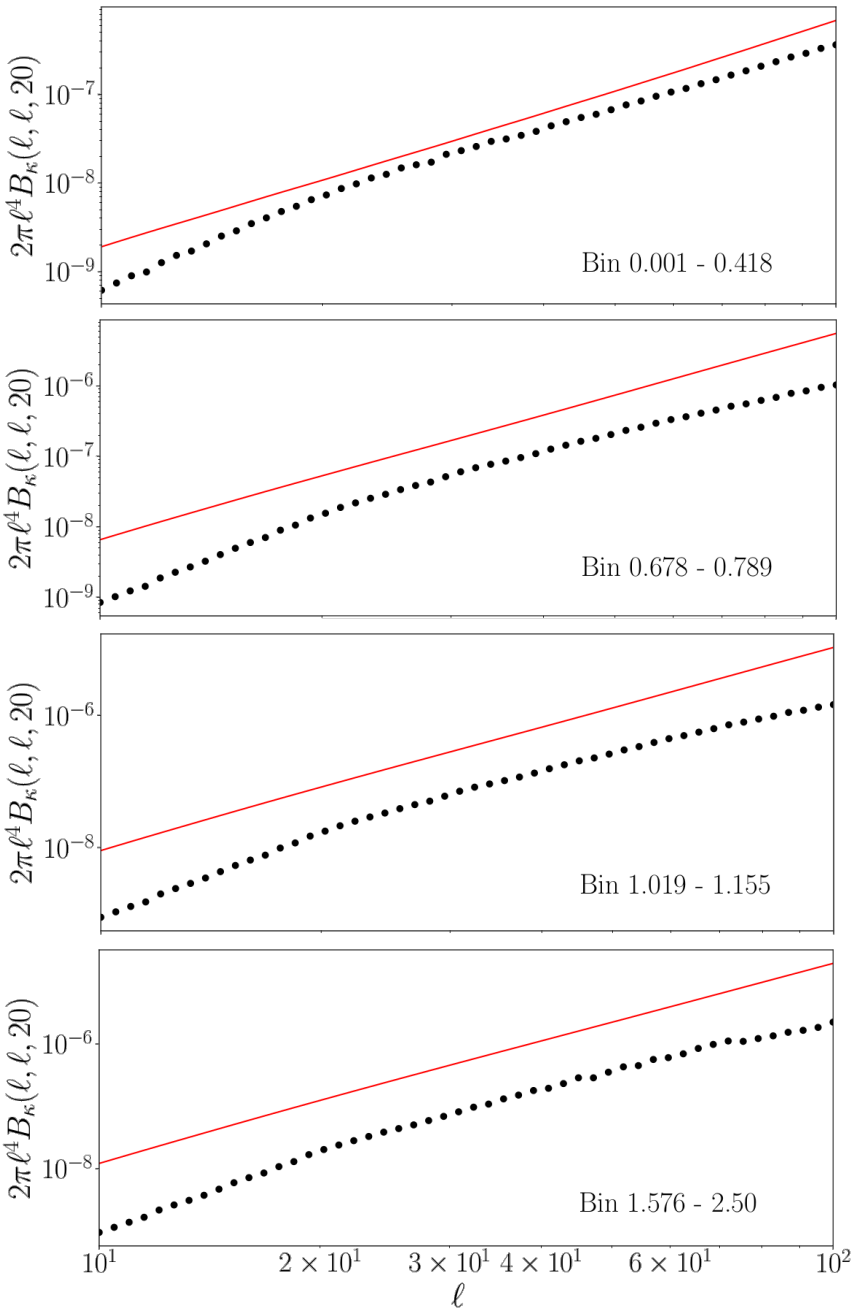

Figure 3.2: Isosceles configuration bispectra with $\ell_3 = 20$, for four tomographic bins across the redshift range of a *Euclid*-like survey. The values of the bispectra with and without making the Limber approximation are shown. Here, the Limber approximation over-predicts the bispectrum for all values of ℓ_1 and ℓ_2. However, when $\ell_3 = 100$, as shown in Figure 3.3 one sees similar behaviour to the equilateral case shown in Figure 3.1, in that the Limber approximation only results in over-prediction for $\ell_1 = \ell_2 < 60$. This suggests the Limber approximation fails when any one of the sides of the bispectrum triangle $\ell_i < 60$. Otherwise, the trends match those seen for the equilateral configuration, with over-prediction worsening at higher redshift, and lower ℓ. Adapted from Deshpande & Kitching (2020).

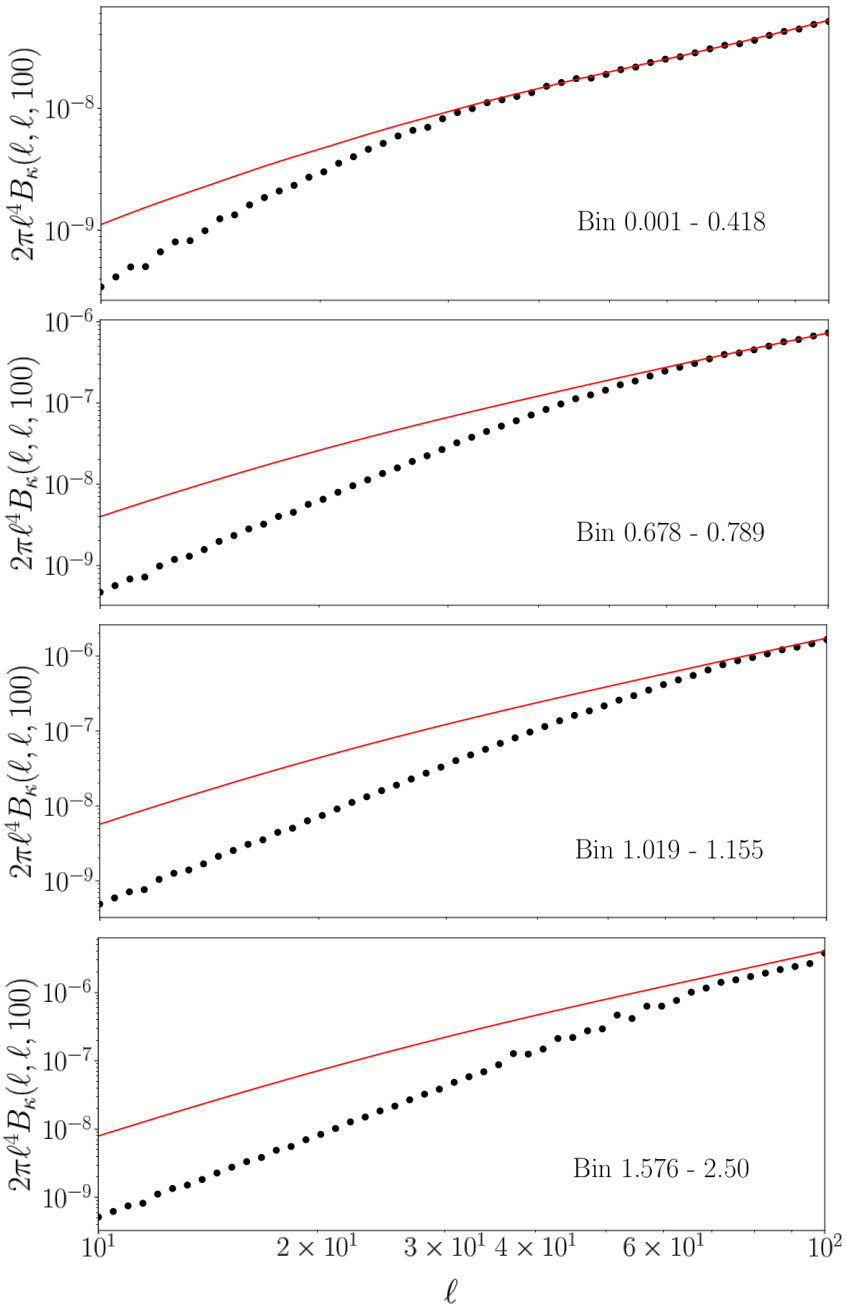

Figure 3.3: Isosceles configuration bispectra with $\ell_3 = 100$, for four tomographic bins across the redshift range of a *Euclid*-like survey. The values of the bispectra with and without making the Limber approximation are shown. Here, one sees similar behaviour to the equilateral case shown in Figure 3.1, in that the Limber approximation only results in over-prediction for $\ell_1 = \ell_2 < 60$. However, when $\ell_3 = 20$ as in Figure 3.2, the Limber approximation over-predicts the bispectrum for all values of ℓ_1 and ℓ_2. This suggests the Limber approximation fails when any one of the sides of the bispectrum triangle $\ell_i < 60$. Otherwise, the trends match those seen for the equilateral configuration, with over-prediction worsening at higher redshift, and lower ℓ. Adapted from Deshpande & Kitching (2020).

a solution. For a given configuration, if one of the sides of the bispectrum $\ell_i < 60$, only the instances of Equation (3.15) corresponding to that side need to be computed without the Limber approximation. Furthermore, there has recently been great success in using the FFTLog decomposition technique to significantly speed up the computation of higher-order statistics without the Limber approximation (Assassi et al. 2017; Lee & Dvorkin 2020).

3.5.2 The Post-Limber Lensing Bias Corrections

Figure 3.4 shows the impact of relaxing the Limber approximation on the combined corrections to the cosmic shear angular power spectra for the reduced shear approximation and magnification bias. Now, it can be seen that the magnitude of these corrections is over-estimated slightly throughout the entire probed range when the Limber approximation is made. This is due to the fact that the mathematical forms of these corrections, Equation (2.3) and Equation (2.11), involve integrating over two of the sides of the bispectrum triangle.

Accordingly, mode-mixing results in bispectra with at least one ℓ-mode less than 60 being involved in corrections for all ℓ values. One also sees that, once again, the over-estimation is worse for the higher redshift bins. This is expected, given that these trends are carried across from the bins' respective bispectra. The correction terms themselves are highest at higher redshift; meaning that they are the dominant contribution to the induced cosmological biases (see Figures 2.1, 2.2, and 2.3).

In fact, for all bins, the difference between the Limber approximated and post-Limber cases is below sample variance, as seen in Figure 3.5. The worst-case scenario cosmological parameter biases, when $\Delta C_{\ell;ij} \approx 0.01\, C^{\gamma\gamma}_{\ell;ij}$, are stated in Table 3.1. Also reproduced here, from Chapter 2, are the biases if the reduced shear and magnification bias corrections are neglected entirely.

The bias on a parameter is considered significant when it exceeds 0.25σ, as

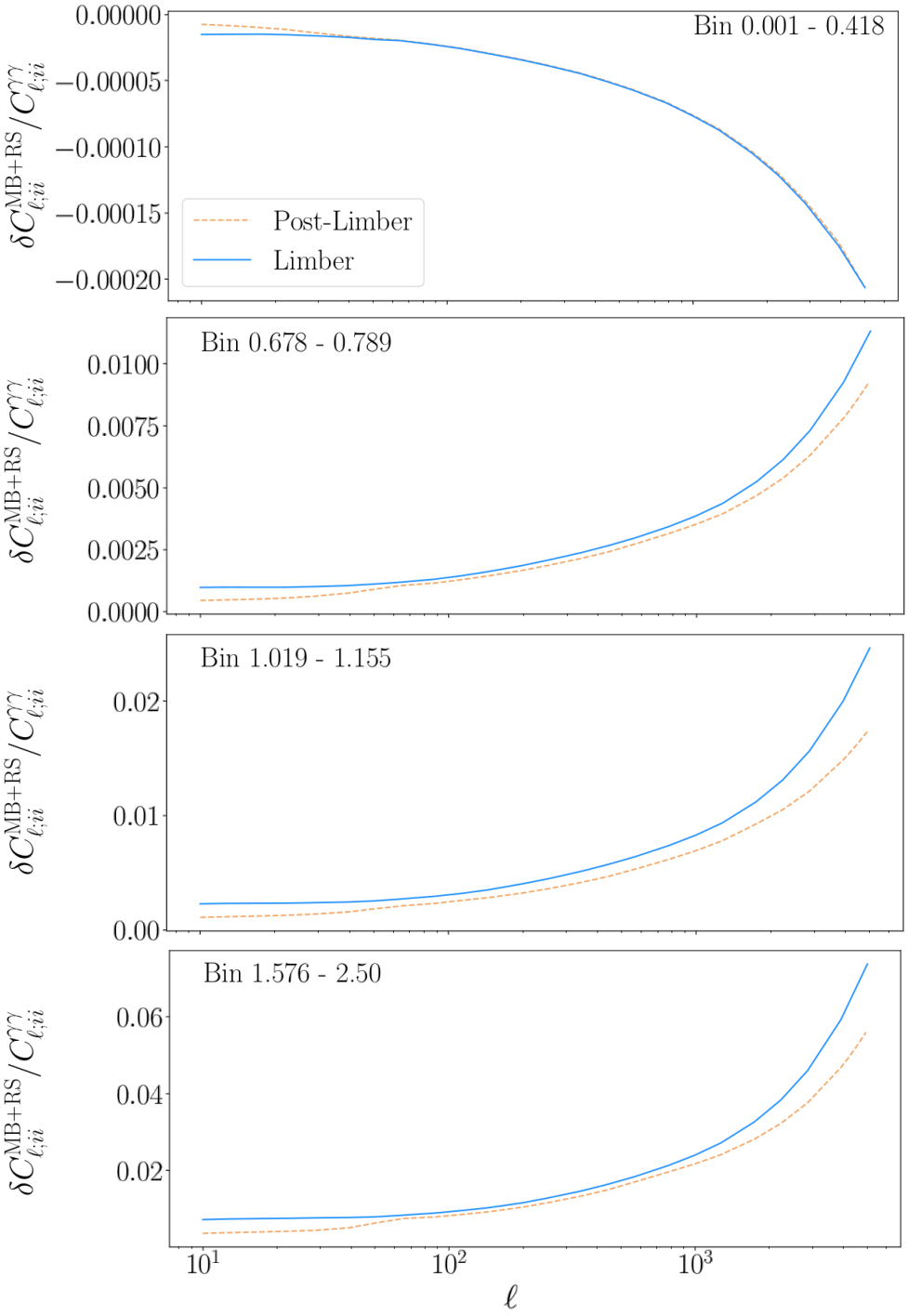

Figure 3.4: Combined reduced shear and magnification bias corrections, with and without the Limber approximation. Corrections for the auto-correlation of four bins across the redshift range of a *Euclid*-like survey, 0 – 2.5. Now, due to mode-mixing, the Limber approximation overestimates the correction terms at all ℓ-modes. As with the convergence bispectra, the over-prediction worsens at higher redshift. Adapted from Deshpande & Kitching (2020).

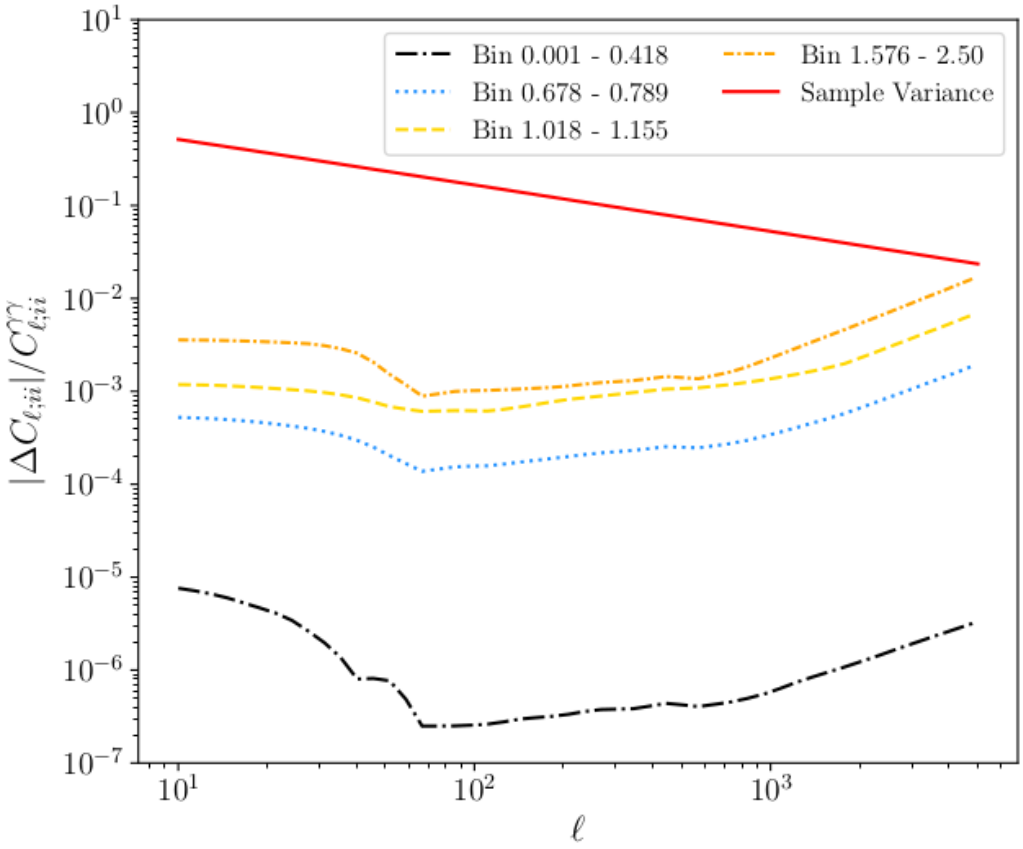

Figure 3.5: Difference between Limber and post-Limber reduced shear and magnification bias corrections, relative to the auto-correlation power spectrum for four bins in redshift range $0-2.5$. The sample variance of the galaxy survey is also shown for comparison. The overestimation of the Limber approximation worsens at higher redshifts. However, it is below sample variance across the probed redshift range; meaning that the Limber approximation is sufficient when calculating these correction terms for Stage IV experiments. Adapted from Deshpande & Kitching (2020).

at this point the confidence contours of the parameters with and without the systematic effect overlap less than 90% (Massey et al. 2013). From Table 3.1, I note that none of the biases are significant. In fact, all but one of the biases have a magnitude less than 0.20σ which means that the confidence regions of those parameters when having neglected the bias have an overlap of more than 95% with the parameters' confidence regions when the bias is taken into account.

I note that the bias in the inferred value of w_a sits on the threshold of

Table 3.1: Worst-case scenario biases in w_0w_aCDM cosmological parameters from the difference in the post-Limber and Limber approximated (labelled 'PL-L') reduced shear and magnification bias corrections, relative to the predicted 1σ uncertainty on those parameters (Euclid Collaboration: Blanchard et al. 2020) for a *Euclid*-like survey. The biases resulting from neglecting the reduced shear and magnification bias corrections altogether are also reproduced from Chapter 2, in the column labelled 'AD19'. Adapted from Deshpande & Kitching (2020).

Cosmological Parameter	Worst-case PL-L Bias/σ	AD19 Bias/σ
$\Omega_{\rm m}$	0.073	-0.53
$\Omega_{\rm b}$	0.065	-0.20
h	0.090	0.040
$n_{\rm s}$	-0.16	-0.34
σ_8	-0.020	0.43
$\Omega_{\rm DE}$	0.13	1.36
w_0	-0.18	-0.68
w_a	0.25	1.21

significance. However, for $\ell \lesssim 5000$ and all bin correlations other than the auto-correlation of bin $1.576-2.50$, $\Delta C_{\ell;ij} < 0.01\, C^{\gamma\gamma}_{\ell;ij}$. Given that these modes and bins will make up the majority of observations for a *Euclid*-like survey, one can safely conclude that the cosmological biases induced from neglecting the reduced shear and magnification bias corrections will not be significantly altered by whether they make the Limber approximation or not.

Furthermore, biases from the difference between the post-Limber and Limber approximated corrections are significantly smaller in magnitude than those resulting from simply neglecting the Limber approximated corrections entirely. Accordingly, these correction terms can be safely calculated under the Limber approximation for Stage IV experiments.

3.6 Summary and Outlook

Within this chapter, I have considered how the Limber approximation will affect the convergence bispectrum calculated for Stage IV weak lensing experiments. Additionally, I also calculated the resulting impact on the reduced

shear and magnification bias corrections to the cosmic shear angular power spectrum, as these quantities depend on the bispectrum. I found that the Limber approximation significantly over-predicts the bispectrum at ℓ-modes below 60, throughout the redshift range of a *Euclid*-like survey.

Furthermore, I found that this discrepancy worsens at higher redshifts and lower ℓ scales. Accordingly, I found that the reduced shear and magnification bias corrections are also over-estimated by the Limber approximation, although the difference is well below the sample variance of a Stage IV weak lensing experiment. Finally, I calculated the worst-case scenario cosmological parameter biases that result from the difference between the post-Limber and Limber approximated corrections. These were found not to be significant. Hence, I conclude that the Limber approximation is sufficient for these terms, at this level of precision.

Chapter 4
Doppler-shifted Weak Lensing

This chapter adapts Deshpande & Kitching (2021).

The focus of this chapter is another commonly neglected effect that modifies the expression for the observed reduced shear. Specifically, this chapter describes the impact of the Doppler-shift of the measured source comoving distances, on the cosmology performed by a *Euclid*-like survey. The code used in this investigation was made publicly available.[1]

4.1 Motivation and Outline

The change in the observed shape of distant galaxies due to weak gravitational lensing by the LSS, known as cosmic shear, is a powerful tool for performing precision cosmology. It is a particularly strong probe of dark energy (Albrecht et al. 2006). Existing cosmic shear surveys are able to carry out cosmology competitive with modern CMB surveys. The advent of Stage IV weak lensing surveys will mean more than an order-of-magnitude increase in precision over the present generation of surveys.

In order to match this increased precision in the data, we must ensure that our theoretical analyses are sufficiently accurate. Accordingly, the impact of neglecting higher–order systematic effects on Stage IV experiments must be explicitly evaluated. In this chapter, I use the Fisher matrix formalism to

[1] `https://github.com/desh1701/k-cut_reduced_shear`

predict the cosmological parameter biases from a *Euclid*-like survey, when one such effect is neglected: the Doppler-shift of measured source redshifts due to their peculiar velocities and the inhomogeniety of the Universe. While the theoretical formalism for this effect has been formulated (as a second-order correction to the shear; Bernardeau et al. 2010; Cuesta-Lazaro et al. 2018), its impact at the angular power spectrum level, on IAs, on cosmological parameter inference for the specifications of a *Euclid*-like survey, and under the Limber approximation, has not been explicitly evaluated.

This chapter is organised in the following manner: Section 4.2 details how the reduced shear approximation is modified by the presence of Doppler-shift, and how this results in another three-point correction term to any computed two-point statistics. Then, in Section 4.3, I detail how the Limber approximation must also be modified when quantities related to this Doppler-shift are computed. Following on, I describe the corrections to the modelled shear angular power spectra that result from the Doppler-shift, in Section 4.4. Next, the modelling specifications followed in this investigation are given in Section 4.5. The impact of making these corrections for a *Euclid*-like survey is then explicitly reported and discussed in Section 4.6. Lastly, I summarise the conclusions of the chapter in Section 4.7.

4.2 Doppler-shifted Cosmic Shear

When measuring the effect of weak lensing on a given source galaxy, one observes its redshift. However, the inhomogeneity of the Universe and the presence of the LSS mean that the source will have a peculiar velocity towards its local overdensity. Consequently, the measured redshift will be perturbed by Doppler-shift. At second-order, this will result in a correction to the observed reduced shear due to the coupling between this redshift perturbation and the lenses. Under the reduced shear approximation, this is given by (Bernardeau

et al. 2010):

$$g^{\alpha}(\boldsymbol{\theta}, \chi) = \gamma^{\alpha}(\boldsymbol{\theta}, \chi) + \delta g_z(\boldsymbol{\theta}, \chi), \tag{4.1}$$

where δg_z accounts for the perturbation of the observed redshift according to:

$$\delta g_z(\boldsymbol{\theta}, \chi) = -\frac{\mathrm{d}\gamma^{\alpha}}{\mathrm{d}\chi}\frac{\mathrm{d}\chi}{\mathrm{d}z}\delta z. \tag{4.2}$$

Now, δz is the perturbation of the source redshift due to Doppler-shift. Expanding this expression explicitly, and neglecting the sub-dominant Sachs-Wolfe and integrated Sachs-Wolfe effects results in:

$$\delta g_z(\boldsymbol{\theta}, \chi) = \frac{c}{\chi^2 H(\chi) a(\chi)}\, \boldsymbol{n}\cdot\boldsymbol{v} \int_0^{\chi} \mathrm{d}\chi\, \partial^2\Phi(\boldsymbol{\theta}, \chi), \tag{4.3}$$

where $H(\chi)$ is the value of the Hubble function at source comoving distance χ, $\boldsymbol{n}$ is the unit direction vector pointing from the source to the observer, $\boldsymbol{v}$ is the peculiar velocity of the source, and Φ is the gravitational potential. In fact, δg_z is a two-point term, as $\boldsymbol{n}\cdot\boldsymbol{v}$ also depends on the matter density contrast (see e.g. Appendix B of Bacon et al. 2014). Accordingly, I write Equation (4.3) as a combination of κ^{like} and γ^{like} terms:

$$\delta g_z(\boldsymbol{\theta}, \chi) = \kappa^{\mathrm{like}}(\boldsymbol{\theta}, \chi)\, \gamma^{\mathrm{like}}(\boldsymbol{\theta}, \chi), \tag{4.4}$$

within which:

$$\kappa^{\mathrm{like}}(\boldsymbol{\theta}, \chi) = \frac{c}{\chi^2 H(\chi) a(\chi)}\, \boldsymbol{n}\cdot\boldsymbol{v}, \tag{4.5}$$

$$\gamma^{\mathrm{like}}(\boldsymbol{\theta}, \chi) = \int_0^{\chi} \mathrm{d}\chi\, \partial^2\Phi(\boldsymbol{\theta}, \chi). \tag{4.6}$$

The Doppler correction is now expressed as a product between a shear-like term, γ^{like}, and a convergence-like term, κ^{like}, analogous to the way in which other three-point correction terms (e.g. the reduced shear and magnification

bias corrections) are typically formulated.

When expanded fully, in spherical harmonic space, and for a given tomographic redshift bin i, these terms take the form:

$$\widetilde{\kappa}^{\rm like}_{i;\ell m} = 4\pi i^{\ell} c \int_0^{\chi_{\rm lim}} \frac{{\rm d}\chi}{\chi^2 H(\chi) a(\chi)} n_i(\chi) \int_0^{\infty} \frac{d^3k}{(2\pi)^3} \frac{j'_{\ell}(k\chi)}{k} \, {}_2Y^*_{\ell m}(\hat{\boldsymbol{k}}) \widetilde{\delta}(\boldsymbol{k}, \chi), \tag{4.7}$$

$$\widetilde{\gamma}^{\rm like}_{i;\ell m} = 4\pi i^{\ell} \frac{3\Omega_{\rm m} H_0^2}{2c^2} \int_0^{\chi_{\rm lim}} {\rm d}\chi n_i(\chi) \int_0^{\infty} \frac{d^3k}{(2\pi)^3} \, j_{\ell}(k\chi) \, {}_2Y^*_{\ell m}(\hat{\boldsymbol{k}}) \widetilde{\delta}(\boldsymbol{k}, \chi), \tag{4.8}$$

where j'_{ℓ} is the derivative of the spherical-Bessel function j_{ℓ} with respect to $k\chi$.

Propagating Equation (4.4) through to the computation of the E-mode angular power spectra of Equation (1.85) leads to a three-point correction for the Doppler-shift. However, applying the Limber approximation as part of this process poses a unique challenge.

4.3 Adapting the Limber Approximation

While the extended Limber approximation (LoVerde & Afshordi 2008) can be readily applied to the $\widetilde{\gamma}^{\rm like}_{i;\ell m}$ Doppler term of Equation (4.8), the $\widetilde{\kappa}^{\rm like}_{i;\ell m}$ term from Equation (4.7) presents complications. This is due to the additional factor of k, and the presence of the derivative of a spherical Bessel function.

In order to apply the Limber approximation for this case, I begin by recognizing that:

$$j'_{\ell}(k\chi) = \frac{\ell}{k\chi} j_{\ell}(k\chi) - j_{\ell+1}(k\chi). \tag{4.9}$$

Now, I follow the derivation of LoVerde & Afshordi (2008), referred to as LA for the remainder of this chapter, for an angular power spectrum where one of

the fields probed is $\widetilde{\kappa}^{\rm like}_{i;\ell m}$. Here I only detail the two-point case for simplicity and brevity, however it is straightforward to generalise this to the three-point case; particularly given that a bispectrum can typically be expressed as a linear combination of power spectra (Fry 1984; Scoccimarro & Couchman 2001; Gil-Marín et al. 2012; Takahashi et al. 2020). Equation (5) of LA, for this scenario, would then read:

$$C_{A\kappa^{\rm like}} = \int {\rm d}k P_{A\delta} \int {\rm d}\chi_1 \frac{F_A}{\sqrt{\chi_1}} J_{\ell+1/2}(k\chi_1) \int {\rm d}\chi_2 \frac{F_{\kappa^{\rm like}}}{\sqrt{\chi_2}} \times \left[\frac{\ell}{k\chi} J_{\ell+1/2}(k\chi_2) - J_{\ell+3/2}(k\chi_2) \right], \tag{4.10}$$

where J_ℓ is the Bessel function of the ℓ-th order, F_A is the projection kernel for field A, and:

$$F_{\kappa^{\rm like}}(\chi) = \frac{c}{\chi^2 H(\chi) a(\chi)} n(\chi). \tag{4.11}$$

Now, following LA through to their Equation (13), I obtain:

$$\begin{aligned} C_{A\kappa^{\rm like}} &= \int \frac{{\rm d}\chi}{\chi^2} \frac{\chi}{(\ell+1/2)} \left[\frac{\ell}{(\ell+1/2)} - \frac{(\ell+1/2)}{(\ell+3/2)} \right] \\ &\quad \times F_{\kappa^{\rm like}}(\chi) F_A(\chi) P_{A\delta} \left(\frac{(\ell+1/2)}{\chi} \right) \\ &= \int \frac{{\rm d}\chi}{\chi^2} W_i^{\kappa\nu}(\chi, \ell) F_A(\chi) P_{A\delta} \left(\frac{(\ell+1/2)}{\chi} \right), \end{aligned} \tag{4.12}$$

where only terms to the first-order have been retained. When performed at the three-point level, this calculation allows for the computation of the necessary Limber approximated bispectra.

4.4 Corrections for Doppler-shift

Constructing an expression for the angular power spectrum which takes into account the additional Doppler correction term, under the flat-sky, flat-Universe,

and Limber approximations, recovers Equation (1.87), plus an additional term:

$$\delta C_{\ell;ij}^{\mathrm{Doppler}} = \int_0^\infty \frac{\mathrm{d}^2\boldsymbol{\ell'}}{(2\pi)^2} \cos(2\phi_{\ell'} - 2\phi_\ell) B_{ij}^{\mathrm{Doppler}}(\boldsymbol{\ell}, \boldsymbol{\ell'}, -\boldsymbol{\ell} - \boldsymbol{\ell'}), \tag{4.13}$$

where:

$$\begin{aligned} B_{ij}^{\mathrm{Doppler}}(\boldsymbol{\ell}, \boldsymbol{\ell'}, -\boldsymbol{\ell} - \boldsymbol{\ell'}) = \int_0^{\chi_{\mathrm{lim}}} \frac{\mathrm{d}\chi}{\chi^4} [&W_i^{\kappa\nu}(\chi, \ell') W_i^{\gamma\nu}(\chi) W_j(\chi) \\ &+ W_j^{\kappa\nu}(\chi, \ell') W_j^{\gamma\nu}(\chi) W_i(\chi)] \\ &\times B_{\delta\delta\delta}(\boldsymbol{k}, \boldsymbol{k'}, -\boldsymbol{k} - \boldsymbol{k'}, \chi) \end{aligned} \tag{4.14}$$

Here, $W_i^{\kappa\nu}$ and $W_i^{\gamma\nu}$ are weight functions, analogous to the lensing kernel of Equation (1.88), corresponding to $\widetilde{\kappa}_{i;\ell m}^{\mathrm{like}}$ and $\widetilde{\gamma}_{i;\ell m}^{\mathrm{like}}$, respectively. I define these weight functions as:

$$\begin{aligned} W_i^{\kappa\nu}(\chi, \ell) = &\left[\frac{\ell}{(\ell + 1/2)^2} - \frac{1}{(\ell + 3/2)}\right] \\ &\times \frac{c}{\chi\, H(\chi)\, a(\chi)}\, n_i(\chi), \end{aligned} \tag{4.15}$$

$$W_i^{\gamma\nu}(\chi) = \frac{3\Omega_{\mathrm{m}} H_0^2}{2c^2}\, n_i(\chi). \tag{4.16}$$

If one now also considers contributions from IAs, there will be another correction term to the angular power spectrum resulting from the correlation between the Doppler-shift and IA terms. This new term takes the form:

$$\begin{aligned} \delta C_{\ell;ij}^{\mathrm{Doppler-IA}} = &\int_0^\infty \frac{\mathrm{d}^2\boldsymbol{\ell'}}{(2\pi)^2} \cos(2\phi_{\ell'} - 2\phi_\ell) \\ &\times B_{ij}^{\nu\mathrm{I}}(\boldsymbol{\ell}, \boldsymbol{\ell'}, -\boldsymbol{\ell} - \boldsymbol{\ell'}), \end{aligned} \tag{4.17}$$

where now I define:

$$B_{ij}^{\nu\mathrm{I}}(\boldsymbol{\ell},\boldsymbol{\ell'},-\boldsymbol{\ell}-\boldsymbol{\ell'}) = \int_0^{\chi_{\lim}} \frac{\mathrm{d}\chi}{\chi^4}[W_i^{\kappa\nu}(\chi,\ell')W_i^{\gamma\nu}(\chi)\, n_j(\chi) + W_j^{\kappa\nu}(\chi,\ell')W_j^{\gamma\nu}(\chi)\, n_i(\chi)] \times B_{\delta\delta\mathrm{I}}(\boldsymbol{k},\boldsymbol{k'},-\boldsymbol{k}-\boldsymbol{k'},\chi). \tag{4.18}$$

4.5 Modelling Methodology

To model a *Euclid*-like survey, I used the specifications detailed in Section 1.3.2. Additionally, as with the previous chapters, the fiducial cosmology and IA parameters selected in Section 1.3.3 were used, to facilitate self-consistent comparisons.

Furthermore, in this chapter, I used the publicly available `CAMB`[2] cosmology software package (Lewis et al. 2000) to compute the matter power spectrum and growth factor. This has been shown to be consistent with the hitherto used `CLASS` package (Blas et al. 2011) meaning the results of this thesis are self-consistent. Once again, the non-linear part of the matter power spectrum was calculated using the `Halofit` paradigm (Takahashi et al. 2012), and the additional corrections of Mead et al. (2015). In order to calculate comoving distances, I additionally made use of the `Astropy` package[3] (Astropy Collaboration et al. 2013, 2018). Now, the matter bispectrum model of Scoccimarro & Couchman (2001) was replaced by the updated `BiHalofit` model of Takahashi et al. (2020). It was computed using the corresponding publicly available software package[4]. For a comparison of how this change in model affects three-point corrections, see Section 5.4.1.

With these tools and specifications, I first computed the Doppler-shift cor-

[2] `https://camb.info/`
[3] `http://www.astropy.org`
[4] `http://cosmo.phys.hirosaki-u.ac.jp/takahasi/codes_e.htm`

rections described by Equations (4.13) and (4.17). These were compared to the sample variance for a *Euclid*-like survey. Next, I propagated these corrections through the Fisher matrix formalism; estimating the cosmological parameter biases that would result from ignoring the Doppler-shift effect.

Additionally, as is the case in Chapter 3, the Fisher matrices used here assumed a Gaussian covariance; meaning that the SSC contribution was again neglected. This was again done in order to reduce computational load.

4.6 Results and Discussion

Within this section, I present the effect of neglecting Doppler-shift on the cosmology that will be carried out with a *Euclid*-like survey. Firstly, I show the magnitude of the Doppler and Doppler-IA corrections relative to the predicted cosmic shear power spectra for such a survey. I then report the resulting biases on the inferred cosmological parameters that would result from ignoring these corrections.

In Figure 4.1, I show the magnitude of the Doppler and Doppler-IA correction terms, relative to the cosmic shear angular power spectra, for the auto-correlation spectra of all tomographic bins for a *Euclid*-like survey. Here, the two corrections are shown both separately and when combined. Additionally, the sample variance, given by Equation (3.17), is also shown for reference.

From this graph, one sees that the impact of Doppler-shift decreases as the redshift of the tomographic bin probed increases. This is a consequence of the accelerating expansion of the Universe (Planck Collaboration et al. 2020), as accordingly one expects the relative Doppler-shift to be greater at lower redshifts. However, across the entire redshift and ℓ range of the survey, I observe that both correction terms remain several orders-of-magnitude below sample variance; consistent with the findings of (Cuesta-Lazaro et al. 2018). This suggests that these corrections may be able to be safely neglected for

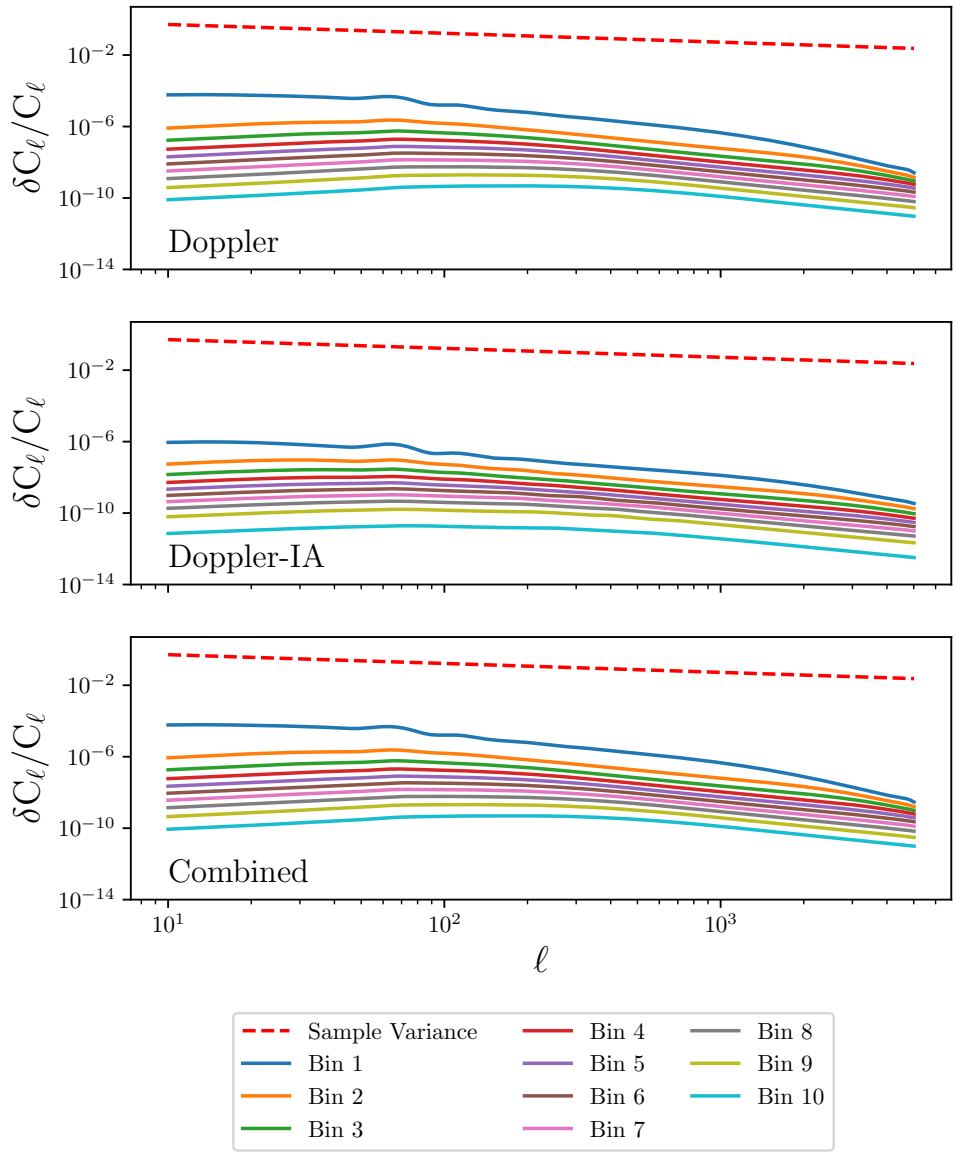

Figure 4.1: Relative magnitude of Doppler-shift corrections as a proportion of shear angular power spectra, for the auto-correlations of 10 equi-populated tomographic redshift bins for a *Euclid*-like survey. The bin edges are: {0.001, 0.418, 0.560, 0.678, 0.789, 0.900, 1.019, 1.155, 1.324, 1.576, 2.50}. The top panel shows the Doppler-shear correction, while the middle panel shows the Doppler-IA term, and the bottom panel displays the combined corrections. The sample variance is also shown, for comparison. As would be expected, the effect of Doppler-shift is greatest at low redshift, and decreases as redshift increases. In all cases, both corrections are several orders-of-magnitude below sample variance, suggesting these terms are unlikely to be significant for Stage IV surveys. Adapted from Deshpande & Kitching (2021).

Table 4.1: Predicted 1σ cosmological parameter constraints obtained from cosmic shear power spectra for a *Euclid*-like survey, together with the biases in the inferred parameter values resulting from neglecting the Doppler-shift correction. Constraints and biases are obtained using the Fisher matrix formalism, and the choice of fiducial cosmology is stated in Table 1.2. Biases are only considered significant if they exceed 0.25σ, as at this point the 2σ parameter constraints would overlap by less than 90%. All biases reported here are well below that threshold, suggesting these corrections can be safely neglected for Stage IV experiments. Adapted from Deshpande & Kitching (2021).

Cosmological Parameter	Uncertainty (1σ)	Doppler Bias/1σ	Doppler-IA Bias/1σ
$\Omega_{\rm m}$	0.0089	1.4×10^{-3}	3.4×10^{-6}
$\Omega_{\rm b}$	0.020	-1.8×10^{-4}	-4.0×10^{-7}
h	0.12	-2.8×10^{-4}	-1.2×10^{-6}
$n_{\rm s}$	0.028	-1.3×10^{-4}	5.2×10^{-7}
σ_8	0.0094	-1.1×10^{-3}	-2.6×10^{-6}
w_0	0.11	1.2×10^{-3}	2.9×10^{-6}
w_a	0.32	-5.6×10^{-4}	-1.9×10^{-6}

upcoming surveys.

To provide more in-depth insight into whether these terms can be neglected for Stage IV surveys, Table 4.1 shows the biases that would result in the inferred cosmological parameter values, if the two Doppler-shift effects were to be neglected. Also shown here are the predicted parameter constraints for a *Euclid*-like survey. Both the predicted constraints and biases were calculated using the Fisher formalism. From this table, one sees that all of the resulting biases are at sub-percent level. Given that a bias must exceed 0.25σ, in order to typically be considered significant – as at this point the biased and unbiased parameter constraints would overlap by less than 90% – one can safely conclude that these effects can be neglected for Stage IV experiments.

4.7 Summary and Outlook

Within this chapter, I have explored the impact of Doppler-shift on Stage IV cosmic shear surveys. Adopting modelling specifics for a *Euclid*-like survey, I calculated the three-point corrections to the shear angular power spectra that

result from the perturbation of the observed shear by Doppler-shift. Additionally, I demonstrated how this perturbation interacts with IA terms, and calculated the resulting Doppler-IA correction for the shear angular power spectrum. Both of these additional corrections were shown to be several orders-of-magnitude smaller than sample variance, suggesting these corrections could be safely neglected.

In order to explicitly check whether these corrections resulted in any significant biases at the cosmological parameter level, I propagated these through a Fisher matrix calculation. I found that all resulting biases were of the sub-percent level, confirming that, in isolation, Doppler-shift does not need to be taken into account for cosmic shear analyses in Stage IV weak lensing surveys.

However, I note that it is possible that when combined with multiple other neglected approximations, the total magnitude of the corrections may result in significant biases. A comprehensive investigation of *all* weak lensing approximations is necessary to test this. Additionally, while this effect does not significantly affect the cosmic shear power spectrum, it can be detected in other forms in Stage IV surveys. If the convergence is directly probed, a significant contribution to the observed convergence signal from this Doppler-shift can be detected (Bacon et al. 2014). Furthermore, this Doppler-shift of source redshifts could also result in detectable contributions in cross-correlations with other probes that depend on the peculiar velocity of overdensities, for example the Kinematic Sunyaev–Zeldovich effect (see e.g. Shao et al. 2011; Sugiyama et al. 2017).

Chapter 5

Mitigating Biases with k-cut Cosmic Shear

This chapter adapts Deshpande et al. (2020b).

One of the major challenges identified by the preceding chapters is the computational complexity of computing three-point correction terms to the commonly observed two-point statistics of cosmic shear. The k-cut method – making the Bernardeau-Nishimichi-Taruya transform, and then applying a redshift-dependent ℓ-cut – can reduce sensitivity to baryonic physics; allowing Stage IV surveys to include information from increasingly higher ℓ-modes. This chapter addresses the question of whether it can also mitigate the impact of making the reduced shear approximation; which is also important in the high-κ, small-scale regime. The following investigation focuses primarily on a *Euclid*-like survey as a representation of a typical Stage IV weak lensing survey, but also considers a Stage III kinematic weak lensing survey. I have also made the key parts of code utilised for this analysis publicly available[1].

5.1 Motivation and Outline

As a result of the improvement in precision that Stage IV weak lensing surveys will deliver over existing experiments, we face new challenges. One such issue is the small scale sensitivity problem. This refers to the fact that the cosmic shear

[1] `https://github.com/desh1701/k-cut_reduced_shear`

signal is sensitive to poorly understood physics at scales below $k = 7\,h\mathrm{Mpc}^{-1}$ (Taylor et al. 2018b). Nulling has previously been suggested as a potential solution (Huterer & White 2005). An approach that has shown promise in addressing this issue is to first apply the Bernardeau-Nishimichi-Taruya (BNT) nulling scheme (Bernardeau et al. 2014), and then take a redshift-dependent angular scale cut. This technique is known as k-cut cosmic shear (Taylor et al. 2018a).

Using k-cut shear to alleviate the small scale sensitivity problem, we can push our analyses to include increasingly smaller angular scales. For example, an appropriate k-cut would allow us to readily achieve the 'optimistic' case for a *Euclid*-like survey; where e.g. the inclusion of angular wave numbers of up to $\ell = 5000$ would be attainable. However, at these scales, two theoretical assumptions cease to be valid; the reduced shear approximation, and the assumption that magnification bias can be neglected (see Chapter 2). Relaxing these requires the explicit calculation of the convergence bispectrum, which could be prohibitively computationally expensive for Stage IV experiments and requires a theoretical expression for the poorly understood matter bispectrum, including baryonic feedback.

In this chapter, I demonstrate how the k-cut method preserves the reduced shear approximation for a Stage IV survey even at high-ℓ, as an example of how the k-cut technique could help forego the need to explicitly evaluate higher-order corrections. Specifically, I examine the case of a *Euclid*-like experiment, as forecasting specifications for such a survey are readily available (Euclid Collaboration: Blanchard et al. 2020). This procedure bypasses the need for the expensive computation of three-point terms, at the price of weakening cosmological parameter constraints. I also repeat this analysis for a hypothetical Tully-Fisher kinematic weak lensing survey (Huff et al. 2013; Gurri et al. 2020). Kinematic lensing has been proposed as a method to reduce shape noise

in weak lensing by an order of magnitude. It is predicated on spectroscopic measurements of disk galaxy rotation, and use of the Tully-Fisher relation in order to control for the intrinsic orientations of galaxy disks. For a detailed overview of kinematic weak lensing, see Huff et al. (2013). By also considering the kinematic survey set-up, I demonstrate that the reduced shear approximation (and therefore other similar systematic effects) will remain a problem for this other configuration of surveys, and that k-cut cosmic shear can help mitigate these effects here too.

I continue this chapter by describing the theoretical formalism behind k-cut cosmic shear in Section 5.2. Then, in Section 5.3, I review the modelling specifics used in this investigation. Section 5.4 then presents the key findings of this chapter. The last section of this chapter, Section 5.5, contains a summary of the investigation, as well as a discussion of future prospects.

5.2 k-cut Cosmic Shear

Given that the shear angular power spectrum is a projection of the matter power spectrum, to remove sensitivity to physical scales below a certain k-mode one must remove angular scales above the corresponding ℓ-mode. One may imagine that, in the regime of the Limber approximation, this could simply involve removing information where $\ell > k\chi$. However, in reality lensing kernels are broad; meaning that lenses across a range of distances and scales contribute power to the same ℓ-mode. Consequently, simply removing scales is not effective on its own (Taylor et al. 2018b).

A solution comes in the form of the BNT nulling scheme (Bernardeau et al. 2014). In this formalism, the observed tomographic angular power spectrum can be re-weighted in such a way that each redshift bin retains only the information about lenses within a small redshift range. This procedure can be illustrated by first considering three discrete source planes. Then, the BNT

weighted convergence, assuming flatness, can be written as:

$$\kappa^{\rm BNT} = \frac{3\Omega_m H_0^2}{2c^2} \int_0^{\chi_\beta} {\rm d}r \frac{\delta(\chi)}{a(\chi)} w(\chi), \tag{5.1}$$

where χ_β is the comoving distance to source plane i, and:

$$w(\chi) = \sum_{\beta, \chi_\beta > \chi} p_\beta \frac{\chi_\beta - \chi}{\chi_\beta}, \tag{5.2}$$

where p_β are the weights for planes $\beta = \{1, 2, 3\}$ with $\chi_1 < \chi_2 < \chi_3$, for the three bin case. In the BNT scheme, weights are then chosen such that $w(\chi < \chi_1) = 0$. This coupled with the fact that lenses with $\chi > \chi_3$ will not contribute to the re-weighted convergence, means that $\kappa^{\rm BNT}$ will only be sensitive to lenses with comoving distances in the range $\chi_1 \leq \chi < \chi_3$. This argument can be generalized (Taylor et al. 2021) for an arbitrary number of continuous source bins; leading to the construction of a weighting matrix, $\boldsymbol{M}$, that is applied to the observed angular spectra:

$$\boldsymbol{C}_\ell^{\rm BNT} = \boldsymbol{M} \boldsymbol{C}_\ell \boldsymbol{M}^T, \tag{5.3}$$

where $\boldsymbol{C}_\ell$ is a matrix of the $C_{\ell;ij}$ for all tomographic bin combinations, at the given ℓ-mode, and $\boldsymbol{C}_\ell^{\rm BNT}$ is its BNT-nulled counterpart. For a given k-cut, I remove information where $\ell > k_{\rm cut} \chi_i^{\rm mean}$ from the BNT-nulled power spectrum of bin i. Here, I use the mean comoving distance of the bin rather than the minimum distance to the bin, to avoid removing the first bin entirely. This has negligible impact on sensitivity to small scales (Taylor et al. 2018a).

5.3 Modelling Methodology

In order to examine whether k-cut cosmic shear can be used to minimise the impact of the reduced shear approximation on Stage IV surveys, I adopted

the forecasting specifications described in Section 1.3.2. The k-cut technique enables the inclusion of information from smaller angular scales, making the 'optimistic' scenario for such a survey, where ℓ-modes up to 5000 are studied, more achievable. Accordingly, I computed the reduced shear correction, and carried out the corresponding k-cut analysis, up to this maximum ℓ.

This process consisted of computing the predicted cosmological parameter uncertainties using the Fisher matrix formalism described in Section 1.3.1, and then computing the reduced shear correction and calculating the resulting biases. Next, I applied the BNT transform, and applied gradually lower k-cuts, monitoring the change in the parameter uncertainties and biases. I then noted the optimum k-cut that suppresses biases to below the significance threshold, without significantly compromising parameter constraints. This was also compared to the predicted cosmological parameter uncertainties from the 'pessimistic' case for such an experiment where only ℓ-modes up to 1500 are included, and no k-cut is necessary (Euclid Collaboration: Blanchard et al. 2020).

This process was repeated for a theoretical kinematic weak lensing survey. Here, I studied the effect of k-cut cosmic shear on the hypothetical TF-Stage III survey described in Huff et al. (2013). This survey includes ℓ-modes up to 5000, has $f_{\rm sky} = 0.12$, with an intrinsic ellipticity of $\sigma_\epsilon = 0.021$, and a surface density of galaxies of $\bar{n}_{\rm g} = 1.1$ arcmin^{-2}. I considered the survey to have ten equi-populated redshift bins with limits: $\{0.001,\ 0.568,\ 0.654,\ 0.723,\ 0.788,\ 0.851,\ 0.921,\ 0.999,\ 1.097,\ 1.243,\ 1.68\}$. A kinematic survey will not have IA contributions. The galaxy distribution for such a survey is modelled by:

$$\mathcal{N}_i(z) \propto z^\alpha e^{-\left(\frac{z}{z_0}\right)^\beta}, \tag{5.4}$$

with $\alpha = 29.98$, $z_0 = 1.10 \times 10^{-6}$, and $\beta = 0.33$.

For all computations in this chapter, I used the choice of cosmology specified in Section 1.3.3, with one key difference. In this investigation, I considered a flat w_0w_aCDM cosmology, so that $\Omega_{\rm DE}$ was also kept fixed and not treated as an inferred parameter. Given the strong constraints on flatness provided by contemporary cosmological surveys (Planck Collaboration et al. 2020), this does not compromise the validity of my findings. Additionally, as in Chapters 3 and 4, the Fisher matrices assumed a Gaussian covariance; neglecting the SSC contribution. The BNT matrices were calculated using the code[2] of Taylor et al. (2021). Additionally, to calculate the matter power spectrum, I again used the publicly available `CAMB` cosmology package, with `Halofit` and corrections from Mead et al. (2015) used to compute the non-linear contributions. Comoving distances were computed with `Astropy`.

Here, the matter bispectrum was computed again using the `BiHalofit` formalism and code. To verify that this would not significantly affect comparisons with previous chapters and works, I also performed a comparison of the reduced shear correction computed with the model of Scoccimarro & Couchman (2001), described by Equation (2.5) and denoted by 'SC', and the `BiHalofit` model, denoted by 'BH'.

5.4 Results and Discussion

In this section, I demonstrate the effect k-cut cosmic shear has on addressing the biases resulting from the reduced shear approximation, for a *Euclid*-like experiment and a hypothetical kinematic survey. I begin by comparing the cosmological parameter biases, for the standard calculation with no k-cut, found when the reduced shear approximation is relaxed with either the SC or BH bispectrum models. Next, the change in parameter constraints and biases for the BNT transformed power spectra with a range of k-cuts are shown; first for a *Euclid*-like survey, and then a kinematic lensing survey.

[2] `https://github.com/pltaylor16/x-cut`

Table 5.1: Cosmological parameter biases predicted if the reduced shear correction is neglected for two different matter bispectrum models. The SC model uses the fitting formulae of Scoccimarro & Couchman (2001), while BH is the `Bihalofit` model (Takahashi et al. 2020). The difference between the two approaches is also stated, and is not significant. Here σ denotes the 1σ uncertainty. Adapted from Deshpande et al. (2020b).

Cosmological Parameter	SC Model Bias/σ	BH Model Bias/σ	Absolute Difference in Biases/σ
$\Omega_{\rm m}$	-0.32	-0.28	0.04
$\Omega_{\rm b}$	-0.011	-0.0056	0.0044
h	0.025	0.027	0.002
$n_{\rm s}$	0.14	0.11	0.03
σ_8	0.27	0.24	0.03
w_0	-0.40	-0.33	0.07
w_a	0.28	0.23	0.05

5.4.1 Comparing Matter Bispectrum Models

The ratio of the reduced shear correction of Equation (2.3) calculated using the BH bispectrum, relative to the correction calculated using the SC bispectrum is shown in Figure 5.1. Here, the correction terms for the auto-correlation of four bins, with redshift-limits: 0.001 – 0.418, 0.678 – 0.789, 1.019 – 1.155, and 1.576 – 2.50, are shown in order to illustrate the difference between the two models. The consequent difference in the predicted parameter biases from using the two models is stated in Table 5.1.

From Figure 5.1, one sees that the two approaches produce correction terms that differ at most by 27%. At low-ℓ and at all but the highest redshifts, the BH model produces a correction smaller than the SC one. The BH correction then increases until the two models produce comparable results at $\ell \sim 100$. Beyond this ℓ-mode, the BH model once again produces a smaller correction value than the SC approach. For the highest redshift bins, the same trend persists. However, in this case the corrections start off being comparable, before the BH term becomes greater than the SC correction. After peaking at scales of $\ell \sim 100$, the BH correction reduces again. The greatest differences between

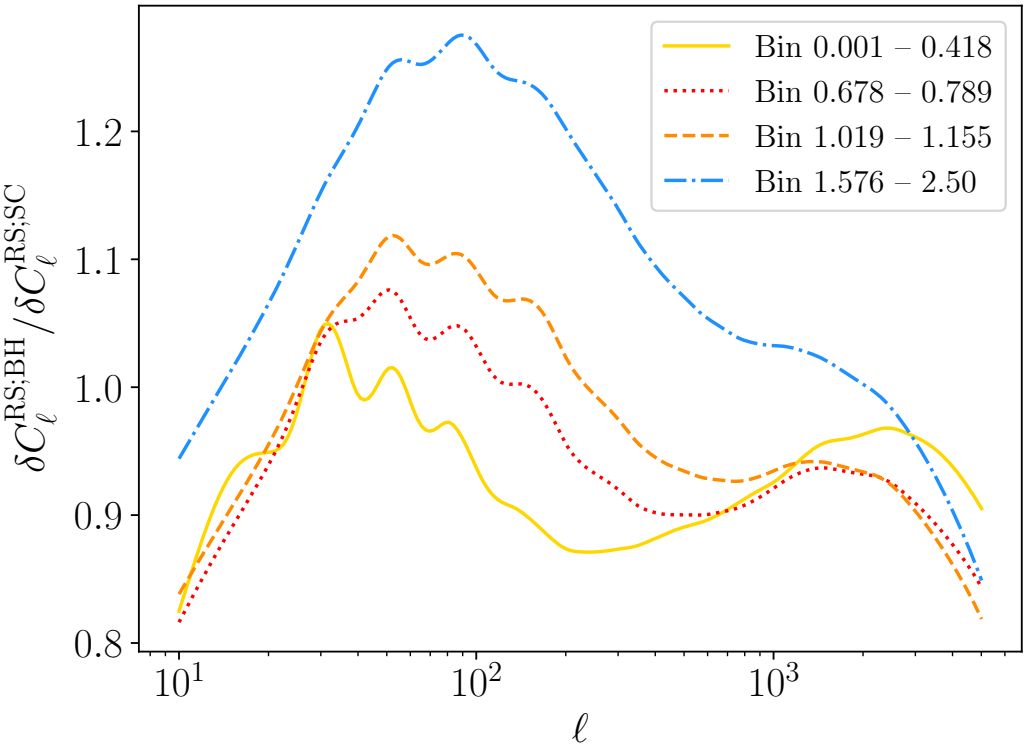

Figure 5.1: Ratio of reduced shear corrections calculated with two different matter bispectrum models. The first of these uses the approach of Scoccimarro & Couchman (2001) and is labelled by SC, whereas the second is the `BiHalofit` model (Takahashi et al. 2020) and is denoted by BH. The correction terms for four different auto-correlation spectra across the survey's anticipated redshift range are presented, and are representative of all the spectra. The most extreme disagreement between the models occurs at $\ell = 89$, where they disagree by 27%. I note that the reduced shear correction is negligible at these scales, and only becomes significant at scales above $\ell \sim 1000$ (see Chapter 2), at which point the two models are in closer agreement. Adapted from Deshpande et al. (2020b).

the two models occur at lower ℓ-modes, where the reduced shear correction is typically negligible (see Chapter 2). Additionally, these differences are likely to be dwarfed by baryonic model uncertainties.

Despite these differences, Table 5.1 shows that the resulting cosmological parameter biases from the two models are not significantly different. Accordingly, although the BH and SC models can differ significantly at calculating the matter bispectrum for certain scales and configurations (Takahashi et al.

2020), the reduced shear correction calculation can be considered robust to the choice of matter bispectrum model. For all results that follow, I use the BH matter bispectrum model.

5.4.2 k-cut for Stage IV Surveys

I calculated the cosmological parameter constraints, and the biases resulting from neglecting the reduced shear approximation, for a range of k-cut values. The changing constraints are shown in Figure 5.2, whilst the biases are shown in Figure 5.3. As expected, taking lower k-cuts results in weaker constraints. In general, biases reduce as a lower k-cut is taken. The behaviour of the bias in $\Omega_{\rm b}$ is non-trivial, due to the complex way in which this parameter interacts with the non-linear component of the matter power spectrum. A bias is considered significant if its magnitude is greater than 0.25σ, as beyond this the confidence contours of the biased and unbiased parameter estimates overlap by less than 90%. The maximum k-cut required in order to ensure that no parameter biases are significant is 5.37 hMpc^{-1}. Tables 5.2 and 5.3 show the constraints and biases at this k-cut respectively, as well as the constraints and biases when no k-cut is taken for both the 'optimistic' ($\ell_{\rm max}$=5000), and 'pessimistic' ($\ell_{\rm max}$=1500) scenarios for a *Euclid*-like survey. From this, I note that the optimum k-cut increases the size of all of the parameter constraints by less than 10%. This is a marked improvement over the 'pessimistic' case in which all but two of the parameters have their constraints increased by more than 10% compared to the 'optimistic' case.

These findings support the idea that k-cut cosmic shear can be successfully used to access smaller angular scales for upcoming Stage IV weak lensing surveys. It has already been shown that this technique can bypass the need to model baryonic physics (Taylor et al. 2018a), while allowing access to small physical scales. Now, these results indicate that k-cut cosmic shear can also address the impact of the reduced shear approximation. While explicit cal-

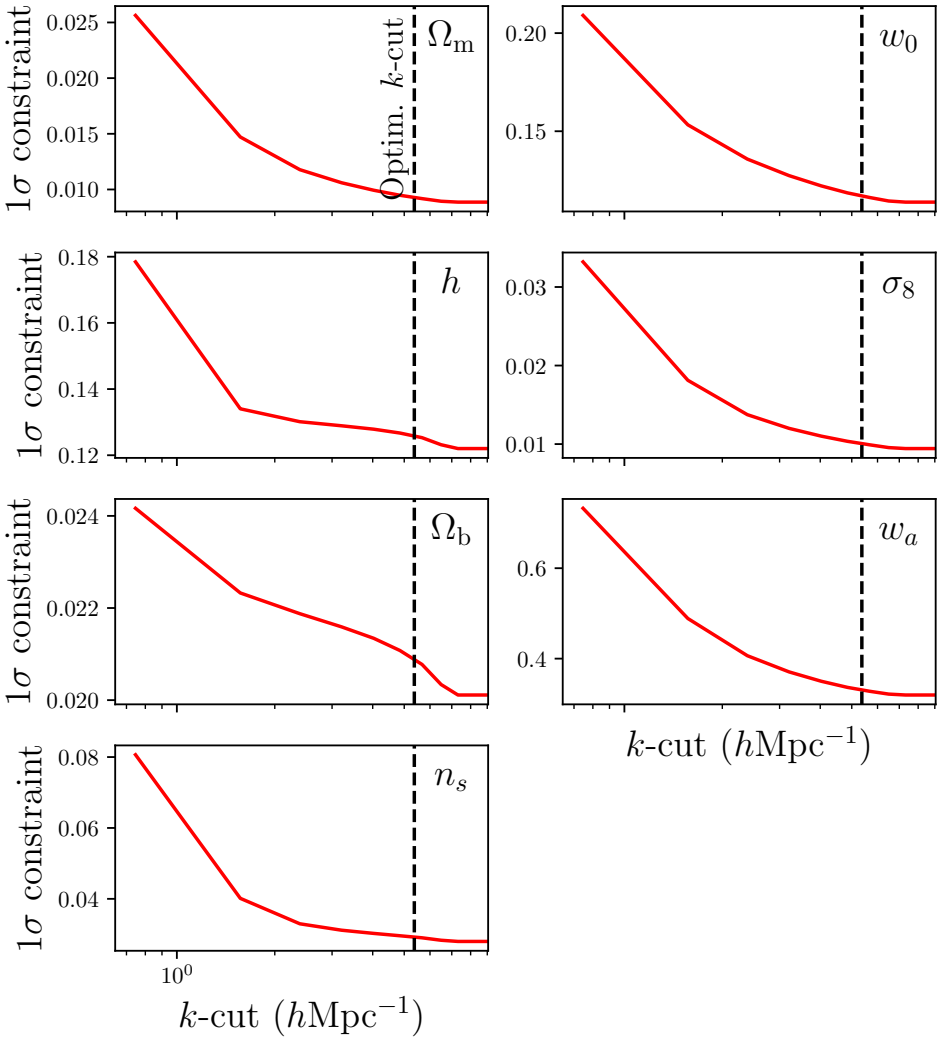

Figure 5.2: Change in the 1σ cosmological parameter constraints predicted for a *Euclid*-like survey, when a range of k-cuts are applied. These results are for the 'optimistic' case for such a survey, where ℓ-modes up to 5000 are included. Unsurprisingly, the constraints weaken as lower k-cuts are taken; corresponding to more information being removed. The black dashed line at $k = 5.37\,h\mathrm{Mpc}^{-1}$ marks the maximum k-cut required for biases from the reduced shear correction to not be significant. Adapted from Deshpande et al. (2020b).

culation of the reduced shear correction yields the most precise cosmological parameter constraints, it is prohibitively computationally expensive. The k-cut approach bypasses this cost while only marginally weakening the constraints.

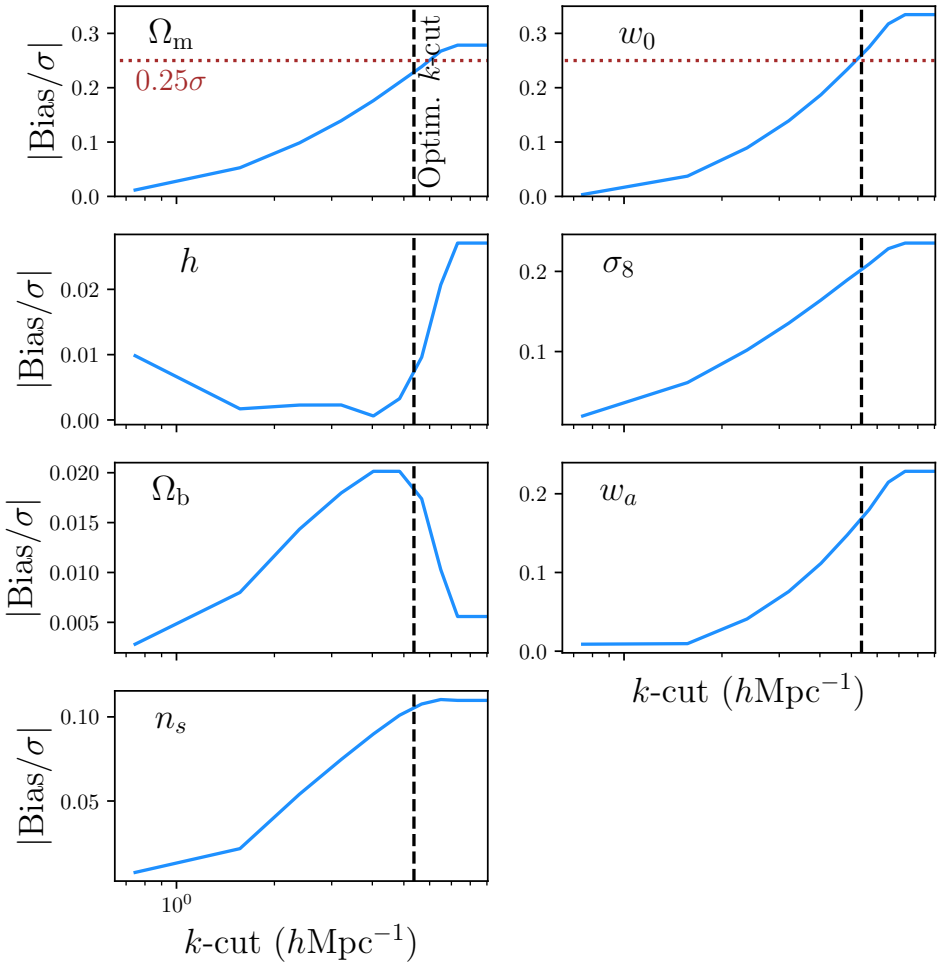

Figure 5.3: Change in cosmological parameter biases with changing k-cuts, when the reduced shear correction is neglected, for a *Euclid*-like survey. The values are reported as a fraction of the 1σ uncertainty of the respective parameter. A parameter is considered to be significantly biased if the bias is greater than 0.25σ. Beyond this point, the biased and unbiased confidence regions overlap less than 90%. These results are for the 'optimistic' case for a *Euclid*-like survey, where ℓ-modes up to 5000 are included. The black dashed line at $k = 5.37\,h\text{Mpc}^{-1}$ marks the maximum k-cut required for biases from the reduced shear correction to not be significant. The brown dotted line denotes the threshold for a bias to be significant. Generally, a lower k-cut corresponds to smaller biases, as sensitivity is reduced to regions where the reduced shear correction is largest. Adapted from Deshpande et al. (2020b).

I note that if the photometric redshifts are systematically mis-calibrated, the BNT transform I have computed would be inaccurate. In fact, given

Table 5.2: Predicted parameter uncertainties for a *Euclid*-like survey for three different cases. The 'optimistic' case is when ℓ-modes up to 5000 are included, and no k-cut is made, while the 'maximum k-cut' columns denote the situation where ℓ-modes up to 5000 are included, but a k-cut is taken at $k = 5.37$ $h\mathrm{Mpc}^{-1}$, as this is the maximum k-cut to achieve non-significant biases. Finally, the 'pessimistic' case is when only ℓ-modes up to 1500 are included, and no k-cut is taken. Adapted from Deshpande et al. (2020b).

Cosmological Parameter	Optimistic 1σ	Maximum k-cut 1σ	Pessimistic 1σ
Ω_m	0.0089	0.0094	0.013
Ω_b	0.020	0.021	0.022
h	0.12	0.13	0.13
n_s	0.028	0.029	0.035
σ_8	0.0094	0.010	0.015
w_0	0.11	0.12	0.14
w_a	0.32	0.33	0.44

that the lensing kernels have some width, using the peak of the kernel as a representative comoving distance value for the k-cut is already technically inaccurate. Despite this, the k-cut technique proves successful (Taylor et al. 2018a). Given that one would expect any biases in the photometric redshifts to be narrower than the width of the kernel, I do not anticipate that these biases would significantly affect the validity of the k-cut method. In addition, if there is no mis-calibration, the BNT transformed cross-spectra should be small, and dominated by shot-noise, which is well known and cosmology-independent. If there is significant photometric redshift calibration bias, these cross-spectra will no longer be small. Accordingly, the BNT transform can also serve as a null-test for mis-calibration.

Furthermore, another consideration is my choice of IA model. The NLA model used here can be overly restrictive, and artificially improve constraining power. This could lead to an overestimate of the biases, and accordingly the determination of a lower than needed k-cut. However, in any case the limiting k-cut value will be determined by baryonic physics modelling.

Table 5.3: Expected cosmological parameter biases from neglecting the reduced shear approximation, for a *Euclid*-like survey under three different scenarios. The 'optimistic' scenario is when ℓ-modes up to 5000 are included, and no k-cut is made. The 'maximum k-cut' case is when ℓ-modes up to 5000 are included, but a k-cut is taken at $k = 5.37\ h\mathrm{Mpc}^{-1}$; the maximum k-cut required to achieve non-significant biases. Lastly, the 'pessimistic' case is when only ℓ-modes up to 1500 are included, and no k-cut is taken. The 'maximum k-cut' option is able to suppress the biases to the point of not being significant, while still achieving more precise constraints than the 'pessimistic' option as seen in Table 5.2. Here σ denotes the 1σ uncertainty. Adapted from Deshpande et al. (2020b).

Cosmological Parameter	Optimistic Bias/σ	Maximum k-cut Bias/σ	Pessimistic Bias/σ
Ω_m	-0.28	-0.22	-0.076
Ω_b	-0.0056	-0.020	-0.012
h	0.027	0.0043	-0.001
n_s	0.11	0.10	0.040
σ_8	0.24	0.19	0.083
w_0	-0.33	-0.24	-0.064
w_a	0.23	0.15	0.024

5.4.3 k-cut for Kinematic Weak Lensing Surveys

The predicted cosmological parameter constraints for a hypothetical kinematic lensing survey which includes ℓ-modes up to 5000, together with the expected biases in those constraints from neglecting the reduced shear approximation, are stated in Tables 5.4 and 5.5, respectively. From this, one sees that the reduced shear correction is also necessary for potential future kinematic lensing surveys, as the bias in n_s is significant. This is due to the fact that constraint on n_s is improved, compared to the standard Stage IV case. The spectral index is most sensitive to high-ℓ modes (Copeland et al. 2018), and this is where the hypothetical kinematic survey performs better than the standard survey. The kinematic survey has a higher signal-to-noise ratio at high-ℓ, and a lower signal-to-noise ratio at low-ℓ, as the shot-noise is low by construction, and because it covers a smaller area than the Stage IV survey which means sample variance is relatively more important.

Table 5.4: Predicted cosmological parameter constraints for a TF-Stage III (Huff et al. 2013) kinematic lensing survey. Three different scenarios are presented here. The 'optimistic' scenario is when ℓ-modes up to 5000 are included, and no k-cut is made, while the 'maximum k-cut' columns denote the situation where ℓ-modes up to 5000 are included, but a k-cut is taken at $k = 5.82$ $h\mathrm{Mpc}^{-1}$, as this is the maximum k-cut to achieve non-significant biases. Finally, the 'pessimistic' case is when only ℓ-modes up to 1500 are included, and no k-cut is taken. Adapted from Deshpande et al. (2020b).

Cosmological Parameter	Optimistic 1σ	Maximum k-cut 1σ	Pessimistic 1σ
Ω_m	0.0083	0.0093	0.016
Ω_b	0.0089	0.0094	0.013
h	0.022	0.027	0.058
n_s	0.015	0.017	0.041
σ_8	0.031	0.032	0.047
w_0	0.17	0.19	0.33
w_a	0.59	0.68	1.18

For such a survey, I find that the maximum k-cut required for the biases from the reduced shear correction to no longer be significant is 5.82 $h\mathrm{Mpc}^{-1}$. This is higher than the value in the Stage IV survey case, because the kinematic survey is less deep in redshift. Consequently, the same ℓ-mode corresponds to a higher k-mode for the kinematic survey than in the Stage IV experiment case. Since the reduced shear correction is only non-negligible at the highest ℓ-modes, this is where a cut will alleviate biases, and shallower surveys can include higher k-modes before reaching this regime.

Tables 5.4 and 5.5 show the predicted parameter constraints and reduced shear biases at this k-cut, respectively. For comparison, the constraints and biases for the pessimistic case of the kinematic survey, where only ℓ-modes up to 1500 are probed, are also shown here. As with the Stage IV cosmic shear survey, the k-cut technique degrades the predicted cosmological constraints for a kinematic lensing survey less than the exclusion of ℓ-modes above 1500. With the k-cut, the largest increase is on the constraint on h, which increases by 27%. In comparison, in the pessimistic case, the lowest increase in constraints

Table 5.5: Predicted cosmological parameter biases from neglecting the reduced shear approximation for a TF-Stage III (Huff et al. 2013) kinematic lensing survey. Three different regimes are stated in this table. The 'optimistic' case when ℓ-modes up to 5000 are included, and no k-cut is made, the 'maximum k-cut' case where ℓ-modes up to 5000 are included, but a k-cut is taken at $k = 5.82\ h\mathrm{Mpc}^{-1}$, as this is the maximum k-cut to achieve non-significant biases, and the 'pessimistic' case is when only ℓ-modes up to 1500 are included, and no k-cut is taken. The 'maximum k-cut' option is able to suppress the biases to the point of not being significant, while still achieving more precise constraints than the 'pessimistic' option (as seen in Table 5.4). Here σ denotes the 1σ uncertainty. Adapted from Deshpande et al. (2020b).

Cosmological Parameter	Optimistic Bias/σ	Maximum k-cut Bias/σ	Pessimistic Bias/σ
Ω_m	-0.035	-0.032	-0.0056
Ω_b	0.079	0.068	0.022
h	-0.053	-0.0044	-0.00077
n_s	0.28	0.24	0.036
σ_8	0.083	0.082	0.017
w_0	0.059	0.046	0.024
w_a	-0.081	-0.064	-0.021

is of 44%, for Ω_b.

5.5 Summary and Outlook

In this chapter, I have examined the validity of the reduced shear approximation when applying the k-cut technique to Stage IV cosmic shear experiments, and a hypothetical kinematic lensing survey. I first compared the reduced shear correction calculated using two different models for the matter bispectrum: the fitting formulae of Scoccimarro & Couchman (2001), and the `BiHalofit` model. Despite the differences between the two approaches, I found that their resulting reduced shear corrections were not significantly different, and that accordingly the reduced shear correction was robust to the choice of bispectrum model.

The k-cut cosmic shear technique is used to remove sensitivity to baryonic physics, while allowing access to small physical scales. I examined whether it would also affect the impact of the reduced shear approximation. A variety of

k-cuts were applied to the BNT transformed theoretical shear power spectra and reduced shear corrections for the 'optimistic' case of a *Euclid*-like survey. This scenario assumes ℓ-modes up to 5000 are probed. I demonstrated that, in this case, k-cut cosmic shear preferentially removes scales sensitive to the reduced shear approximation, reducing its inaccuracy. This technique makes this 'optimistic' scenario more achievable, while bypassing the significant computational expense posed by having to explicitly calculate the reduced shear correction. The disadvantage is that the inferred cosmological parameter constraints are weakened. However, with k-cut cosmic shear applied to the 'optimistic' case, the parameter constraints are weakened significantly less than those found in the 'pessimistic' case for such a survey; where only ℓ-modes up to 1500 are included. I also repeated this analysis for a theoretical kinematic lensing survey; finding similarly that the k-cut technique reduced sensitivity to the reduced shear approximation.

Chapter 6
Conclusion

We stand on the precipice of a new generation of high-precision weak gravitational lensing cosmological surveys. Experiments such as *Euclid*, *Roman*, and Rubin will lead to more than an order-of-magnitude improvement in our ability to constrain the values of cosmological parameters. The primary focus of this thesis has been to ensure that the accuracy of our theoretical formalism for cosmic shear keeps up with this significant increase in precision. To accomplish this, I have primarily focused on a *Euclid*-like experiment.

First, I reviewed two commonly neglected systematic effects in current surveys: the impact of making the reduced shear approximation, and magnification bias. Accounting for these effects results in higher-order corrections to the cosmic shear angular power spectra, that depend on bispectra. I calculated these corrections and, using the Fisher matrix formalism, predicted the biases in $w_0 w_a$CDM cosmological parameters that would result from neglecting them. This revealed that not taking into account these terms would result in significant biases in all but two cosmological parameters for *Euclid*; making these corrections essential for Stage IV surveys. I also demonstrated how these systematic effects affect IA spectra as well, and showed that their effect on parameter inference is not significant.

I then examined the dependency of the corrections for the reduced shear approximation and magnification bias on another common theoretical assumption; the Limber approximation. The Limber approximation replaces spherical

Bessel functions with delta functions in order to simplify projection integrals in the calculation of the shear and convergence power spectra and bispectra. Whilst its impact has been shown to not be of concern at the power spectra level for Stage IV surveys, its impact on the bispectra (and therefore on correction terms dependent on the bispectra) had not previously been considered. I showed that while the Limber approximation must be relaxed if one is concerned with directly observing the bispectra with Stage IV experiments, the approximation is safe to make when calculating the reduced shear and magnification bias corrections.

Next, I considered another systematic effect neglected for the current generation of weak lensing surveys; the Doppler-shift of source redshifts due to the presence of over-dense spatial regions. I showed that this effect, which is closely related to the reduced shear approximation, also depends on the matter bispectrum. Using the Fisher matrix formalism again, I computed the impact of this correction on cosmological parameter inference for a *Euclid*-like survey; finding that it was safely negligible even for this upcoming generation of surveys.

A recurring concern from the investigations of the various higher-order corrections was that they posed a major computational challenge, with the corrections for a single cosmology taking on the order of multiple days to calculate. This would make Bayesian inference using techniques such as MCMCs intractable, as this computation would have to be repeated for potentially thousands of cosmologies. In the final research chapter of this thesis, I demonstrated a potential solution to this challenge; k-cut cosmic shear. This technique of making scale cuts after re-weighting observed spectra had previously proved effective in reducing sensitivity to non-linear modelling. Here, I demonstrated that applying the k-cut technique allows one to bypass the need to make the reduced shear correction, without significantly compromising the constraining

power of a *Euclid*-like experiment.

While the k-cut technique is one potential solution to the computational challenge posed by the requirement of higher-order corrections, alternative strategies may also be required. For any potential corrections significantly larger than the reduced shear correction, or ones that act at different scales, the k-cut technique may prove less effective. In this scenario, future work may be required to better optimise the computation of these higher-order terms. Alternatively, machine learning-based emulators have recently proved an efficient way of reducing computation time during the inference stage. Recent work on emulating the matter power spectrum has demonstrated the effectiveness of this strategy (Spurio Mancini et al. 2022). This could potentially be extended to modelling either the matter or convergence bispectra, or the corrections themselves directly.

Furthermore, while this thesis focuses on corrections that have not been studied before, or corrections that have not been applied to Stage IV experiments previously, the literature contains investigations of multiple other potential neglected systematic effects. A comprehensive review was required which gathers and evaluates them under a consistent framework. This is necessary to identify how these terms interact with each other, and what their cumulative impact will be on Stage IV cosmic shear surveys.

To this end, the work carried out within this thesis has a significant impact on *Euclid*, and other upcoming cosmic shear surveys. In particular, the importance of terms identified in this work has led to a concerted effort by the *Euclid* Consortium to evaluate higher-order corrections to the shear power spectrum. Euclid Collaboration: Deshpande et al. (2023) identifies 24 theoretical effects, including those evaluated in this work, and determines which are of concern for *Euclid*; explicitly modelling them. By adapting many of the techniques demonstrated in this thesis, particularly the expression of effects corrections as

projections of the matter bispectrum, Euclid Collaboration: Deshpande et al. (2023) finds multiple important terms for upcoming surveys, in addition to those identified in this thesis. In particular, neglecting source-lens clustering, the overlap of sources with each other, and the effects of the local over-density of the Universe leads to significantly biased cosmological inference. Accounting for these corrections entails many of the same challenges as those raised in this work. Accordingly, the k-cut technique demonstrated here also has increased applicability. From this thesis and the work that has sprung from it, it is evident that the existing cosmic shear formalism is no longer sufficient in the new era of surveys. As demonstrated here, a considerable number of refinements must be made to the theory, to enable these new experiments to advance the frontiers of cosmology.

Appendix A

Deriving Shot-noise

The shot (or shape) noise is the name given to the contribution to the observed lensing angular power spectra from the intrinsic, unlensed component of a galaxy's ellipticity. In spherical-harmonic space, the signal corresponding to the intrinsic ellipticity of a galaxy, $\varepsilon_{\rm src}$, and for a tomographic redshift bin, i, is given by:

$$\widetilde{\varepsilon}_{i;\ell m} = \sqrt{\frac{2}{\pi}} \sum_{g} \varepsilon_{{\rm src};g} \left(\theta_g, \chi_g\right) \, {}_2Y^*_{\ell m}(\hat{\boldsymbol{k}}), \tag{A.1}$$

where the subscript g denotes an individual galaxy, and the sum is over all galaxies in the survey.

Specifically, this signal arises because the shear field is being Poisson sampled at the locations of the galaxies. This additionally means that the term scales with inversely with the number of galaxies in the survey or in the tomographic case, the number of galaxies per bin, $N_{{\rm gal};i}$. This quantity itself can be expressed as the product of the surface-area of the survey, $A_{\rm surv}$, and the surface galaxy density of the bin, $\bar{n}_{g;i}$. If equi-populated bins are used, as in the case of a *Euclid*-like survey, this is simply $\bar{n}_g/N_{\rm bin}$. Its two-point contribution to the observed angular power spectrum is then given by:

$$N^{\epsilon}_{ij;lm} = \frac{1}{A_{\rm surv}\, \bar{n}_g/N_{\rm bin}} \left\langle \widetilde{\varepsilon}_{i;\ell m} \widetilde{\varepsilon}^*_{j;\ell' m'} \right\rangle \delta^K_{\ell\ell'} \, \delta^K_{mm'} \, \delta^K_{ij}, \tag{A.2}$$

where the final Kronecker delta accounts for the fact that ellipticies at different redshifts are intrinsically uncorrelated. This can then be expanded as:

$$N^{\epsilon}_{ij;lm} = \frac{1}{A_{\rm surv}\,\bar{n}_g/N_{\rm bin}} \int \mathrm{d}^3\boldsymbol{r}\mathrm{d}^3\boldsymbol{r}'\left\langle \varepsilon_{{\rm src};i}\varepsilon'_{{\rm src};j}\right\rangle \delta^3\left(\boldsymbol{r}-\boldsymbol{r}'\right) \\ \times \delta_{\ell\ell'}\delta^K_{mm'}\,\delta^K_{ij}\,{}_2Y_{\ell m}(\hat{\boldsymbol{r}})\,{}_2Y^*_{\ell m}(\hat{\boldsymbol{r}}'). \tag{A.3}$$

Now, one can recognise that $\left\langle \varepsilon_{{\rm src};i}\varepsilon'_{{\rm src};i}\right\rangle$ is simply the variance of observed ellipticities in the bin, which is taken to be the variance of observed ellipticities in the sample, σ^2_ϵ, which can then be taken out of the integral. Then, using the identity:

$$\int \mathrm{d}^2\boldsymbol{r}'\,{}_2Y_{\ell m}(\hat{\boldsymbol{r}})\,{}_2Y^*_{\ell m}(\hat{\boldsymbol{r}}') = \delta^K_{mm'}\,\delta^K_{\ell\ell'}, \tag{A.4}$$

one can recognise that the integration results in the area of the survey, so that I am finally left with Equation (1.89), which is reproduced here:

$$N^{\epsilon}_{l;ij} = \frac{\sigma^2_\epsilon}{\bar{n}_{\rm g}/N_{\rm bin}}\delta^{\rm K}_{ij}. \tag{A.5}$$

Appendix B

Generalised Lensing Bispectra

This chapter adapts Appendix A of Deshpande et al. (2020a).

Here, I extend the methodology used to describe the matter bispectrum, $B_{\delta\delta\delta}$, in order to describe the bispectrum of three related quantities, $B_{\mu\nu\eta}$. The three fields μ, ν, and η are proportional to the matter density contrast, δ, by some redshift-dependent weightings. This means they behave as δ would, under a small change in the fiducial cosmology. In this way, the second-order perturbation theory approach of Fry (1984) remains valid. I also assume Gaussian random initial conditions. Accordingly, the bispectrum is defined by first and second-order terms:

$$\begin{aligned} B_{\mu\nu\eta}(\boldsymbol{k}_1, \boldsymbol{k}_2, \boldsymbol{k}_3) = \langle & [\widetilde{\mu}^{(1)}(\boldsymbol{k}_1) + \widetilde{\mu}^{(2)}(\boldsymbol{k}_1)] \\ & \times [\widetilde{\nu}^{(1)}(\boldsymbol{k}_2) + \widetilde{\nu}^{(2)}(\boldsymbol{k}_2)] \\ & \times [\widetilde{\eta}^{(1)}(\boldsymbol{k}_3) + \widetilde{\eta}^{(2)}(\boldsymbol{k}_3)] \rangle, \end{aligned} \tag{B.1}$$

where the superscripts (2) and (1) denote the second and first-order terms respectively. But because I have taken Gaussian random initial conditions, the value of the three-point correlation vanishes at the lowest-order. Additionally, I neglect products of second-order terms, as these are fourth-order terms.

Equation (B.1) now becomes:

$$\begin{aligned} B_{\mu\nu\eta}(\boldsymbol{k}_1, \boldsymbol{k}_2, \boldsymbol{k}_3) = &\langle \widetilde{\mu}^{(2)}(\boldsymbol{k}_1)\widetilde{\nu}^{(1)}(\boldsymbol{k}_2)\widetilde{\eta}^{(1)}(\boldsymbol{k}_3)\rangle \\ &+ \langle \widetilde{\nu}^{(2)}(\boldsymbol{k}_2)\widetilde{\mu}^{(1)}(\boldsymbol{k}_1)\widetilde{\eta}^{(1)}(\boldsymbol{k}_3)\rangle \\ &+ \langle \widetilde{\eta}^{(2)}(\boldsymbol{k}_3)\widetilde{\mu}^{(1)}(\boldsymbol{k}_1)\widetilde{\nu}^{(1)}(\boldsymbol{k}_2)\rangle \,. \end{aligned} \tag{B.2}$$

The above assumption relating the three fields to δ, also leads one to concluding that $\delta^{(1)}$ is related to $\delta^{(2)}$ in the same way that $\mu^{(1)}$, $\nu^{(1)}$, and $\eta^{(1)}$ are related to $\mu^{(2)}$, $\nu^{(2)}$, and $\eta^{(2)}$ respectively. In which case, one can directly adapt Equation (40) of Fry (1984), to read:

$$\begin{aligned} B_{\mu\nu\eta}(\boldsymbol{k}_1, \boldsymbol{k}_2, \boldsymbol{k}_3) = &\, 2F_2(\boldsymbol{k}_2, \boldsymbol{k}_3)P_{\mu\nu}(\boldsymbol{k}_2)P_{\mu\eta}(\boldsymbol{k}_3) \\ &+ 2F_2(\boldsymbol{k}_1, \boldsymbol{k}_3)P_{\nu\mu}(\boldsymbol{k}_1)P_{\nu\eta}(\boldsymbol{k}_3) \\ &+ 2F_2(\boldsymbol{k}_1, \boldsymbol{k}_2)P_{\eta\mu}(\boldsymbol{k}_1)P_{\eta\nu}(\boldsymbol{k}_2), \end{aligned} \tag{B.3}$$

where $P_{\mu\nu}$ are the two-point power spectra for fields μ and ν, analogous to the matter power spectrum, and:

$$F_2(\boldsymbol{k}_1, \boldsymbol{k}_2) = \frac{5}{7} + \frac{1}{2}\frac{\boldsymbol{k_1}\cdot\boldsymbol{k_2}}{k_1 k_2}\left(\frac{k_1}{k_2} + \frac{k_2}{k_1}\right) + \frac{2}{7}\left(\frac{\boldsymbol{k_1}\cdot\boldsymbol{k_2}}{k_1 k_2}\right)^2. \tag{B.4}$$

As in Scoccimarro & Couchman (2001), this can then be modified to include numerical fitting to N-body simulations by exchanging F_2 for $F_2^{\rm eff}$, as defined in Equation (2.6). The fitting formula determined in Scoccimarro & Couchman (2001) still remains valid, because it does not have any redshift dependence and does not depend on the fiducial cosmology. The density perturbation-IA bispectrum, used in the IA-enhanced lensing bias correction, is then a specific case of this formula, where $\mu = \nu = \delta$, and $\eta = I$.

Bibliography

Akeson, R., Armus, L., Bachelet, E., et al. 2019, arXiv e-prints, arXiv:1902.05569

Albrecht, A., Bernstein, G., Cahn, R., et al. 2006, arXiv e-prints, astro ph/0609591

Assassi, V., Simonović, M., & Zaldarriaga, M. 2017, J. Cosmology Astropart. Phys., 2017, 054

Astropy Collaboration, Price-Whelan, A. M., Sipőcz, B. M., et al. 2018, AJ, 156, 123

Astropy Collaboration, Robitaille, T. P., Tollerud, E. J., et al. 2013, A&A, 558, A33

Bacon, D., Refregier, A., & Ellis, R. 2000, MNRAS, 318, 625

Bacon, D. J., Andrianomena, S., Clarkson, C., Bolejko, K., & Maartens, R. 2014, MNRAS, 443, 1900

Barreira, A., Krause, E., & Schmidt, F. 2018, J. Cosmology Astropart. Phys., 2018, 053

Barreira, A., Nelson, D., Pillepich, A., et al. 2019, MNRAS, 488, 2079

Bartelmann, M. & Schneider, P. 2001, Phys. Rep., 340, 291

Battye, R. A. & Moss, A. 2014, Phys. Rev. Lett., 112, 051303

Bernardeau, F., Bonvin, C., & Vernizzi, F. 2010, Phys. Rev. D, 81, 083002

Bernardeau, F., Nishimichi, T., & Taruya, A. 2014, MNRAS, 445, 1526

Blake, C. & Bridle, S. 2005, MNRAS, 363, 1329

Blas, D., Lesgourgues, J., & Tram, T. 2011, J. Cosmology Astropart. Phys., 2011, 034

Bridle, S. & King, L. 2007, New J. Phys., 9, 444

Copeland, D., Taylor, A., & Hall, A. 2018, MNRAS, 480, 2247

Cropper, M., Cole, R., James, A., et al. 2012, in Proc. SPIE, Vol. 8442, Space Telescopes and Instrumentation 2012: Optical, Infrared, and Millimeter Wave, ed. M. C. Clampin, G. G. Fazio, H. A. MacEwen, & J. Oschmann, Jacobus M., 84420V

Cuesta-Lazaro, C., Quera-Bofarull, A., Reischke, R., & Schäfer, B. M. 2018, MNRAS, 477, 741

Dark Energy Survey Collaboration. 2005, arXiv e-prints, astro ph/0510346

de Jong, J., Kuijken, K., Applegate, D., et al. 2013, The Messenger, 154, 44

Deshpande, A. C. & Kitching, T. D. 2020, Phys. Rev. D, 101, 103531

Deshpande, A. C. & Kitching, T. D. 2021, Phys. Rev. D, 103, 123510

Deshpande, A. C., Kitching, T. D., Cardone, V. F., et al. 2020a, A&A, 636, A95

Deshpande, A. C., Taylor, P. L., & Kitching, T. D. 2020b, Phys. Rev. D, 102, 083535

Dodelson, S., Shapiro, C., & White, M. 2006, Phys. Rev. D, 73, 023009

Duncan, C. A. J., Joachimi, B., Heavens, A. F., Heymans, C., & Hildebrandt, H. 2014, MNRAS, 437, 2471

Dyson, F., Eddington, A., & Davidson, C. 1920, Phil. Trans. Royal Soc. London Series A, 220, 291

Einstein, A. 1916, Annalen der Physik, 354, 769

Euclid Collaboration: Blanchard, A., Camera, S., Carbone, C., et al. 2020, A&A, 642, A191

Euclid Collaboration: Deshpande, A. C., Kitching, T., Hall, A., et al. 2023, arXiv e-prints, arXiv:2302.04507

Freedman, W. L., Madore, B. F., Hatt, D., et al. 2019, ApJ, 882, 34

Fry, J. 1984, ApJ, 279, 499

Gil-Marín, H., Wagner, C., Fragkoudi, F., Jimenez, R., & Verde, L. 2012, J. Cosmology Astropart. Phys., 2012, 047

Gurri, P., Taylor, E. N., & Fluke, C. J. 2020, MNRAS

Heymans, C., Van Waerbeke, L., Miller, L., et al. 2012, MNRAS, 427, 146

Hikage, C., Oguri, M., Hamana, T., et al. 2019, Pub. Astro. Soc. Japan, 71, 43

Hildebrandt, H., Köhlinger, F., van den Busch, J. L., et al. 2020, A&A, 633, A69

Hu, W. & Kravtsov, A. V. 2003, ApJ, 584, 702

Hubble, E. 1929, PNAS, 15, 168

Huff, E. M., Krause, E., Eifler, T., et al. 2013, arXiv e-prints, arXiv:1311.1489

Hui, L., Gaztañaga, E., & Loverde, M. 2007, Phys. Rev. D, 76, 103502

Huterer, D. & White, M. 2005, Phys. Rev. D, 72, 043002

Joachimi, B. & Bridle, S. L. 2010, A&A, 523, A1

Joachimi, B., Cacciato, M., Kitching, T., et al. 2015, Space Sci. Rev., 193, 1

Kaiser, N., Wilson, G., & Luppino, G. A. 2000, arXiv e-prints, astro ph/0003338

Kiessling, A., Cacciato, M., Joachimi, B., et al. 2015, Space Sci. Rev., 193, 67

Kilbinger, M. 2015, Rep. Prog. Phys., 78, 086901

Kirk, D., Brown, M., Hoekstra, H., et al. 2015, Space Sci. Rev., 193, 139

Kitching, T. D., Alsing, J., Heavens, A. F., et al. 2017, MNRAS, 469, 2737

Kitching, T. D. & Heavens, A. F. 2017, Phys. Rev. D, 95, 063522

Krause, E. & Hirata, C. 2010, A&A, 523, A28

Lacasa, F. & Grain, J. 2019, A&A, 624, A61

Laureijs, R., Amiaux, J., Arduini, S., et al. 2011, arXiv e-prints, arXiv:1110.3193

Lee, H. & Dvorkin, C. 2020, J. Cosmology Astropart. Phys., 2020, 044

Lemaître, G. 1927, Annales de la Société Scientifique de Bruxelles, 47, 49

Lesgourgues, J. & Pastor, S. 2006, Phys. Rep., 429, 307

Lewis, A., Challinor, A., & Lasenby, A. 2000, ApJ, 538, 473

Limber, D. N. 1953, ApJ, 117, 134

Lin, C.-H., Harnois-Déraps, J., Eifler, T., et al. 2020, MNRAS, 499, 2977

Linder, E. V. 2005, Phys. Rev. D, 72, 043529

Liu, J., Haiman, Z., Hui, L., Kratochvil, J. M., & May, M. 2014, Phys. Rev. D, 89, 023515

Lorenz, C. S., Alonso, D., & Ferreira, P. G. 2018, Phys. Rev. D, 97, 023537

LoVerde, M. & Afshordi, N. 2008, Phys. Rev. D, 78, 123506

LSST Science Collaboration, Abell, P. A., Allison, J., et al. 2009, arXiv e-prints, arXiv:0912.0201

Massey, R., Hoekstra, H., Kitching, T., et al. 2013, MNRAS, 429, 661

Mead, A. J., Peacock, J. A., Heymans, C., Joudaki, S., & Heavens, A. F. 2015, MNRAS, 454, 1958

Meneghetti, M. 2016, Introduction to Gravitational Lensing - Lecture scripts (Springer Cham), 6–9

Mörtsell, E. & Dhawan, S. 2018, J. Cosmology Astropart. Phys., 2018, 025

Munshi, D., Namikawa, T., Kitching, T. D., et al. 2020, MNRAS, 493, 3985

Newton, I. 1704, Opticks: or, A treatise of the reflections, refractions, inflections and colours of light, 1st edn. (Samuel Smith and Benjamin Walford, London)

Perlmutter, S., Aldering, G., Goldhaber, G., et al. 1999, ApJ, 517, 565

Planck Collaboration, Aghanim, N., Akrami, Y., et al. 2020, A&A, 641, A6

Riess, A. G., Casertano, S., Yuan, W., Macri, L. M., & Scolnic, D. 2019, ApJ, 876, 85

Riess, A. G., Filippenko, A. V., Challis, P., et al. 1998, ApJ, 116, 1009

Schmidt, F., Rozo, E., Dodelson, S., Hui, L., & Sheldon, E. 2009, ApJ, 702, 593

Scoccimarro, R. & Couchman, H. 2001, MNRAS, 325, 1312

Sellentin, E., Heymans, C., & Harnois-Déraps, J. 2018, MNRAS, 477, 4879

Sellentin, E. & Starck, J.-L. 2019, J. Cosmology Astropart. Phys., 2019, 021

Semboloni, E., Hoekstra, H., & Schaye, J. 2013, MNRAS, 434, 148

Shao, J., Zhang, P., Lin, W., Jing, Y., & Pan, J. 2011, MNRAS, 413, 628

Shapiro, C. 2009, ApJ, 696, 775

Springel, V., White, S. D. M., Jenkins, A., et al. 2005, Nature, 435, 629

Spurio Mancini, A., Piras, D., Alsing, J., Joachimi, B., & Hobson, M. P. 2022, MNRAS, 511, 1771

Sugiyama, N. S., Okumura, T., & Spergel, D. N. 2017, J. Cosmology Astropart. Phys., 01, 057

Takada, M. & Hu, W. 2013, Phys. Rev. D, 87, 123504

Takahashi, R., Nishimichi, T., Namikawa, T., et al. 2020, ApJ, 895, 113

Takahashi, R., Sato, M., Nishimichi, T., Taruya, A., & Oguri, M. 2012, ApJ, 761, 152

Taylor, A., Kitching, T., Bacon, D., & Heavens, A. 2007, MNRAS, 374, 1377

Taylor, P. L., Bernardeau, F., & Huff, E. 2021, Phys. Rev. D, 103, 043531

Taylor, P. L., Bernardeau, F., & Kitching, T. D. 2018a, Phys. Rev. D, 98, 083514

Taylor, P. L., Kitching, T. D., Alsing, J., et al. 2019, Phys. Rev. D, 100, 023519

Taylor, P. L., Kitching, T. D., & McEwen, J. D. 2018b, Phys. Rev. D, 98, 043532

Tegmark, M., Taylor, A., & Heavens, A. 1997, ApJ, 480, 22

Thiele, L., Duncan, C. A. J., & Alonso, D. 2020, MNRAS, 491, 1746

Turner, E. L., Ostriker, J. P., & Gott, III, J. R. 1984, ApJ, 284, 1

Tyson, J., Valdes, F., & Wenk, R. 1990, ApJ, 349, L1

Van Waerbeke, L., Mellier, Y., Erben, T., et al. 2000, A&A, 358, 30

Verde, L. 2007, arXiv e-prints, arXiv:0712.3028

Verde, L. 2010, in Lecture Notes in Physics, Berlin Springer Verlag, ed. G. Wolschin, Vol. 800 (Berlin Springer Verlag), 147–177

von Soldner, J. 1804, Astronomisches Jahrbuch für das Jahr 1804, 1804, 161

Walsh, D., Carswell, R., & Weymann, R. 1979, Nature, 279, 381

Weinberg, D. H. 2007, A873: Cosmology Course Notes VII. Linear Fluctuations, Ohio State University Astronomy Department

Weinberg, S. 2008, Cosmology (Oxford University Press)

Wittman, D., Tyson, J., Kirkman, D., Dell'Antonio, I., & Bernstein, G. 2000, Nature, 405, 143